Design Methodology for an Ultra-High Efficiency Coreless Resonant Power Transformer

by

Noah J. Salk
B.S., University of Illinois at Urbana-Champaign (2020)

Submitted to the Department of Electrical Engineering and Computer Science in partial fulfillment of the requirements for the degree of

Master of Science
at the
MASSACHUSETTS INSTITUTE OF TECHNOLOGY
May 2022

Author .....
Noah J. Salk
Department of Electrical Engineering and Computer Science
May 13, 2022

Certified by .....
Chathan M. Cooke
Principal Research Engineer, Research Laboratory of Electronics
Thesis Supervisor

Accepted by .....
Leslie A. Kolodziejski
Professor of Electrical Engineering and Computer Science
Chair, Department Committee on Graduate Students

Design Methodology for an Ultra-High Efficiency Coreless Resonant Power Transformer

by

Noah J. Salk

Submitted to the Department of Electrical Engineering and Computer Science
on May 13, 2022, in partial fulfillment of the
requirements for the degree of
Master of Science

Abstract

Coreless resonant power transformers, operating at high frequency, have several advantages over the traditional iron core transformer. They have a simple structure, are lighter, cheaper, and more efficient due to the elimination of core losses. For a given cooling capacity, pushing the efficiency of these devices by as little as a fraction of a percent can lead to a substantial increase in power throughput capability. In order to achieve ultra-high efficiency designs, several advanced conductor topologies are explored with the development of corresponding experimentally validated modeling techniques to capture extra losses due to non-ideal conductor construction and elliptically rotational magnetic fields. In consideration of industrial economics, care is taken throughout this work to minimize conductor complexity. The variety of modeling techniques developed in this work allow for fast design space exploration as well as accurate loss predictions for down-selected conductors. An optimization is performed to choose a final design for an ultra-high efficiency (>99%) 40 kW transformer with a x4 voltage ratio. The transformer was constructed and thermal comparisons at partial load were made with a lower efficiency transformer of the same magnetic design built using solid conductors. Results demonstrate a >2x reduction in loss and a subsequent coil efficiency >99%.

Thesis Supervisor: Chathan M. Cooke
Title: Principal Research Engineer, Research Laboratory of Electronics

Acknowledgments

First and foremost, I would like to thank my advisor, Dr. Chathan Cooke, for his patience, unbounded support of my studies, receptiveness to research tangents, and for sharing wisdom accumulated over his incredible career. Through mentorship under a serial experimentalist such as Dr. Cooke, I've learned the importance of controlling one's environment, tailoring experimental setups to amplify desired phenomena, and addressing seemingly insignificant real-life considerations that may have a large impact on measurement results. Most importantly, I've learned to never trust first observations or rush to conclusions until exhausting all possible sources of error.

I am also incredibly grateful for Carlos Gaytan Cavazos, Juan Angel Israel Barrientos Torres, and the rest of the ProlecGE team for supporting my research both financially and technically, and for providing great system-level feedback that helped shape the direction of this research. Additionally, I am grateful for the financial assistance of the EE Landsman (1958) departmental fellowship at MIT and the EECS MathWorks Engineering Fellowship, which relieved some of the financial pressures of graduate studies and allowed me to focus solely on my research.

Last but not least, none of this work would be possible without the support of my family and the adventure-loving friends I've met over the past two years in the Cambridge/Boston area.

Contents

List of Figures

List of Tables

Chapter 1

Introduction

Work is underway at MIT's High Voltage Research Laboratory to develop an advanced power transformer topology for and supported by ProlecGE. The four-coil, air-core structure consists of two resonant coils, a drive (primary) coil, and a load (secondary) coil. A 40 kW version of this transformer (see Fig. 1-1) with a 4x voltage ratio has been built and tested [1, 2]. Magnetically efficient energy transfer is established with high-frequency resonant coupling and eliminates the need for flux-carrying magnetic materials. The absence of an iron core leads to several advantages over traditional transformers including load independent efficiency, lower cost, lower weight, and higher efficiency due to the removal of core losses. The design of the previously built 40 kW transformer, utilizing large diameter solid copper conductors, has a theoretical efficiency of 98.6% at the operating frequency. As thermal limits set by the cooling scheme determine a device's power rating, increasing this transformer's efficiency by 1% allows the power throughput to be nearly tripled while maintaining the same losses. Another way to look at the efficiency improvement is by a 3x reduction in heat load and associated simplification of the auxiliary cooling infrastructure.

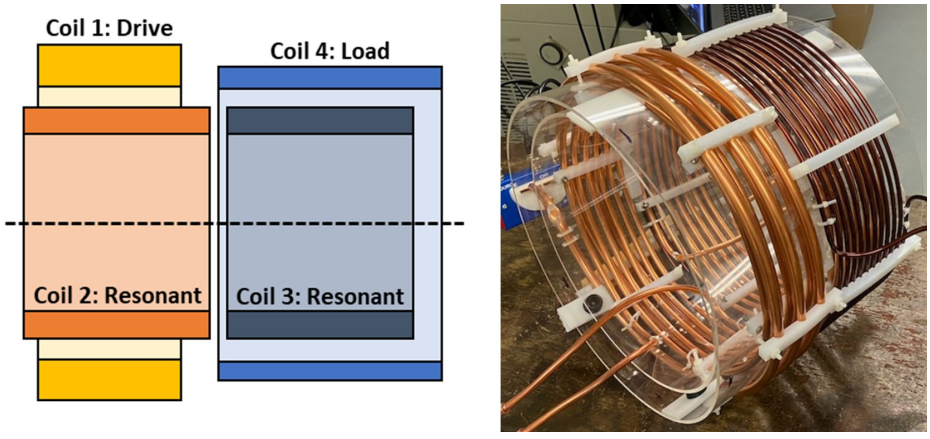

Figure 1-1: (left) The general structure of a 4 coil, coreless transformer and (right) MIT's 40 kW solid conductor transformer with a 4x voltage ratio.

1.1 Motivation

A key limitation to high frequency operation of conductors is the inherent limitation of magnetic diffusion which restricts currents to near surface regions of the conductors. This, in turn, causes an increase in resistance and increased losses, known as AC losses. As will be explained in greater depth throughout this thesis, increasing the transformer efficiency requires special care to reduce AC losses in the conductors, which become substantial at small skin depths relative to the dimensions of the conductor. In order to choose appropriate conductors and conductor arrangements, high-fidelity models and techniques must be implemented to accurately assess the performance of each configuration. Litz wire, a common solution to the AC loss problem, is structured to achieve near DC resistance by twisting together several levels of sub-bundles consisting of smaller individually insulated strands. This arrangement, in theory, achieves full transposition such that each strand has the same net resistance between terminals and therefore current is uniformly distributed throughout the cross-section of the conductor. As detailed below, analytical models for simple arrangements of Litz wire have been developed in the literature over the past century [3–10] and higher accuracy, more general numerical simulation approaches have been the focus of recent work. The large number of strands and complex 3D twisted geometry poses a challenge for numerical simulation approaches due to the large number of mesh elements required for solution convergence. Both 3D finite element analysis (FEA) [11–14] and a more novel partial element equivalent circuit (PEEC) approach [15–19] have been adopted for analysis, but both are generally too time and resource demanding to enable full design space optimizations.

1.2 Approach

A new 2D Litz wire modeling method is developed in this work, which employs a unique geometry to simulate the real, non-ideal structure of commercially available Litz wire. A DC simulation is used to relieve the mesh element burden of the computation. While the simulation setup is more complex due to non-general geometries, the goal is to match theory with measurements with high accuracy and down-select a set of conductors for a given application.

An additional consideration is that the analytical methods in the literature do not apply to the multi-phase, multi-coil geometry of the four-coil resonant transformer due to the introduction of elliptically rotational magnetic fields. Modifications are made to analytical models to account for loss associated with elliptically rotational magnetic fields for the first time and the resulting method is fast enough to enable optimization of the transformer's conductors. Finally, this optimization is used to maximize the transformer efficiency and minimize the total number of strands used in the transformer's coils. The number of strands in a conductor is indicative of manufacturing complexity and generally correlates to the cost of the conductor: a major factor in consideration of industrial economics [20, 21]. With conductor complexity reduction in mind, several non-Litz constructions are explored in this work to

quantify potential performance improvements in simple geometries.

The loss analysis techniques developed in this work are generally applicable to high frequency power applications such as induction heaters [22, 23], wireless power transfer systems [24–27], and high-speed electric machines [28–33].

Quantifying the performance of a conductor in a given application can be accomplished through several forms of analysis. These approaches are generally categorized as numerical or analytical in nature. The following two subsections give an overview of tools developed in the literature and modifications to these tools that have demonstrated good results in practice.

1.3 Numerical Methods

The three most common numerical approaches to simulate AC current distributions in conductors (and therefore compute AC losses) are 2D FEA, 3D FEA, and the more novel PEEC method [34, 35].

1.3.1 2D FEA

Two-dimensional FEA is a good approach for modeling solid conductors in AC environments. Most softwares allow for variable meshing in selected domains of the simulation. This becomes especially useful at high-frequencies when the current is mostly located within a relatively small distance from the conductor's outer surface, known as the *skin depth*. Most softwares also include an axisymmetric modeling option, which is particularly useful in modeling cylindrical coils. Using the axisymmetric option, however, ignores the finite pitch of cylindrically wound coils and therefore each turn is approximated as a hoop. In the FEA formulation, Maxwell's equations, in their differential form, are solved for everywhere in the simulation domain.

The open source FEA program FEMM [36] is commonly used in industry to solve 2D magnetoquasistatic problems. Companies such as Tesla have used the software to analyze their motor designs. Simulating twisted bundles in 2D makes the assumptions that 1) all current is traveling normal to the domain, ignoring any magnetic field component not in the plane of the simulation, and that 2) all cross-sections are circular. These two assumptions are approximations which closely resemble the circumstances when the bundle twist pitch is sufficiently long compared to the bundle outer diameter. Simulating axisymmetric problems is relatively straight forward in 2D; this includes stranded conductors if each strand is placed in series to force equal current sharing and approximate perfect transposition.

First Level

The simplest twisted bundle structure, the single-level bundle, has strands placed in a rotationally symmetric manner about the bundle's axis (see Fig. 1-2). For isolated conductor skin effect analysis in planar 2D simulations there is no difference between modeling this type of bundle as a twisted bundle or parallel wire bundle. The current

density distributions are rotationally symmetric, and every strand sees every position in the bundle. If the strands are all put in parallel, as they would be if soldered together at the end terminals, each strand sees the same current.

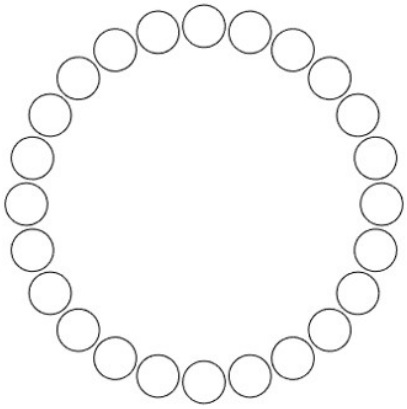

Figure 1-2: 24 strand single-level bundle cross-section with $F_{ins} = 0.05$.

With the total peak current through the bundle, I_{tot}, and by setting a place-holder depth of domain, L, the finite element problem is solved and the average resistive losses over the entire domain is calculated by FEMM using the local electric field, E, and the period, $T = \frac{1}{f}$,

$$P_{tot} = \frac{1}{T} \int_0^T \Re\mathrm{e}\Big\{ \iiint_V \mathbf{J} \cdot \mathbf{E} \Big\} dt \tag{1.1}$$

the AC resistance of the equivalent parallel-strand bundle per-unit-length is,

$$R_{AC} = \frac{2P_{tot}}{I_{tot}^2 L} \tag{1.2}$$

where the factor of two comes from the time-averaged power loss. The DC resistance per-unit-length of a bundle with N_s strands each with diameter d_s is,

$$R_{DC} = \frac{4\rho}{N_s \pi d_s^2} \tag{1.3}$$

While the multi-level simulation method is more complicated and will be discussed in the next section, it should be noted that the highest bundle level in a Litz wire is also rotationally symmetric about the center of the bundle, providing us with one simplification during analysis. After calculating the per-unit-length resistances the added resistance from increased conductor length introduced with twisting can be simply multiplied by a factor using helical path lengths. Twisting typically adds less than 2.5% to the strand length [37, 38].

Successive Level (Rotating Series)

If we were to simulate a two-level bundle like the one shown in Fig. 1-3(a) using the same method as described above. All the current would redistribute to the strands closest to the outside of the bundle as shown in Fig. 1-3(b). This would reflect reality if the bundle were not twisted, as all strands are placed in parallel and the current can simply flow out of the end terminals and into the outer strands. However, since this is a Litz wire and all bundles are assumed to be perfectly twisted such that every strand carries the same current, we know the effect of transposition is not being captured in the 2D simulation. To get around this, we can use our knowledge that every strand carries the same current and meet that boundary condition by placing all strands in a series circuit which carries $\frac{I_{tot}}{N_s}$ total current. This results in a much different current density distribution as shown in Fig. 1-3(c).

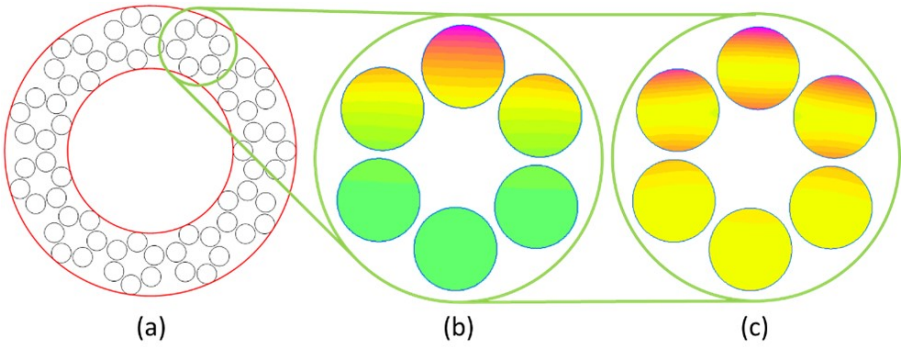

Figure 1-3: (a) A representative two-level, 11 x 6 bundle cross-section (b) sub-bundle current density distribution when all strands are placed in parallel (c) current density distribution when all strands are placed in series.

The cross-sectional current densities will clearly change throughout the twist pitch of the bundle and a more dramatic change is seen in sub-bundles with fewer strands. To simulate this, the FEA problem for a given bundle must be solved multiple times, where each time the sub-bundle(s) are rotated to intermediate positions seen along the length of the wire. Because of the axisymmetric condition of the highest-level as stated previously, we need only calculate the total power loss of all the strands in one of the highest-level sub-bundles and multiply by the number of bundles in that level to get the total power loss per-unit-length at that position, saving computation time. This total power loss per-unit-length is averaged over all intermediate positions and the AC resistance per-unit-length is then calculated by,

$$R_{AC,bundle} = \frac{2N_{tot}\langle P_{tot}\rangle}{LI_{tot}^2} \tag{1.4}$$

where N_{tot} is the total number of strands in the bundle.

1.3.2 3D FEA

3D FEA has the capability of modeling reality within computational limits. With three-dimensional models of the geometry, parametric trajectories of the strands in the twisted bundle can be fully modeled. The drawback with this approach is a substantial increase in computational resource requirements to achieve similar accuracy to a two-dimensional model. Meshing also becomes more cumbersome when general tetrahedral elements are used. Nevertheless, several researchers have succssfully implemented 3D FEA for their applications [12, 13].

The software COMSOL [39] is a very powerful multiphysics FEA program with the AC/DC module [40] capable of modeling 3D electromagnetic problems. A 3D model of the Litz wire can be created using very simple parametric equations as will be discussed later. These simulations should capture all effects of Litz wire with almost no assumptions. Non-normal currents are simulated, creating non-planar magnetic field components. In addition, all currents will redistribute for equal current sharing automatically by nature of transposition without forcing any boundary conditions.

By using the differential form of Maxwell's equations, the entire domain must be meshed fine enough to give accurate results. This includes meshing the surrounding air in addition to the conductors. For this reason, meshing is the most tedious part of modeling in 3D FEA. There is a trade-off between simulation time and mesh density as well as between mesh density and simulation accuracy. Further complicating matters, a high mesh density demands large amounts of random access memory (RAM) on the simulating computer. The 3x3 bundle shown in Fig. 1-4(a) was meshed using the automatic physics-controlled meshing algorithm in COMSOL with a setting of "extremely fine," demanding 150 GB of RAM. The resulting current density distribution at multiple points along the length of the wire is shown in Fig. 1-4(b).

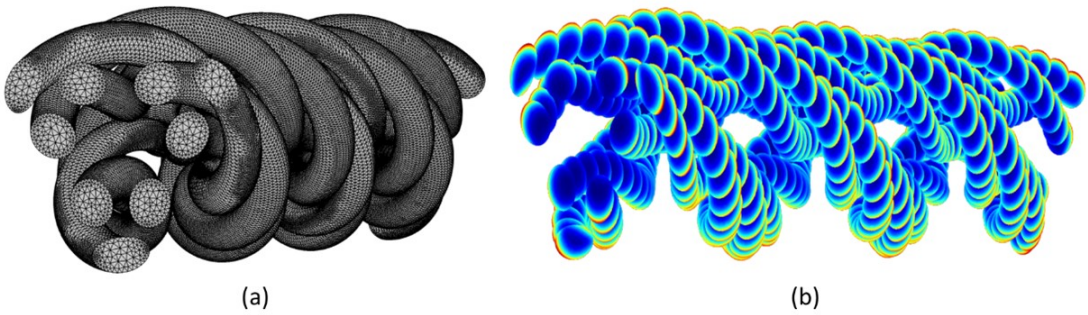

Figure 1-4: (a) "Extremely fine" physics-controlled mesh of a 3x3 bundle (b) the resulting current density cross sections along the length of the wire

1.3.3 PEEC

The partial element equivalent circuit (PEEC) numerical method was introduced several decades ago but has garnered renewed interest in recent years specifically for the analysis of complex 3D structures such as Litz wires. Like 3D FEA, this method

in an air-core application makes no assumptions and will simulate reality provided proper discretization. PEEC theory uses the integral formulation of Maxwell's equations, which simplifies the problem by only requiring discretization of the conductors and not the surrounding air. For frequencies below 1 MHz, the idea is to break the conductor into small filaments and calculate the partial inductances between these filaments (including self-inductance) as well as the partial resistance of each filament. This forms an impedance matrix, Z, and the filament terminal connections are described in the meshing matrix, M. Each filament is assumed to carry uniform current density. The problem can then be treated as an electrical circuit, where the generalize minimal residual method (GMRES) is used to solve the equation for branch currents, I_m, given terminal voltages, V_s,

$$MZM^T I_m = V_s \tag{1.5}$$

The AC resistance is then extracted using the total power loss from all filament calculated with the partial resistances and branch currents. An open-source program, FastLitz, was developed by Zhang et al. at MIT [15,16] that applies the PEEC method specifically to Litz wire. It's predecesor, FastHenry [41], was also developed at MIT for general inductive applications such as PCB layouts. FastLitz and the general PEEC method have been further developed in [17–19, 42–44] to improve accuracy, speed of impedance extractions, and to expand the application space. Partial capacitances must be considered for frequencies greater than 1 MHz.

A comparison between 3D models for the same 3 x 3 Litz wire in FastLitz and COMSOL is shown in Fig. 1-5.

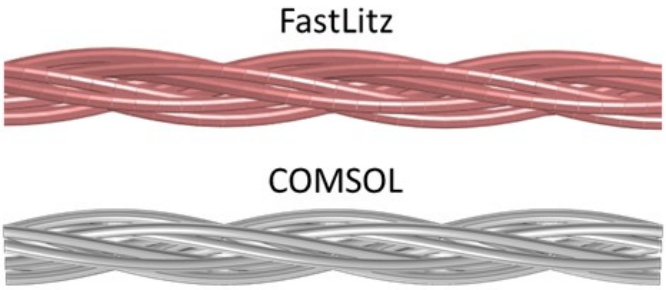

Figure 1-5: The same 3 x 3 Litz wire modeled in FastLitz and COMSOL.

Each strand must be discretized radially and lengthwise. Since most of the calculation effort in the PEEC method is from impedance extraction for non-parallel filaments, more meshed elements results in longer simulation times. The PEEC method implemented in FastLitz uses rectangular filaments as shown in Fig. 1-5 to make impedance extraction faster as there exists exact calculations for the mutual inductance between rectangular conductors in space [45].

A discretization study was performed to find the required level of radial and lengthwise discretization by comparing simulation results for a 5-strand parallel bundle in FastLitz to results from FEMM. Radial discretization is measured as the number of

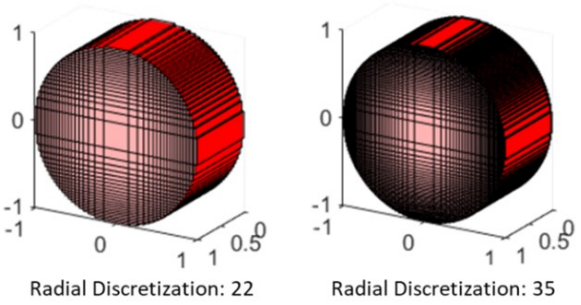

Figure 1-6: Strand cross-sections with varying radial discretization in FastLitz. Fine meshing must be used for accurate results.

filaments along one axis from the center to the radius of the strand. Lengthwise discretization is the number of elements throughout the length of the strand. Results of the study showed that to converge close enough to the FEMM solution for designs up to $\frac{d_s}{2\delta} = 6$ with strand diameter, d_s, significant radial and lengthwise discretization must be used: 30 m^{-1} and 76 m^{-1} respectively. With this meshing scheme, each operating point in FastLitz took roughly 5 minutes to compute while the simulation time in FEMM was comparatively negligible. Results from the fine meshing scheme are shown side-by-side with FEMM results in Fig. 1-7.

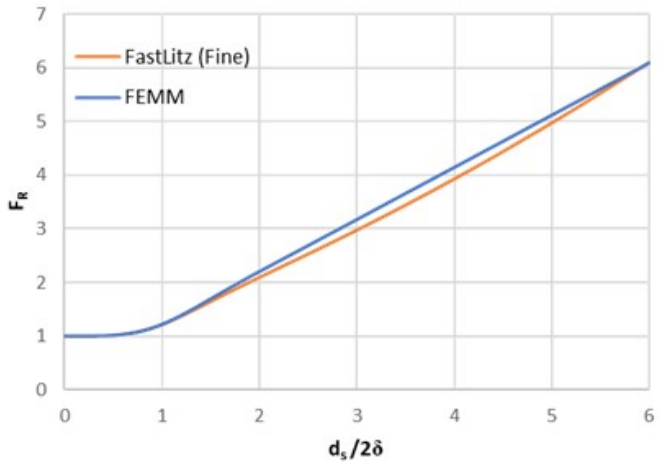

Figure 1-7: Comparison between FastLitz with a fine meshing scheme and FEMM for the 5-strand parallel bundle.

1.3.4 Comparison of Methods to Experimental Measurements

In problems for which there exists no-exact solution, numerical methods must be validated against experimental data. To demonstrate that 2D axisymmetric FEA simulations can accurately compute both the skin effect and proximity effect, we compared our simulation results for an air-core solenoid to measured data in the

literature carried out by Ibuchi *et al* [46]. The air-core solenoid was chosen because it experiences both eddy current effects. The axisymmetric solenoid geometry is laid out in Fig. 1-8. With the parameter values shown in Fig. 1-9 for two different solenoids, FEMM simulations were run and the results are overlaid onto plots taken from [46] as shown in Fig. 1-10. The AC resistances from the FEMM simulations very closely followed experimental data for both solenoids. This gives confidence that FEMM can successfully model complex eddy current phenomenon from both skin and proximity effect.

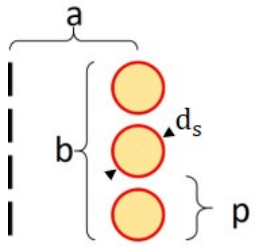

Figure 1-8: Air-core solenoid geometric parameter space.

Type	No.	a [mm]	b [mm]	N	Calculated inductance [µH]	Measured Ls [µH] (at 1 kHz)
Single-layer (sparse)	SL-03	10.6	244.8	76	10.51	10.53
	SL-04	46.1	30.4	9	9.84	9.88

Figure 1-9: List of defining parameters for the two air-core solenoids compared in Ibuchi *et al*, with $d_s = 1.6$ mm and $p = 3.2$ mm.

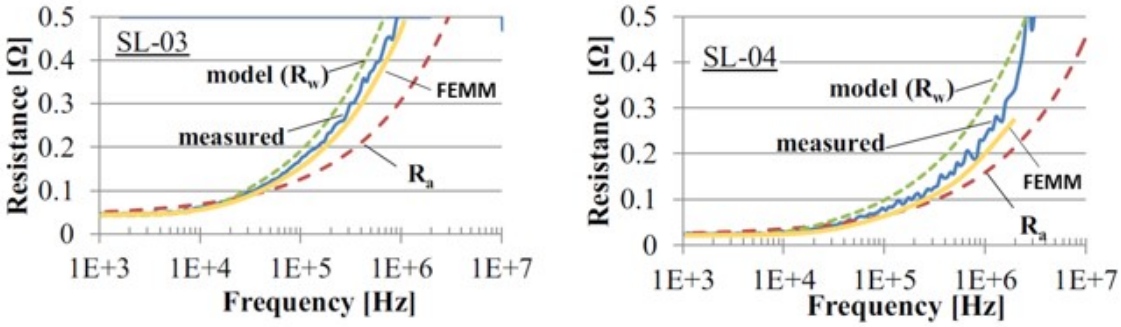

Figure 1-10: Air-core solenoid FEMM simulation results overlaid onto measured data from Ibuchi *et al*, with $d_s = 1.6$ mm and $p = 3.2$ mm.

In the same paper that describes FastLitz [15], experimental validation of the method was performed using measured data from a 3 x 3 Litz wire. The geometry of the Litz wire was fully defined in the paper such that the wire could be reproduced

in the proposed 2D FEA simulation analysis. The Litz wire is twisted in different directions at each bundle level and the strand used was a 32 AWG magnet wire with 30 μm thick insulation. The wire has a total length of 19 cm and twist pitch on each level of 1 cm. Fig. 1-11 shows the FastLitz experimental validation taken from [15] overlaid with results from the 2D FEMM rotating series method. Results from the 2D simulation line up well with measured data, outperforming analytical models. For frequencies below 1 MHz the 2D results closely follow FastLitz, suggesting that the difference between the measured data and simulation results is non-idealities in the construction of the Litz wire. It should be noted that there is a significant advantage in simulation time when using the 2D method instead of either 3D method.

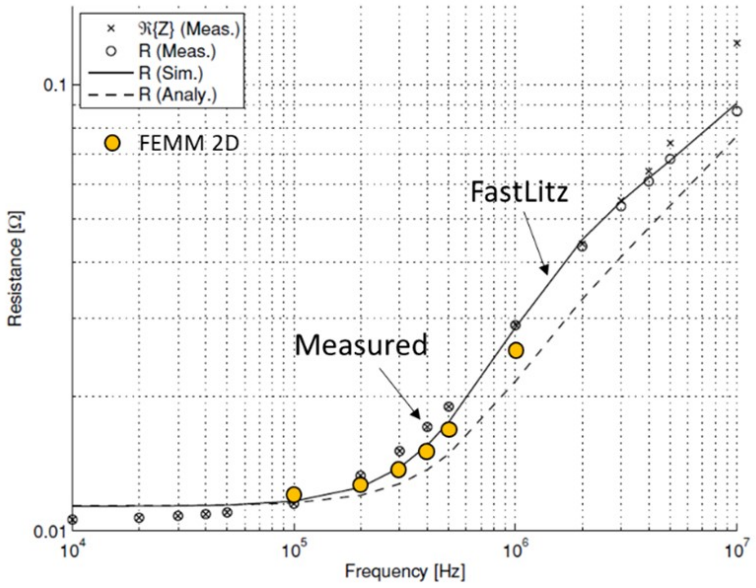

Figure 1-11: FastLitz experimental validation with our 2D FEMM rotating series method results overlaid at the measured operating frequencies, base figure taken from Zhang *et al.*

1.4 Analytical Methods

The basis of nearly all analytical models in the literature [3, 5, 6, 8–10, 47, 48] is the exact analytical solution to skin and proximity loss in a solid conductor.

1.4.1 Skin-effect

The exact solution to the AC resistance per-unit-length of an isolated cylindrical conductor with diameter d_s is well known and is written in terms of Bessel function

as follows,

$$R_{AC} = \Re\mathrm{e}\left\{ \frac{k\rho}{\pi d_s} \frac{J_0\left(\frac{kd_s}{2}\right)}{J_1\left(\frac{kd_s}{2}\right)} \right\} \tag{1.6}$$

where the complex wave number, k, is defined as $\frac{1-j}{\delta}$, ρ is the resistivity, and J_0 and J_1 are Bessel functions of the first kind, order 0 and order 1 respectively. The Bessel functions are written as infinite series,

$$J_0\left(\frac{kd_s}{2}\right) = \sum_{n=0}^{\infty} \frac{(-1)^n}{n!n!}\left(\frac{kd_s}{4}\right)^{2n} \tag{1.7}$$

$$J_1\left(\frac{kd_s}{2}\right) = \sum_{n=0}^{\infty} \frac{(-1)^n}{n!(n+1)!}\left(\frac{kd_s}{4}\right)^{2n+1} \tag{1.8}$$

A detailed derivation of the above solution is provided in [49] and experimentally validated in [50]. A useful parameter for comparing how close a conductor design is to DC conditions and full copper utilization is the AC to DC resistance ratio, F_R. This is computed by dividing the AC resistance of a conductor by the DC resistance, which in per-unit-length metrics is simply calculated using the total copper area, $A_{Cu,tot}$, in the formula

$$R_{DC} = \frac{\rho}{A_{Cu,tot}} \tag{1.9}$$

Fig. 1-12 shows F_R plotted against $\frac{d_s}{2\delta}$ which encapsulates both strand diameter, material, and frequency information.

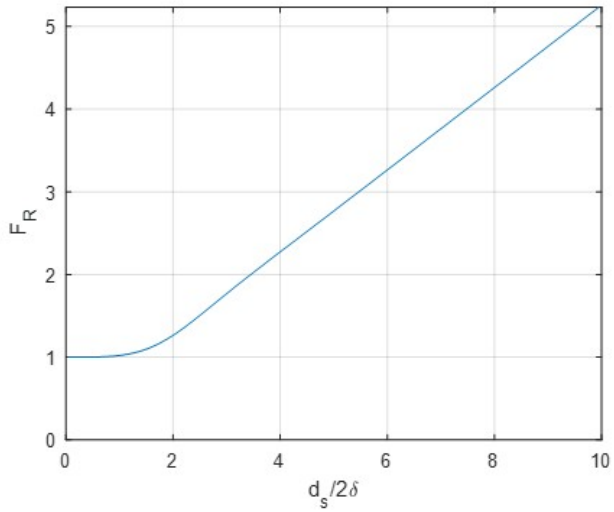

Figure 1-12: Exact solution to the resistance ratio for a solid cylindrical conductor plotted against $\frac{d_s}{2\delta}$

Although efficient computation of the Bessel functions is available in most mathematical scripting softwares and libraries [51–53], it may be advantageous to have

a simpler formulation to reduce run times in large simulations. Through parameter optimization, the following function was found to have less than 0.02% error when $\frac{d_s}{2\delta} < 2$,

$$F_R = \left(1 + 0.0652\left(\frac{d_s}{2\delta}\right)^{4.0685}\right)^{\frac{1}{\pi}} \tag{1.10}$$

For instances where the skin-depth is very small compared to the radius of the conductor ($d_s > 8\delta$), the AC resistance per-unit-length can be approximated by computing the DC resistance of a tubular conductor with wall thickness equal to δ,

$$R_{AC} = \frac{\rho}{\pi\delta(d_s - \delta)} \tag{1.11}$$

1.4.2 Proximity Effect

Similarly, their exists an exact solution to the current density distribution and power loss in a solid cylindrical conductor due to a uniform external alternating and transverse magnetic field. While the proximity effect between strands within a bundle is complex due to a non-trivial field distribution, the uniform field assumption is more applicable for turn-to-turn and coil-to-coil proximity effect analysis. Because there is no current injection, the exact solution is expressed in terms of AC power loss instead of AC resistance. The solution is again written in terms of Bessel functions as [17,54],

$$P_{AC} = 2\pi\rho L H_0^2 \Re\mathrm{e}\left\{\frac{kd_s}{2}\frac{J_1\left(\frac{kd_s}{2}\right)}{J_0\left(\frac{kd_s}{2}\right)}\right\} \tag{1.12}$$

where H_0 is the peak magnitude of the external magnetic field uniform along the length, L, of the conductor. With no net transport current, currents travels in opposite directions within the conductor cross-section to oppose the incident and perpendicular changing magnetic field as can be seen in Fig. 1-13 where red and blue hues denote opposite directions and intensity denotes current density magnitude.

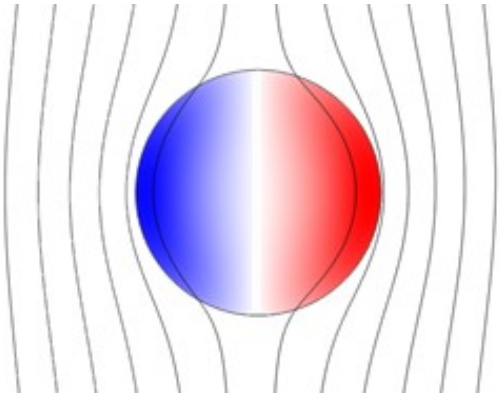

Figure 1-13: Current density distribution in a solid cylindrical conductor due to the proximity effect, blue denotes into the plane, red denotes out of the plane. Black lines are the resultant lines of the magnetic field.

Normalizing the expression for power loss due to the proximity effect by L and H_0^2 gives the proximity loss factor for a solid cylindrical conductor, G_R (plotted in Fig. 1-14). This factor is similar to F_R for the skin-effect in that it provides a value for qualitative comparisons between various geometries.

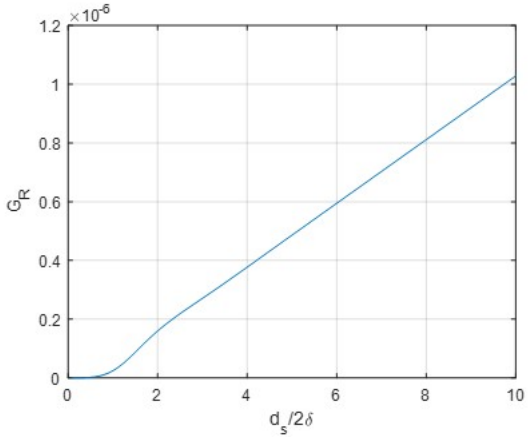

Figure 1-14: Exact proximity loss factor, G_R, calculated from (1.12) for a solid cylindrical conductor plotted against $\frac{d_s}{2\delta}$.

1.4.3 Ferreira's Method

A comparison of several of the most prominent analytical models for ideal Litz wire is provided in [55]. This section gives a detailed description of Ferreira's approach, on of the most commonly cited methods to compute the loss in Litz wire. The Ferreira model was developed to approximate Litz wire losses in a transformer "window". The following assumptions are at the foundation of the method:

1. 2D approximation and perfect twisting of the Litz wire
2. 1D homogeneous applied external field
3. Orthogonality between different loss mechanisms
4. Three different loss types: skin effect, internal proximity effect, and external proximity effect
5. Approximate uniform current density distribution on the cross section of the bundle

Fig. 1-15 shows the geometric definitions used in this description of Ferreira's method.

Assumption 5 is accurate if the Litz wire has a high packing factor β and $\frac{d_s}{2\delta} < 1$. The internal magnetic field is then $\mathbf{H_{int}}(r) = \frac{I}{2\pi r_{Li}^2} r\hat{\phi}$, where $r \in [0, r_{Li}]$ is the distance from the center of the bundle and I is the peak total current through the bundle.

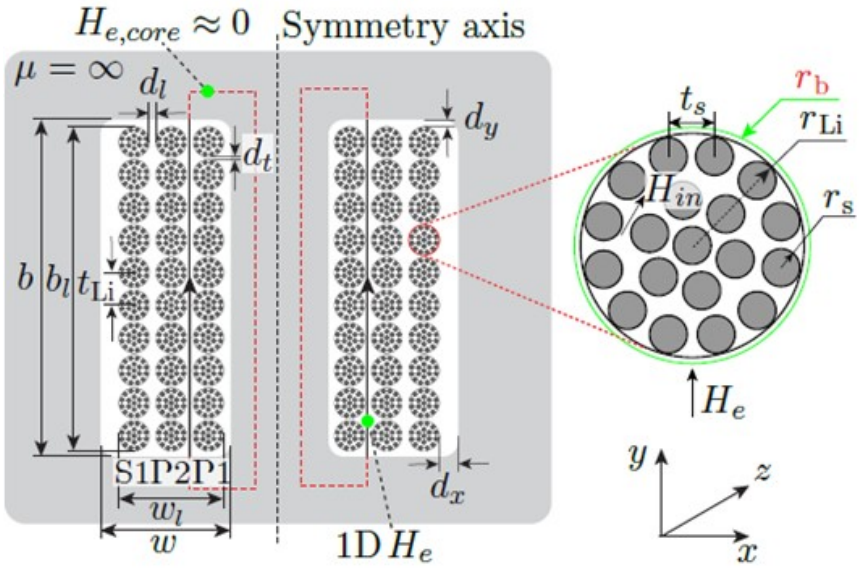

Figure 1-15: Geometric description of a Litz bundle and transformer setup from Meng *et al.*

The total power loss per-unit-length in the Litz wire is a summation of the individual loss components due to orthogonality:

$$P_{tot} = P_{skin} + P_{p,int} + P_{p,ext} \tag{1.13}$$

In general, internal proximity loss in a bundle is calculated by the area integration of the loss density,

$$P_{p,int} = \frac{n_s G_R(f)}{\pi r_{Li}^2} \int_0^{2\pi} \int_0^{r_{Li}} |\mathbf{H_{int}}(r)|^2 r dr d\phi \tag{1.14}$$

where G_R is a frequency dependent multiplicative factor such that the local loss due to proximity effect is $P_p = G_R(d_s, f)[H(r,\phi)]^2$ and n_s is the number of strands in the bundle. Individual loss components are defined as follows using the above assumptions,

$$P_{skin} = R_{DC} F_R(f) \frac{1}{2} I^2 = \frac{4\rho_{cu}}{n_s \pi d_s^2} F_R(f) \frac{1}{2} I^2 \tag{1.15}$$

$$P_{p,int} = n_s G_R(f) \Big[\frac{I^2}{8\pi^2 r_{Li}^2} \Big] \tag{1.16}$$

$$P_{p,ext} = n_s G_R(f) H_e^2 \tag{1.17}$$

where ρ_{cu}, n_s, d_s, F_R, and H_e are copper resistivity, total number of strands in the bundle, strand diameter, skin effect resistance ratio, and peak external transverse magnetic field respectively. The resistance ratio and proximity factor are written in terms of Kelvin functions (definitions of which can be found in Appendix A),

$$F_R(f) = \frac{\gamma_s}{2} \frac{ber(\gamma_s) bei'(\gamma_s) - bei(\gamma_s) ber'(\gamma_s)}{ber'^2(\gamma_s) + bei'^2(\gamma_s)} \tag{1.18}$$

$$G_R(f) = 2\pi\gamma_s\rho\frac{ber_2(\gamma_s)ber'(\gamma_s) + bei_2(\gamma_s)bei'(\gamma_s)}{ber^2(\gamma_s) + bei^2(\gamma_s)} \tag{1.19}$$

where $\gamma_s = \frac{d_s}{\sqrt{2}\delta}$. To calculate the power loss due to external proximity effect, we must know the magnitude of the homogeneous external magnetic field, which is generated by adjacent bundles. For a single-layer coil, Ferreira approximates this external field as the average along the coil length,

$$H_e = \frac{N_t I}{2b} \tag{1.20}$$

where N_t is the number of turns in the single layer coil and b is the length of the coil. Most subsequent models follow Ferreira until the approximation of the external magnetic field. Finally, the AC resistance per-unit-length of the coil is calculated from the total power loss as,

$$R_{AC} = \frac{2P_{tot}}{I^2} \tag{1.21}$$

Proposed Modification for a Single Layer of Pre-formed Sub-bundles

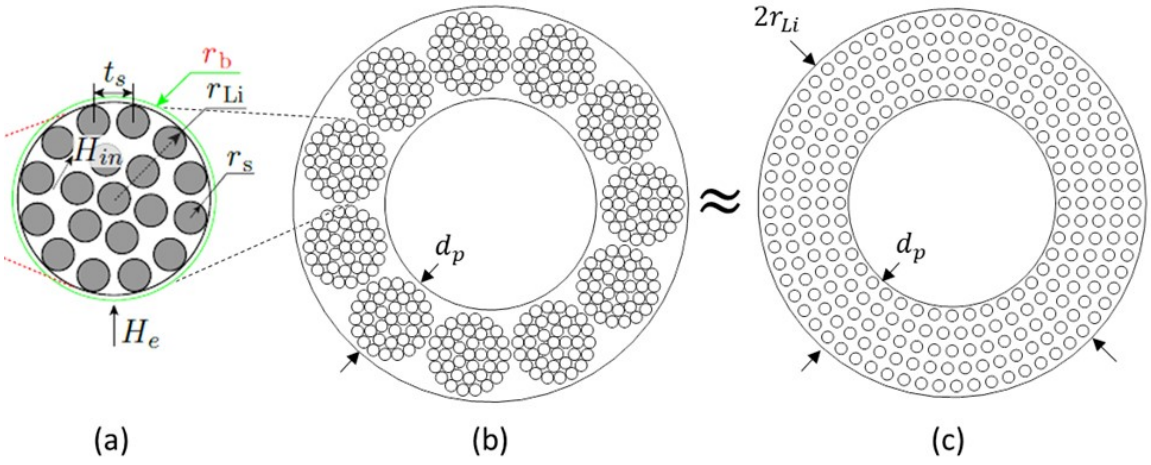

Figure 1-16: (a) Ferreira basic uniformly packed Litz representation, (b) single-layer of uniformly packed pre-formed Litz bundles, (c) an approximation that compresses the pre-formed bundles into an annulus, with reassigned geometric definitions.

If the overall bundle cross section does not have a high packing factor (single-layer of $N_p > 5$ pre-formed bundles creates an annulus) but each closely packed sub-bundle has a high packing factor and $\frac{d_s}{2\delta} < 1$, then the current can be approximated as uniformly distributed throughout the annulus, as shown in Fig. 1-16. Here, the term r_{Li} refers to the radius of the single-layer bundle of pre-formed Litz wire. This compression from pre-formed bundles into equidistantly placed strands (same number) in the annulus is made so that we can approximate the internal magnetic field as before with a slight modification. The internal magnetic field in the annulus in Fig. 1-16(c)

becomes,

$$\mathbf{H_{int}}(r) = \frac{I\left[r^2 - (r_{Li} - d_p)^2\right]}{2\pi r(2r_{Li}d_p - d_p^2)}\hat{\phi} \tag{1.22}$$

where d_p is the diameter of the pre-formed bundle and $r \in [(r_{Li} - d_p), r_{Li}]$. The power loss due to internal proximity effect then becomes,

$$P_{p,int} = \frac{n_s G_R(f) I^2}{2\pi^2(2r_{Li}d_p - d_p^2)^3} \int_{r_{Li}-d_p}^{r_{Li}} \frac{\left[r^2 - (r_{Li} - d_p)^2\right]^2}{r} dr \tag{1.23}$$

As long as $r_{Li} > d_p$ (which should always be true), the definite integral can be written explicitly such that the entire expression for the power loss per-unit-length due to internal proximity effect becomes,

$$P_{p,int} = \frac{n_s G_R(f) I^2}{2\pi^2(2r_{Li}d_p - d_p^2)^3} \left\{ (r_{Li} - d_p)^4 \left[\ln\left(\frac{r_{Li}}{r_{Li} - d_p}\right) + \frac{3}{4} \right] + \frac{r_{Li}^2\left[r_{Li}^2 - 4(r_{Li} - d_p)^2\right]}{4} \right\} \tag{1.24}$$

The skin and external proximity effect power loss calculations should remain unchanged from the original Ferreira formulation.

Chapter 2

Solid Conductor Coil Variations

When choosing between two conductor configurations for a given application, intuition would lead one to believe the conductor with more copper volume will cost more. This is generally true for "like" conductors, however, at some point the complexity of, for example, a stranded conductor, may eclipse the material difference as the dominate cost factor. For this reason, minimizing the complexity of a conductor's geometry can be seen as a cost reduction task and is especially important in industrial applications such as transformers, whose large-scale economics demand low costs to facilitate market proliferation.

This chapter focuses on simple, solid conductor coils and varying their cross-sectional parameters in order to maximize performance. To properly compare between different geometries, these studies use the same centerline axis of each turn in the previously built 40 kW MIT transformer's coils to ensure generally equivalent magnetic performance. Through this analysis, one may draw conclusions about the extent to which varying the cross-sectional geometry of a solid conductor coil may improve the high frequency transformer's performance over a baseline circular cross-section design. Because at high frequencies, the AC transport current is mainly distributed within one skin-depth of the conductor's outer surface, one may hypothesize that in order to minimize losses in a transformer using solid conductors, one only needs to maximize the cross-sectional perimeter of the conductor. However, as will be observed in this chapter, maximizing the perimeter of a coil's cross-section actually degrades performance due to the increasingly close proximity of adjacent turns.

2.1 Elliptical Cross-section

A generalization of the circular cross-section solid conductor coil is an elliptical cross-section coil. All analysis in this study was performed in COMSOL Multiphysics, simulating the full transformer operation. Loss was computed through post-processing on the simulation results and was swept over 150 kHz range with inclusion of the transformers nominal operating frequency, 300 kHz. It should be noted that while the efficiencies peak at a lower frequency, the S_{21} energy transfer parameter peaks at 300 kHz. This provides the best instance of coupling between the drive and load

coils.

For comparisons to the solid conductor transformer already built out of circular cross-section conductors, there are several ways to modify the elliptic cross-section. First, we must establish an eccentricity parameter defined by,

$$E = \sqrt{1 - \frac{b^2}{a^2}} \tag{2.1}$$

where a and b are the major and minor axis radii of the cross-section, respectively. With the eccentricity allowed to vary between 0 and 1, the cross-section can be oriented such that the major-axis points radially outward from the coil centerline. If we apply the eccentricity metric uniformly to each coil and constrain the total cross-sectional area to be equal to the 40 kW circular cross-section solid conductor transformer coils for equivalent DC resistance, then the major radius of the resulting conductor can be calculated as a function of the corresponding circular conductor diameter, d_w, and the eccentricity,

$$a = \frac{d_w}{2\sqrt[4]{1 - E^2}} \tag{2.2}$$

Similarly, the minor radius can be calculated as,

$$b = \frac{1}{2} d_w \sqrt[4]{1 - E^2} \tag{2.3}$$

This case was analyzed in 2D axisymmetric FEA for several eccentricity values and the results are shown in Fig. 2-1. Note that the $E = 0$ variant is the same as the original 40 kW transformer.

Both eccentricity extremes perform slightly worse, however, a small improvement is observed over the original geometry ($E = 0$) for some of the mid-eccentricity values. The minimal performance benefit is most likely not worth the extra cost of the unique cross-sectional geometry.

A similar approach can be made, but now constraining the major axis to point axially, or in parallel with the coil centerline. Still keeping the cross-sectional areas the same, the definitions for the major and minor radii are swapped,

$$a = \frac{1}{2} d_w \sqrt[4]{1 - E^2} \tag{2.4}$$

$$b = \frac{d_w}{2\sqrt[4]{1 - E^2}} \tag{2.5}$$

The results of this analysis are shown in Fig. 2-2. Here there is a clear disadvantage to increasing the eccentricity of the cross-section. The circular cross-section of the original transformer performs the best.

The results of the above analysis suggests that inter-coil turn spacing can have a large impact on the efficiency of the transformer. If we were to now let the cross-sectional area grow but maintain the spacing between copper edges of adjacent turns

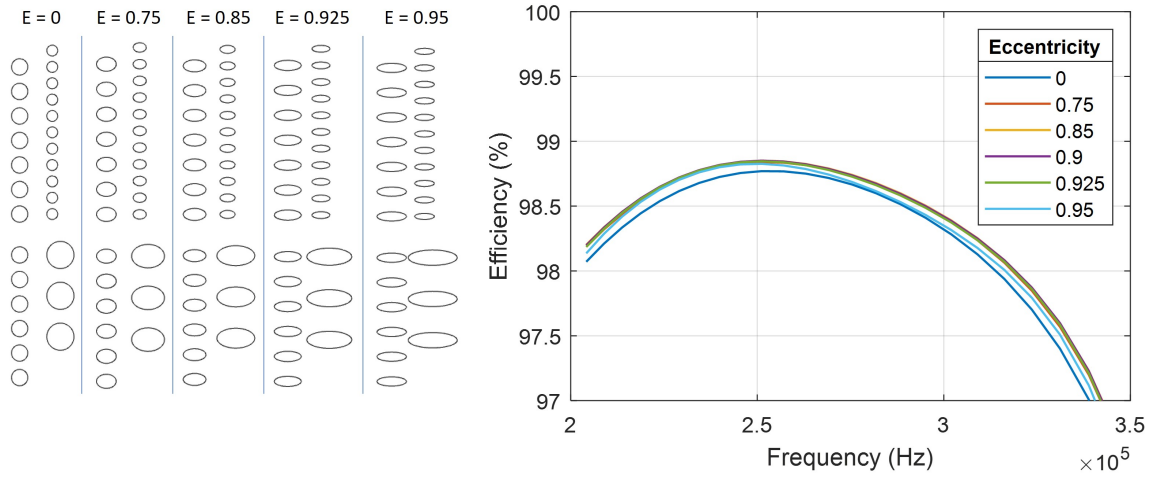

Figure 2-1: (left) Axisymmetric cross-sectional geometry of the 40 kW transformer with varying eccentricity values when the coil cross-sectional areas are constrained to be equivalent to the original 40 kW transformer and the major axis points radially outward from the coil centerline (right) 2D axisymmetric FEA results for efficiency of each variation over a 150 kHz frequency range.

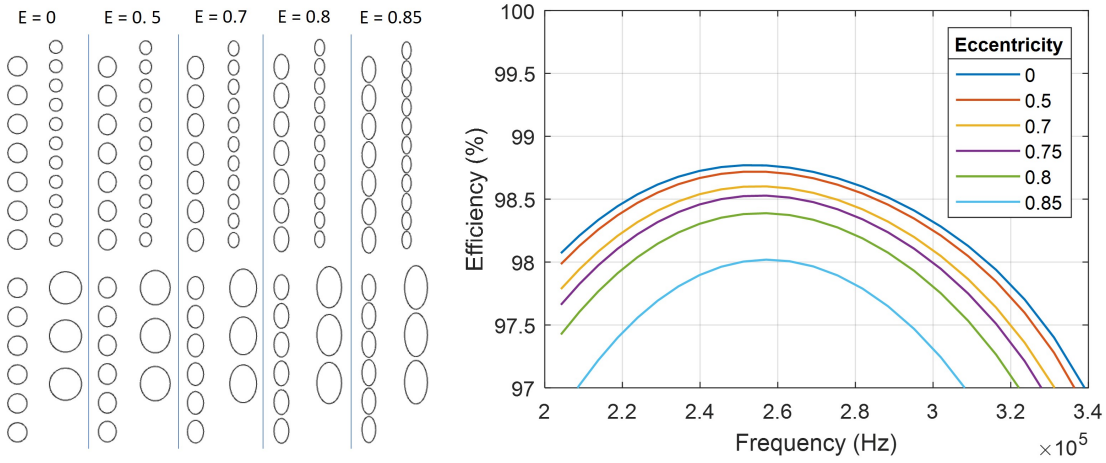

Figure 2-2: (left) Axisymmetric cross-sectional geometry of the 40 kW transformer with varying eccentricity values when the coil cross-sectional areas are constrained to be equivalent to the original 40 kW transformer and the major axis points axially, in parallel with the coil centerline (right) 2D axisymmetric FEA results for efficiency of each variation over a 150 kHz frequency range.

in each coil, perhaps we may achieve a substantially higher efficiency. This approach inherently constrains the major axis of the cross-section to point radially and fixes the minor radius to half the of the original circular conductor diameter,

$$b = \frac{d_w}{2} \tag{2.6}$$

and the major radius is then calculated from the minor radius and the eccentricity,

$$a = \sqrt{\frac{b^2}{1 - E^2}} \tag{2.7}$$

The results of this study (shown in Fig. 2-3) are surprising. Even with increased cross-sectional area of each conductor in the transformer, no significant improvement is seen over the original circular cross-section design. This makes it clear that the efficiency is dependent on turn spacing relative to every adjacent turn in the transformer and not just inter-coil turn spacing

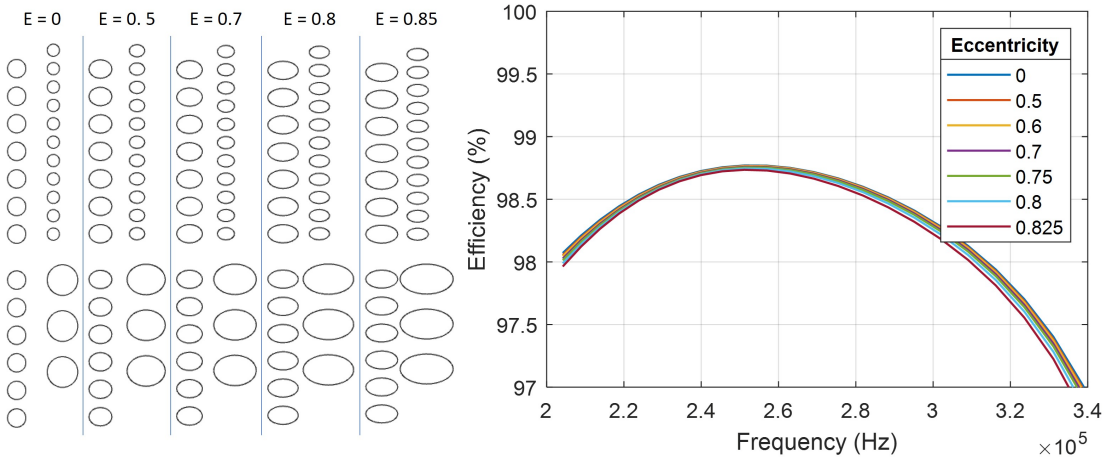

Figure 2-3: (left) Axisymmetric cross-sectional geometry of the 40 kW transformer with varying eccentricity values when the inter coil turn spacings are constrained to be equivalent to the original 40 kW transformer and the cross-sectional area is allowed to grow with eccentricity (right) 2D axisymmetric FEA results for efficiency of each variation over a 150 kHz frequency range.

2.2 Rectangular Cross-section

A similar study was performed with rectangular conductor cross-sections. Here, the aspect ratio defines the severity of the rectangular shape,

$$AR = \frac{L_1}{L_2} \tag{2.8}$$

where L_1 is the larger side length and L_2 is the smaller side length. With the cross-sectional area again held constant and equivalent to the respective coils in the 40 kW circular cross-section transformer,

$$L_1 = \frac{1}{2} d_w \sqrt{AR\pi} \tag{2.9}$$

$$L_2 = \frac{1}{2} d_w \sqrt{\frac{\pi}{AR}} \tag{2.10}$$

the aspect ratio was varied and analyzed over several frequencies. The first case studied is with the longer side pointing radially outward from the coil centerline. The results of this study are shown in Fig. 2-4.

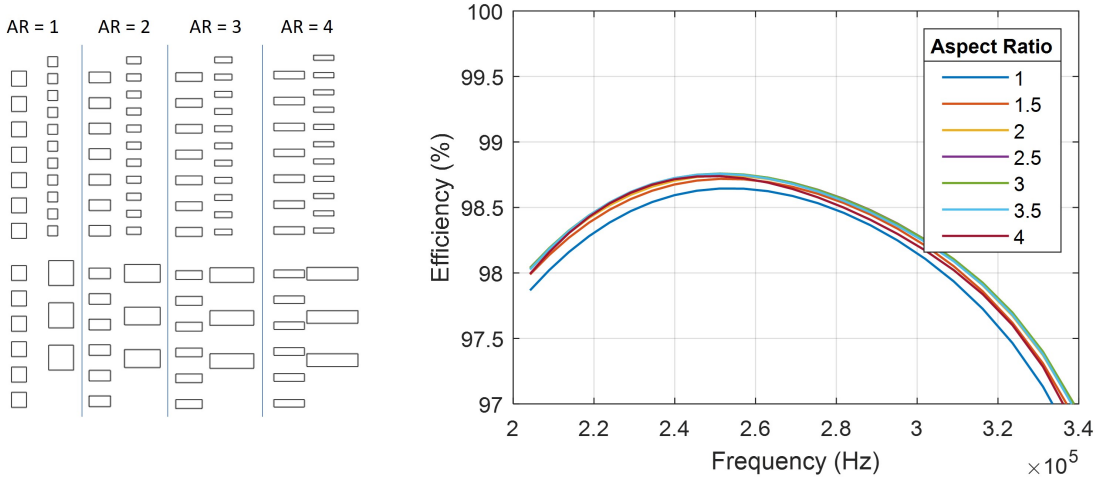

Figure 2-4: (left) Axisymmetric cross-sectional geometry of the 40 kW transformer with varying aspect ratios when the longer side points radially outward from the coil centerline and the cross-sectional areas are constrained to be equivalent to those of the original 40 kW transformer (right) 2D axisymmetric FEA results for efficiency of each variation over a frequency range.

A slight benefit comes with an aspect ratio close to 3.5 over the square ($AR = 1$) case, however, it should be noted that all curves are at or below the original circular cross-section design. In the next study, the longer side is oriented parallel to the coil centerline and the aspect ratios are again varied with the cross-sectional area remaining same. The results of this study are shown in Fig. 2-5.

A clear and significant performance drop is observed with increasing aspect ratios in this orientation. This is therefore not a viable option likely because of the close inter coil turn spacing that results from the geometric setup. The final option studied is to keep the same inter coil turn spacing as in the circular conductor transformer such that,

$$L_2 = d_w \tag{2.11}$$

$$L_1 = (AR) L_2 \tag{2.12}$$

and allow the cross-sectional area to grow with the uniformly applied aspect ratio. The results of this study are provided in Fig. 2-6. And show a significant reduction in performance for nearly all aspect ratios. This, together with Fig. 2-5, suggests that the most important factor in the rectangular cross-sectional conductor designs performance is the inter coil turn-to-turn spacing. This is most likely because, due to the skin-effect, the current is mostly carried within a skin-depth from the surface

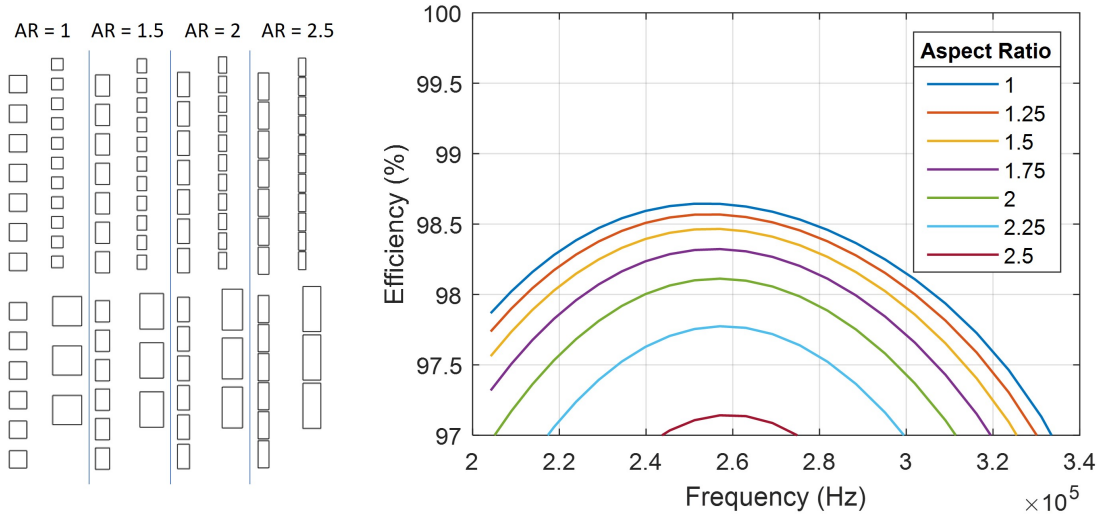

Figure 2-5: (left) Axisymmetric cross-sectional geometry of the 40 kW transformer with varying aspect ratios when the longer side points axially, or parallel to the coil centerline and the cross-sectional areas are constrained to be equivalent to those of the original 40 kW transformer (right) 2D axisymmetric FEA results for efficiency of each variation over a frequency range.

of the smaller side of the rectangle. Keeping the inter coil turn spacing the same and increasing the aspect ratio does not change this current distribution.

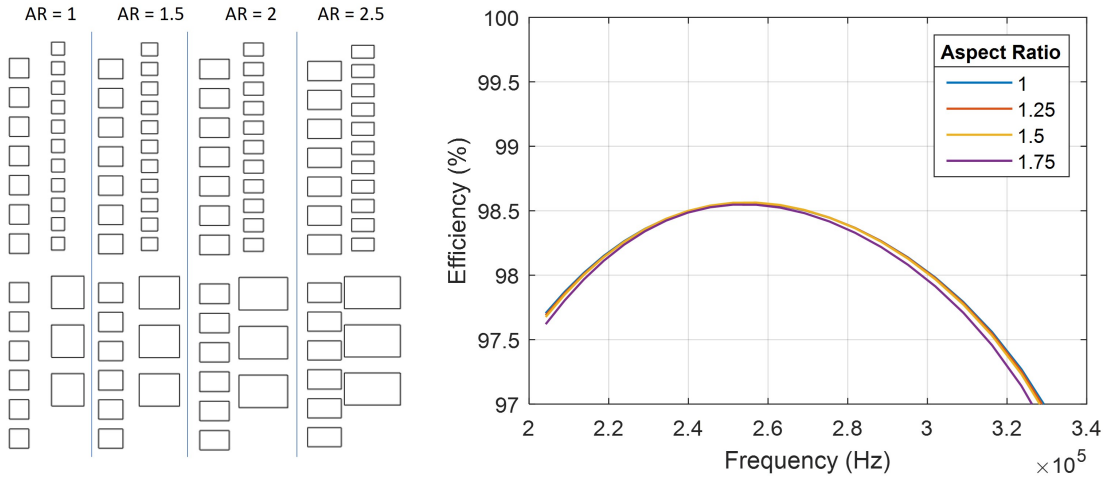

Figure 2-6: (left) Axisymmetric cross-sectional geometry of the 40 kW transformer with varying aspect ratios when the inter coil turn spacings are constrained to be equivalent to the original 40 kW transformer and the cross-sectional area is allowed to grow with aspect ratio (right) 2D axisymmetric FEA results for efficiency of each variation over a frequency range.

From both the elliptical and rectangular cross-section variation studies, no signif-

icant improvement over the circular cross-section was observed that would warrant switching to a new geometry. The circular cross-section is nearly the best that a solid conductor coil can provide in terms of performance. To get significantly higher efficiencies a more complex geometry conductor must be used by introducing stranding and transposition. This is the focus of the next chapter.

Chapter 3

Stranded Conductor Theory

The concept of using Litz wire to reduce AC associated losses was introduced nearly a century ago for radio applications [56]. The idea being that by breaking up a conductor into smaller insulated filaments or strands and using proper transposition, every strand in the conductor will see the same resistance over the lay. This means that the current is evenly distributed over the cross-section and the effective resistance is reduced.

Litz wire began attracting more interest in recent years as wide-band gap (WBG) power semiconductors became an enabler for several high frequency, high power technologies, such as induction cooktops [10,22,23], EV wireless power transfer [24–27,57], megawatt-class electric machines [28–33], and resonant power transformers [1, 2]. Many modeling approaches have been proposed for the optimization of Litz coil efficiency. Several analytical methods were established in the literature over the decades [3, 5, 6, 9, 48, 58] all aimed at quick performance approximations. For more detailed predictions, three-dimensional numerical methods have been employed such as FEA [11–14] and the more novel PEEC method [15–19] which does not require the discretization of air. These 3D approaches are accurate given knowledge of the exact strand level construction, but suffer from computational limitations (memory, complexity, and long simulation times) due to the large number of mesh elements required. In this chapter, two new approaches to estimate losses with greater accuracy are presented.

3.1 General Assumptions

The most universal assumption made during Litz wire loss analysis in the literature as well as in the following text is that the strand diameter is much smaller than the spatial variation of the magnetic field. This means that the magnetic field local to any strand is approximately uniform and transverse. Many other modeling approaches make the assumption that the conductors are perfectly Litzed. Meaning every strand is radially and azimuthally transposed such that each strand is in each position of the bundle cross-section for equal time over the twist pitch. This leads to the ideal

assumption that every strands carries the same amount of current, I_s,

$$I_s = \frac{I_{tot}}{N_s} \tag{3.1}$$

where I_{tot} is the total current in the bundle and N_s is the number of strands in the bundle. The work described in Section 3.4 removes this assumption and generates a more realistic current distribution in the cross-section and therefore more accurate approximations of the internal proximity fields. However, Section 3.5 does utilize the "perfect Litz" assumption in order to simplify analysis.

3.2 Single-level Annular Bundle (SLAB)

The single-level annular bundle (SLAB) stranded conductor offers loss reduction with a simple geometry and has potential to be a cost-effective solution. Current manufacturing techniques are not built around this geometry; however, the bundle structure is a good compromise between loss reduction in applications experiencing heavy proximity-effect and material usage. In addition, the geometry is similar to armoured cabling in some power transmission lines [59] which suggests that manufacturing this type of conductor may be reasonable. To achieve clarity in this analysis, the following section will provide definitions for the SLAB geometry and macro definitions used for a solenoid application.

3.2.1 Problem Geometry

Three variables fully define the SLAB structure: strand diameter (d_s), number of strands (N_s), and insulation factor (F_{ins}). A diagram of the geometry is given in Fig. 3-1.

The insulation factor is defined fracionally such that the insulation thickness is $F_{ins}d_s$. If we constrain the design space by forcing the insulation surfaces of adjacent strands to be tangent to one another and take the insulation media to be free space, the insulation factor may be thought of as a spacing factor. Whether the space is taken up by air or the enamel insulation of magnet wire, the magnetic field and current distributions are only dependent upon the copper geometry. The diameter, d_{bos}, of the imaginary circle tangent to the outer copper surface of the strands is written as,

$$d_{bos} = \frac{d_s\left[1 + 2F_{ins} + \sin\left(\frac{\pi}{N_s}\right)\right]}{\sin\left(\frac{\pi}{N_s}\right)} \tag{3.2}$$

As a baseline application, a single solenoid provides a platform to analyze the various forms of proximity-effect loss (internal and external) and skin-effect loss. Fig. 3-2 shows the macro geometric definitions of a solenoid utilizing the SLAB structure.

Again, here three parameters fully define the solenoid structure: coil diameter measured from the center of each conductor bundle (D_c), number of turns in the coil

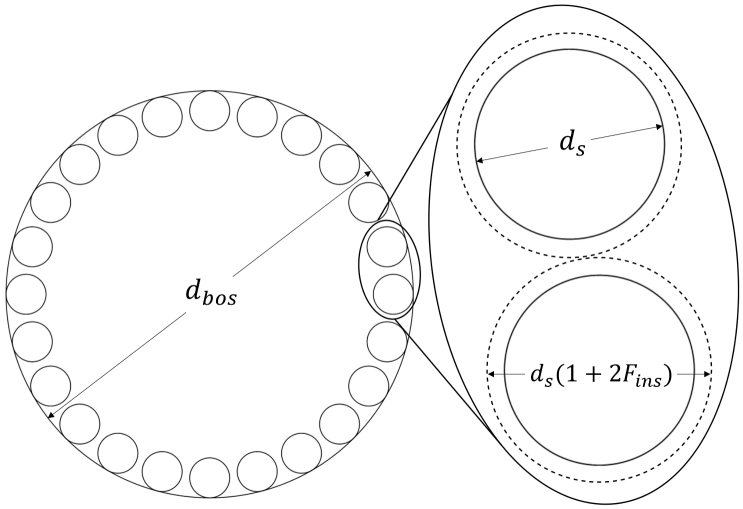

Figure 3-1: Geometric definitions for the SLAB structure. Two-strands are shown in an expanded view for simplicity.

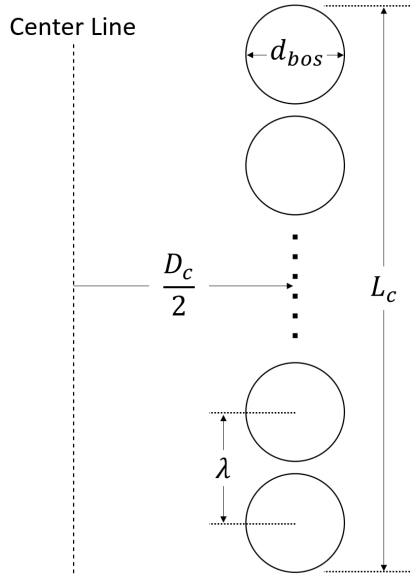

Figure 3-2: Geometric definitions of a solenoid utilizing the SLAB conductor.

(N_t), and turn-to-turn spacing factor (c/a). The spacing factor scales the pitch of the coil, λ, by the bundle OD,

$$\lambda = \left(\frac{c}{a}\right) d_{bos} \tag{3.3}$$

3.2.2 Resistance and Inductance Analysis

A combination of analytical and FEA tools are used here to extract resistance values for coils with varying SLAB and solenoid geometries. The goal of this analysis is to observe the effect each of the many defining parameters has on the overall coil

resistance. The open-source software FEMM [36] was used for this analysis due to its tight scripting integration with MATLAB/Octave and the complex geometry of the problem. Care was taken to minimize simulation time as many combinations of the defining parameters require analysis. Additionally, the number of mesh elements scales with the product of N_s and N_t. Some simplifications were made to the simulation setup to accommodate these practical considerations:

S1) A 2D axisymmetric magnetoquasistatic simulation

S2) Each turn is approximated as a hoop (there is no out-of-page component to the magnetic field)

S3) Each strand is placed in series so as to carry the same amount of peak current: I_{tot}/N_s

Simplification S3) is made to simulate the effect of azimuthal transposition, or twisting, in the bundle. The flux linkage generated from external fields cancels out by twisting an integer number of times per-turn [15], therefore each strand sees the same average field between the conductor's terminals.

For performance comparisons with solid cylindrical conductor coils, d_{bos} is set to the OD of an equivalent solid conductor. The strand diameter was then varied from 22-42 AWG and as many strands plus insulation as possible were fit into the bundle for each strand size. The number of stands is calculated by,

$$N_s = \left\lfloor \pi \left[\sin^{-1}\left(\frac{d_s(1+2F_{ins})}{d_{bos}-d_s} \right) \right]^{-1} \right\rfloor \tag{3.4}$$

Note: the floor in (3.4) means that our insulation surfaces are no longer constrained to touch, since now the insulation factor has physical meaning.

After running an FEA simulation, the total power loss in the coil is calculated by computing the time-averaged resistive losses over the entire domain,

$$P_{tot} = \frac{1}{T}\int_0^T \Re\mathrm{e}\left\{ \iiint_V \mathbf{J}\cdot\mathbf{E} \right\} dt \tag{3.5}$$

From this, the total AC resistance per-unit-length can be extracted,

$$R_{AC,tot} = \frac{2P_{tot}}{\pi I_{tot}^2 N_t D_c} \tag{3.6}$$

By simulating a straight, isolated SLAB conductor, we can compute the resistance only due to strand-level skin-effect and internal proximity effect. Subtracting this resistance from the total resistance found in the coil simulations singles out the resistance due to turn-to-turn proximity effect. This value is of interest to us, as it is what the SLAB structure seeks to minimize.

A method widely used in the literature, developed by Nagaoka [60] as a modification of Lorenz' formulation, predicts the inductance of short solenoids by approxi-

mating the coil as a cylindrical sheet of current, Nagaoka's equation for inductance, L, is written as,

$$L = \frac{\mu_0 \pi D_c^2 N_t^2}{4 L_c} K_n \tag{3.7}$$

where L_c is the coil length, measured from the outer conductor edges of the first and last turns (as shown in Fig. 3-2). The Nagaoka factor, K_n, is defined in terms of coil dimensions and elliptical integrals of the first and second kind, K and E respectively, definitions of which can be found in the Appendix.

$$K_n = \frac{4}{3\pi k'} \left[\frac{k'^2}{k^2} \big(K(k) - E(k) \big) + E(k) - k \right] \tag{3.8}$$

where the geometric factor, k, is written as,

$$k = \frac{1}{\sqrt{1 + \left(\frac{L_c}{D_c}\right)^2}} \tag{3.9}$$

and its dual,

$$k' = \sqrt{1 - k^2} \tag{3.10}$$

From FEA, inductance is calculated in the software as,

$$L = \frac{1}{I_{tot}^2} \Re\mathrm{e} \left\{ \iiint_V \mathbf{A} \cdot \mathbf{J} dV \right\} \tag{3.11}$$

where I_{tot} is the peak total current through the bundle, V is the 3D simulation domain, $\mathbf{A}$ is the local magnetic vector potential at peak current, and $\mathbf{J}$ is the local current density at peak current.

3.2.3 Resistance and Inductance Analysis Results

The coil macro parameters given in Table 3.1 were used to demonstrate the various resistive contributions for a SLAB conductor compared to a solid cylindrical conductor with the same OD.

Table 3.1: Baseline Coil Parameters

Parameter	Value
d_{bos}	0.25"
D_c	11.25"
N_t	6
c/a	2
f	300 kHz

Performing the analysis as previously described gives the total AC resistance of

the SLAB coil. By subtracting the total AC resistance from the AC resistance of the same conductor but straight and isolated, we can extract out the resistance due to proximity effect. The resistive components are broken down and plotted together with those of an equivalent solid cylindrical conductor in Fig. 3-3.

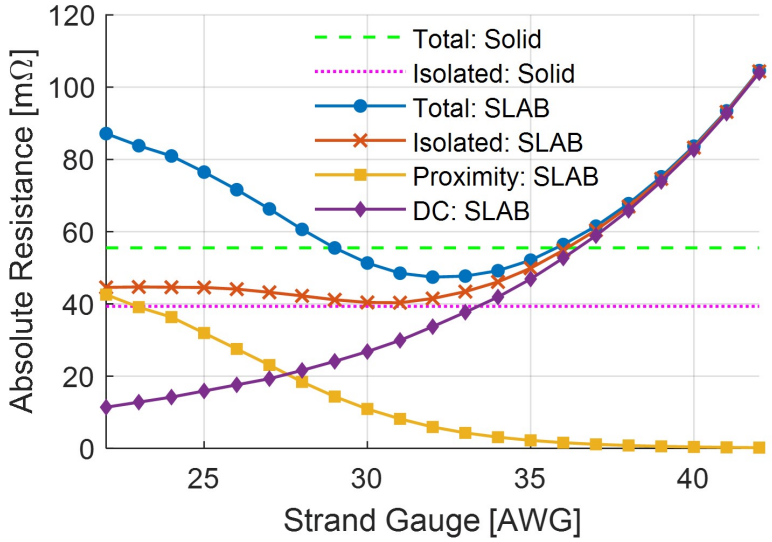

Figure 3-3: Coil absolute resistances with breakdown of contributing loss mechanisms.

As can be seen, the isolated SLAB resistance never goes below an equivalent isolated solid conductor resistance. This is because there is no radial transposition in the SLAB conductor. The benefit of a SLAB is solely in the reduction of turn-to-turn proximity resistance. The proximity resistance decreases as the strand diameter is decreased (at a fixed frequency) and eventually the total resistance is asymptotic to the SLAB's DC copper resistance. This happens as the total copper area decreases and the strand diameters are significantly smaller than the skin-depth.

The benefit of SLAB conductors is exaggerated at closer turn-to-turn spacing. Fig. 3-4 shows the minimum total AC resistances of the coil analyzed in Fig. 3-3 but with different c/a spacing factors. Each resistance is normalized to an equivalent solid conductor coil. At the lower limit ($c/a = 1$), the best SLAB total resistance approaches half that of an equivalent solid conductor coil, and at the upper limit ($c/a \to \infty$) the SLAB and solid conductor will have the same AC resistance.

To explore the design space, a number of coil parameter combinations were analyzed. The strand gauge in each coil is increased until the total resistance turns up again. The minimum total resistance is recorded for that coil and operating conditions. Table 3.2 gives the variables and their respective values. All combinations were simulated for a total of 324 operating points. The insulation factor was fixed at $F_{ins} = 0.05$.

An approximate analytical expression for the minimum total AC resistance of a coil given it's parameters is developed by first taking DC conduction in the skin depth of the bundle and multiplying by strand-level skin-effect and turn-to-turn proximity-

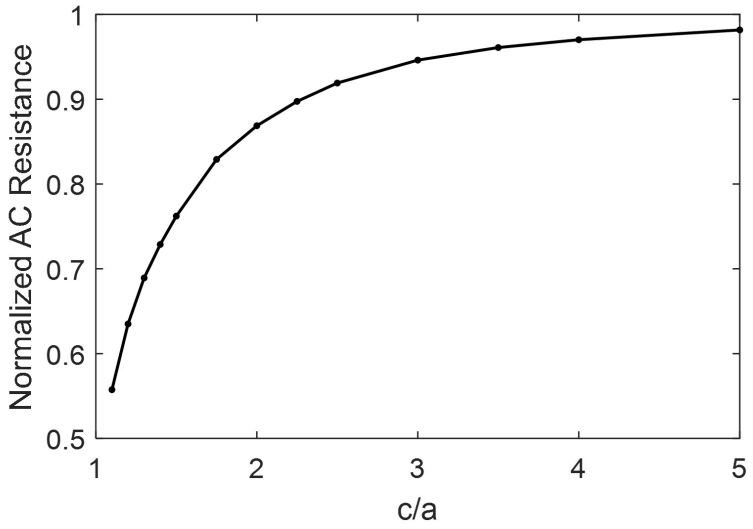

Figure 3-4: Minimum resistance vs. c/a for the best performing SLAB conductors. Resistance is normalized to that of an equivalent solid conductor coil.

Table 3.2: Coil Parameter Space

Parameter	Values
D_c	[0.2, 0.25, 0.3, 0.35] m
c/a	[1.5, 2, 2.5]
N_t	[3, 6, 7]
f	[200, 300, 400] kHz
d_{bos}	[0.162, 0.25, 0.375] in

effect correction factors. The resulting expression is,

$$R_\theta = \left(e^{-\left(\frac{c}{a}\right)} + \sqrt{1 + \frac{1}{4}\left(\frac{d_s}{2\delta}\right)^2} \right) \frac{\rho N_t D_c}{(d_{bos} - \delta)\delta} \tag{3.12}$$

where the exponential factor is a correction for turn-to-turn proximity. This correction factor fits well for the values of c/a analyzed in this study and meets the isolated conductor boundary condition of $\lim_{c/a \to \infty} e^{-\left(\frac{c}{a}\right)} = 0$. The square root factor,

$$\sqrt{1 + \frac{1}{4}\left(\frac{d_s}{2\delta}\right)^2} \tag{3.13}$$

is a rough approximation of F_R in the region of small $\frac{d_s}{2\delta}$ and therefore adjusts R_θ to consider strand-level skin effect.

Alignment between the AC minimum resistances calculated from FEA simulation results and (3.12) can be seen in Fig. 3-5. Resistances calculated from FEA for all

324 configurations are plotted against the value as approximated by R_θ.

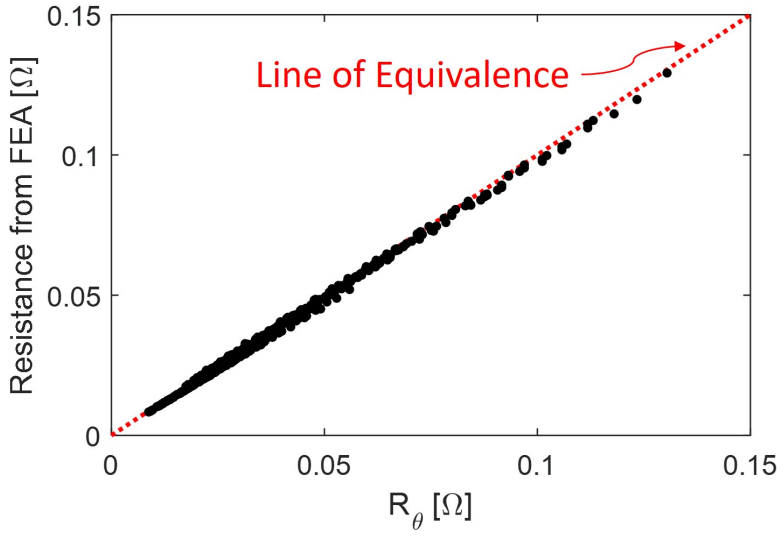

Figure 3-5: Good alignment between the minimum resistances of all parameter combinations calculated via FEA and the analytical expression (3.12).

The error of Nagaoka's analytical expression for solenoid inductance can be large for arrangements in which the current and magnetic field distribution differ greatly from the cylindrical sheet approximation. This non-uniformity is exaggerated in AC solid conductor coils with increasing frequency, increasing turn count, and decreasing c/a spacing.

As Nagaoka's calculation only considers coil macro properties, it is necessary to compare the accuracy of the analytical method for different types of conductors via FEA simulations. Generally, Nagaoka over-estimates the actual coil inductance regardless of the conductor used as can be seen in Fig. 3-6(a), where a coil with parameters shown in Table 3.3 was simulated over a variety of c/a spacing.

The finer stranded SLAB conductors in Fig. 3-4 have slightly larger inductance than the solid conductor coils, especially at smaller c/a, and perform closer to Nagaoka's predictions as shown in Fig. 3-6(b).

Table 3.3: Inductance Study Coil Parameters

Parameter	Values
D_c	30 cm
N_t	6
f	300 kHz
d_{bos}	0.25 in

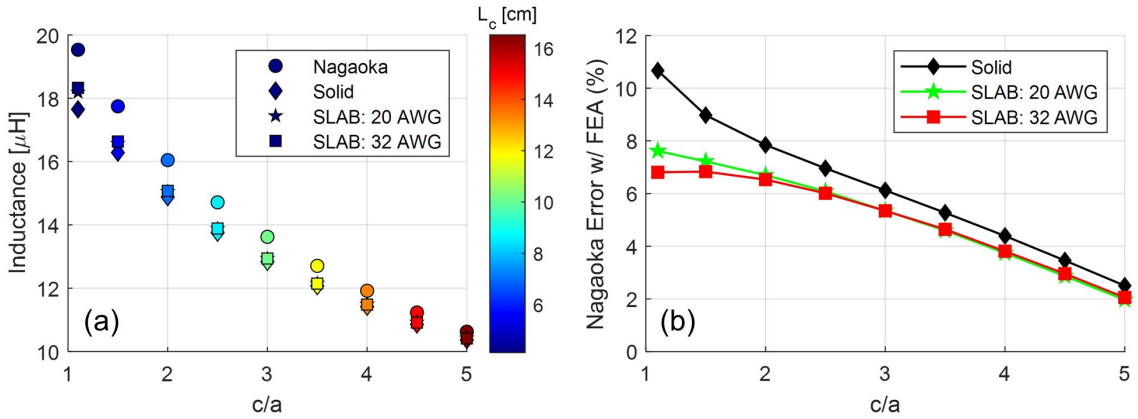

Figure 3-6: (a) Coil inductance for a coil with varying c/a using different conductors. FEA is compared to Nagaoka, (b) Nagaoka inductance calculation error with FEA for a fixed coil at varying c/a spacings.

3.2.4 Proposed Design Method for SLAB Conductors

The presence of a local minimum in the total coil AC resistance for SLAB conductors suggests there is an optimal conductor arrangement for a given application. The designer must take care not to deviate significantly from this minimum or else the full benefit of the SLAB structure is not realized and in some cases may perform worse than an equivalent solid conductor.

Table 3.4 shows the average values of $\frac{d_s}{2\delta}$ that correlates to the minimum resistance in both the isolated case and in a solenoid for several frequencies. The "Total Minimum Resistance" row suggests that the minimum occurs around $\frac{d_s}{2\delta} = 0.81$. Using this information, the following SLAB conductor design method for low loss is proposed by the authors:

1. Choose macro coil parameters and a bundle OD (d_{bos}) that fit the magnetic performance specifications of the application
2. Set $\frac{d_s}{2\delta} = 0.81$ and back out d_s at the operating frequency
3. Calculate N_s based on d_{bos}, the selected d_s, and strand insulation factor (F_{ins}) using (3.4)
4. Predict R_{AC} of the coil with the analytical expression (3.12)

This analysis demonstrated that SLAB conductors are capable of achieving a nearly 50% reduction in AC resistance over a solid conductor with an equivalent outer diameter at 300 kHz and close spacing. The benefits of SLAB conductors are enhanced at close turn-to-turn spacing and at higher frequencies. This benefit is supplemented by lower copper usage, a flexible bundle, and much simpler construction and manufacturing practice compared to commonly used Litz wire. The SLAB conductor may be attractive to utility companies looking to replace their distribution transformers with promising high frequency, coreless resonant transformers, as the

Table 3.4: Minimum Resistance Point for Varying Frequencies

Specification		100 kHz	200 kHz	300 kHz	400 kHz	500 kHz
Isolated	Value	24.0	33.2	40.3	46.5	51.8
Minimum	AWG	26	29	30.5	31.5	33
Resistance	$d_s/2\delta$	0.97	0.97	1	1.02	0.96
Total	Value	27.8	38.7	47.4	54.5	60.8
Minimum	AWG	27	30.5	32	33.5	34.5
Resistance	$d_s/2\delta$	0.86	0.81	0.84	0.81	0.81

bundle structure offers electrical and potential cost benefits that scale well to industrial applications. In addition, the self inductance of SLAB solenoids is always larger than their solid conductor counterparts.

3.3 AC Loss Mechanisms

Nearly all analytical models established in the literature to compute AC loss in Litz wire attempt to take advantage of the exact solution for AC loss in two ideal scenarios: a straight cylindrical conductor carrying sinusoidal transport current and a straight cylindrical conductor placed in a sinusoidally varying homogeneous and transverse magnetic field. These two cases are referred to as skin effect and proximity effect respectively, and the loss in each scenario is computed analytically in terms of Kelvin functions. Both loss mechanisms have been proven to be orthogonal [5] and therefore associated loss can be computed separately and summed up to calculate total AC loss.

A core premise to the calculation is if the AC current carried by every strand in the conductor and the resultant magnetic field amplitude local to every strand is known, then the loss in the Litz wire can be accurately computed with the assumption that the magnetic field applied to each strand is approximately uniform. These fundamental calculations are as follows.

3.3.1 Strand-level Skin-Effect

The current distribution within a straight, cylindrical conductor isolated in free space is known analytically and is used to compute the AC resistance for any strand diameter and current injection frequency. Two ratio parameters are introduced here that will be used to collectively reduce the problem by two dimensions. The first parameter, F_R, is the ratio of the AC resistance due to skin effect to the DC resistance of the conductor [3]. The second parameter, $\frac{d_s}{2\delta}$, is the ratio of the strand diameter to two times the skin-depth. The exact skin effect resistance ratio of the single conductor case is well known [49] and can be expressed in terms of Kelvin functions (definitions

of which can be found in Appendix A) using a slight variation of $\frac{d_s}{2\delta}$, $\gamma_s = \frac{d_s}{\sqrt{2}\delta}$, to simplify the notation,

$$F_R = \frac{\gamma_s}{2} \frac{ber(\gamma_s)bei'(\gamma_s) - bei(\gamma_s)ber'(\gamma_s)}{ber'^2(\gamma_s) + bei'^2(\gamma_s)} \tag{3.14}$$

For a cylindrical strand carrying sinusoidal AC current with amplitude I_{peak}, the power loss per-unit-length due to the skin effect is,

$$P_{skin} = R_{DC} F_R \frac{1}{2} I_{peak}^2 = \frac{4\rho}{\pi d_s^2} F_R \frac{1}{2} I_{peak}^2 \tag{3.15}$$

where ρ is the resistivity of the conductor material.

3.3.2 Strand-level Proximity-Effect

Likewise, for a straight cylindrical conductor present in a homogeneous transverse AC magnetic field, there exists an exact solution to the power loss per-unit-length due to the proximity effect. Similar to F_R, the proximity factor, G_R, is dependent only on the strand geometry, resistivity (ρ), and operating frequency (via its effect on the skin depth, δ). It is defined as [5],[47],

$$G_R = 2\pi\gamma_s\rho \frac{ber_2(\gamma_s)ber'(\gamma_s) + bei_2(\gamma_s)bei'(\gamma_s)}{ber^2(\gamma_s) + bei^2(\gamma_s)} \tag{3.16}$$

The calculation for proximity loss per-unit-length is written in terms of only the proximity factor and the peak amplitude of the applied AC magnetic field, H_{peak},

$$P_{prox} = G_R H_{peak}^2 \tag{3.17}$$

The total loss is the numerical sum of the skin- and proximity effect losses.

$$P_{loss} = P_{skin} + P_{prox} \tag{3.18}$$

3.4 Layered Mesh Approach

There is an element of unknown in the actual construction of Litz wires. A perfect Litz wire is technically possible to make, but the number of cabling operations required to do so renders these conductors economically impractical. Moreover, a DC resistance penalty is incurred with every twisting operation, resulting in a conductor with worse performance than an imperfect Litz wire with fewer fabrication levels. Actual fabrication techniques lead to randomized strand positions and inaccuracies in all of the aforementioned models due to non-idealities in the current distribution. Plumed attempted to address this by introducing some randomization in the strand placement of his simulations [12], but exact packing information is required to model reality. As such, most approaches in the literature use the ideal assumption that each

strand in the bundle carries equal current. The key to improving Litz modeling accuracy is determining the non-ideal current distribution over the cross-section. If the current distribution is known, resultant fields can be computed and used to calculate losses as employed in other methods.

The layered mesh simulation method of Litz conductor loss calculations provides a fast alternative to more computationally intensive three-dimensional simulation methods and accounts for non-idealities in the bundle construction. The method is general enough that it may be applied to arbitrary conductor applications for a given packed layer geometric representation of a Litz bundle. A unique corresponding fabrication factor used in the loss calculation for a given Litz wire is defined, and is a quantity that could be supplied by a manufacturer as obtained from simple isolated conductor tests.

3.4.1 Addressing Non-Ideal Construction

If the conductor of interest is perfectly "Litzed" (every strand spends equal time in every position within the cross-section) over the length of the wire, then each strand carries equal current and the current density in the conductor's cross section is approximately uniform. This case results in several simplifications and is the basic approximation for the majority of analytical methods in the literature [3, 5, 6, 9, 48]. However, manufacturing a perfect Litz wire requires many cabling operations that not only add complexity/cost, but also increase the DC resistance of the conductor. Therefore, a fabrication shortcut called bunching is used in which the base level is composed of many essentially parallel strands that are then packed and twisted together. This operation does not result in full radial transposition for every strand and therefore renders the assumption of uniform current density throughout the cross-section invalid.

Informed Geometry Generation

Litz wire is a multi-level structure consisting of two types of operations: cabling (denoted by 'x' or '()' for served cabling) and bunching (denoted by '/'). Cabling typically happens at the higher levels and is the process of twisting two or more concentric sub-bundles together. To ensure structural integrity and proper azimuthal transposition, the number of sub-bundles cabled at any given level is often limited to about 7 but is sometimes increased at the highest level. The bunched operation is when a given number of strands are collectively twisted without enforcement of full radial transposition. A perfectly "Litzed" wire is constructed using only cabling operations.

As an example, the manufacturing process for a 5x5x42/44 AWG Litz wire in chronological order (lowest to highest level) is: 42 strands of 44 AWG magnet wire are gathered together and twisted, 5 of these bunched bundles of 42 strands are cabled together, and finally 5 of those resulting sub-bundles are cabled together to create a conductor with 1050 total strands. The levels of construction can be seen in the side section view of this conductor in Fig. 3-7(a). As the conductor was ini-

tially served with Nomex insulation, Fig. 3-7(b) shows a highly packed cross-section. Manufacturers typically twist successive cabling operations in opposite directions.

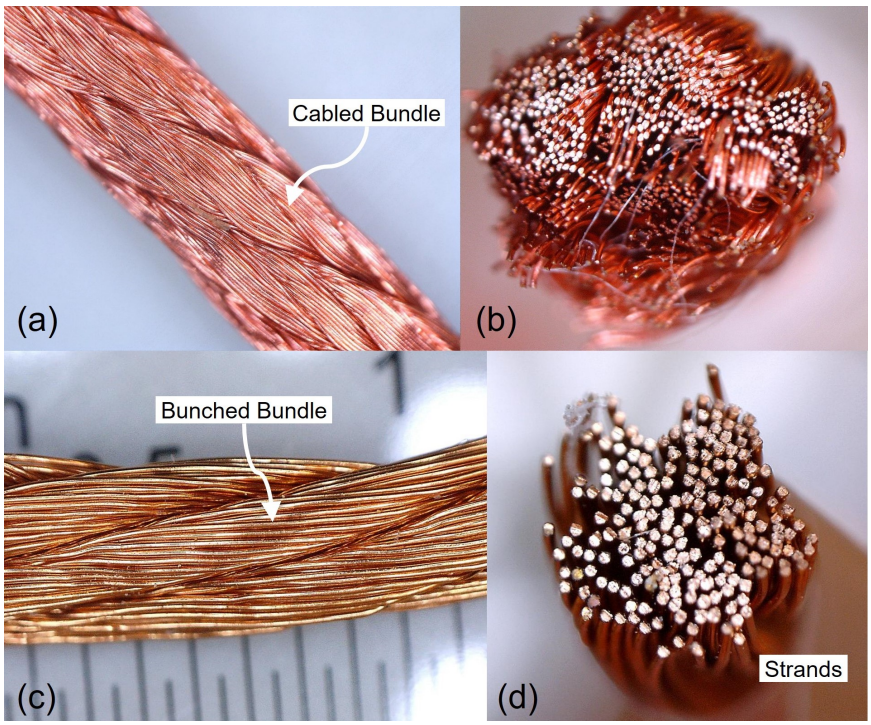

Figure 3-7: Close-ups of both the 5x5x42/44 AWG Litz wire's (a) side view, and (b) cross-section and 5x40/36 AWG Litz wire's (c) side view, and (d) cross-section. Pictures captured after removing the Nomex serving.

The guiding principle of the proposed loss calculation method is to model the non-idealities resulting from the bunching operation and thereby enable unequal current sharing between strands from the ideal assumption of equal distribution, hence affecting the field distribution within the cross-section. All cabling operations are assumed to be perfect, such that each bunched sub-bundle carries equal total current. Because the bunched level is twisted together, each strand at the perimeter should carry the same current. Likewise, each strand in subsequent layers inside the bunched sub-bundle should carry the same current as the others in their layer. This is modeled by creating "concentric" layers of thickness equal to a strand diameter as shown in Fig. 3-8(a). The current density within a layer is approximated as uniform and is to be determined in the following sections.

The sub-bundles are fit into a circular cross-section to simulate a tightly packed conductor. Each packed shape, shown as "triangular" and "rectangular" sectors in Fig. 3-8(a) should have equal area, but the exact geometry is arbitrary. This is because the actual shape after packing is not defined; this variation will be encapsulated in the constant *fabrication factor*.

The 5x5x42/44 AWG Litz wire is a three level construction. The complexity of the packed geometry is more severe with more levels. A two level 5x40/36 AWG Litz

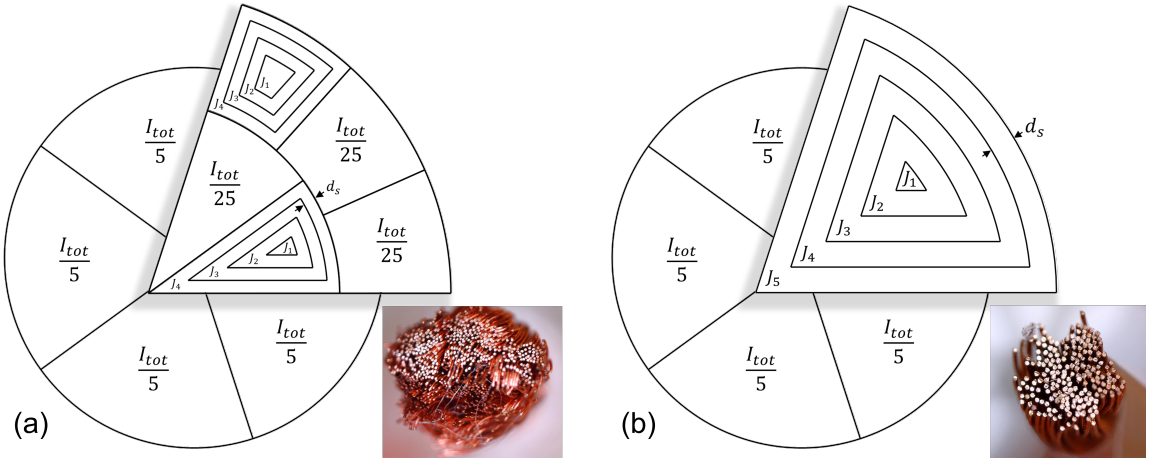

Figure 3-8: Packed layer geometry used for the (a) 5x5x42/44 AWG and (b) 5x40/36 AWG Litz wire analysis; expanded sub-bundles are shown carrying $I_{tot}/5$.

wire example is shown in Fig. 3-7(c-d) and is much simpler to model. The layered mesh packed geometry for this conductor is shown in Fig. 3-8(b).

3.4.2 FEA Simulation Assistance

Surrogate Skin-effect Model

A surrogate cylindrical conductor skin effect model is used to inform and distribute the current in each layer of the layered-model Litz wire cross-section. The surrogate conductor is cylindrical and has a diameter equal to $2md_s$ where m is the number of layers in the bunched level cross-section of interest. Again, the layers have thickness equal to the strand diameter, d_s, as shown in Fig. 3-9.

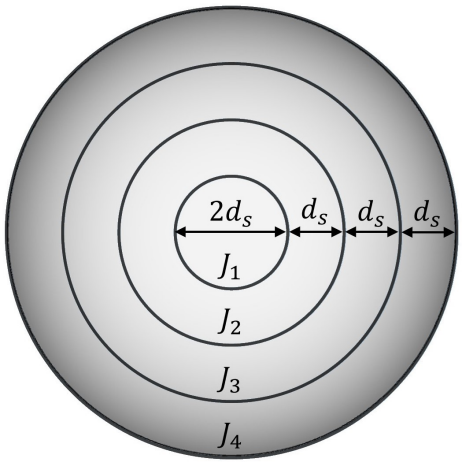

Figure 3-9: Surrogate skin effect model for layered current distribution, $m = 4$.

The current density in each layer is spatially averaged at the excitation frequency of interest as shown. An example of the quantized current density as a function of

radius in the surrogate model is shown in Fig. 3-10. This can be computed from FEA or calculated analytically using the exact solution for the current distribution in an isolated cylindrical conductor carrying sinusoidal transport current. The total current through the surrogate conductor is unimportant since the resulting average current densities will be normalized and used relatively. Therefore, we will set the total peak current through the surrogate model as 1 A to simplify the math. The average current density in the i^{th} layer is computed as,

$$J_i = \frac{k}{\pi m d_s^3 (2i-1)} \int_{(i-1)d_s}^{id_s} \frac{\mathcal{J}_0(kr)}{\mathcal{J}_1(kmd_s)} r dr \tag{3.19}$$

where $\mathcal{J}_0$ and $\mathcal{J}_1$ are the Bessel functions of the first kind, orders zero and one respectively, and the wave number, k, is defined as $\frac{1-j}{\delta}$. From this average current density, the current in each layer of the Litz wire is computed and scaled to attain the total injection current peak amplitude, I_{tot},

$$I_i = \frac{I_{tot} J_i A_i}{\beta \sum_{n=1}^{m} J_n A_n} \tag{3.20}$$

where β is the fraction of the total current carried at the bunched level. This number would be 25 for the 5x5x42/44 AWG Litz wire and 5 for the 5x40/36 AWG Litz wire. Additionally, A_i is the area of the i^{th} layer in the Litz wire cross-section. This area changes depending on the geometry of the bunched-level cross-section and must be computed individually for the triangular and rectangular sectors.

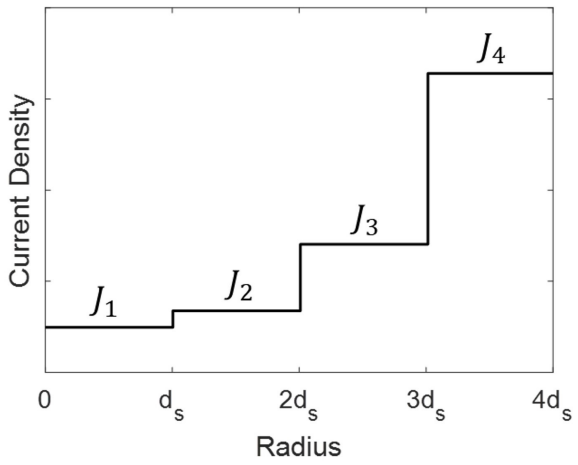

Figure 3-10: Example of the quantized current density in each layer, $m = 4$.

Loss Calculation

The current distribution has already been determined using the surrogate skin effect model. It is therefore possible to calculate skin effect loss in the conductor before

simulation. Generally, this is computed from (3.15) as follows,

$$P_{skin} = \frac{4\rho F_R}{\pi d_s^2} \sum_i^{\Omega} \frac{\pi d_{bos}^2}{4 N_s A_i} \frac{1}{2} I_i^2 \tag{3.21}$$

where Ω is the conductor cross-section domain, N_s is the total number of strands in the bundle, and d_{bos} is the conductor diameter to the outer surface of the bundle. This is essentially computing the number of strands in each layer as the product of the total number of strands in the conductor and the fraction of the cross-sectional area covered by each layer. For each layer, the number of strands and the current carried, I_i (assumed to be distributed equally amongst each strand), is enough information to compute the power loss due to skin effect for that layer. The total skin effect loss is the summation of this for each layer in the bundle.

The 5x5x42/44 AWG conductor is used here as an example to demonstrate the full skin effect power loss computation. If we define $A_{t,i}$ and $A_{r,j}$ as the area of the i^{th} layer in the triangular sector and j^{th} layer in the rectangular sector respectively, the total area of the conductor's cross section is,

$$A_\Omega = 10 \sum_{i=1}^{4} A_{t,i} + 15 \sum_{j=1}^{4} A_{r,j} = \frac{\pi d_{bos}^2}{4} \tag{3.22}$$

The total number of strands that belong to the i^{th} layer of all of the triangular sectors in the bundle is,

$$n_{t,i} = \frac{10 A_{t,i}}{A_w} N_s = \frac{40 A_{t,i}}{\pi d_{bos}^2} N_s \tag{3.23}$$

where $n_{t,i}$ is allowed to be a fraction and A_w is the total cross-sectional area of the conductor. The current per strand in that layer is,

$$i_{t,i} = \frac{10 I_{t,i}}{n_{t,i}} = \frac{10 I_{tot} J_i A_{t,i}}{25 n_{t,i} \sum_{n=1}^{4} J_n A_{t,n}} \Rightarrow \frac{\pi d_{bos}^2 I_{tot} J_i}{100 N_s \sum_{n=1}^{4} J_n A_{t,n}} \tag{3.24}$$

Similarly, the total number of strands that belong to the j^{th} layer of all of the rectangular sectors in the bundle is,

$$n_{r,j} = \frac{15 A_{r,j}}{A_w} N_s = \frac{60 A_{r,j}}{\pi d_{bos}^2} N_s \tag{3.25}$$

and the current per strand in that layer is,

$$i_{r,j} = \frac{15 I_{r,j}}{n_{r,j}} = \frac{15 I_{tot} J_j A_{r,j}}{25 n_{r,j} \sum_{n=1}^{4} J_n A_{r,n}} \Rightarrow \frac{\pi d_{bos}^2 I_{tot} J_j}{100 N_s \sum_{n=1}^{4} J_n A_{r,n}} \tag{3.26}$$

Finally, the total power loss per-unit-length due to skin effect is computed as,

$$P_{skin} = \frac{2\rho F_R}{\pi d_s^2}\left(\sum_{i=1}^{4} n_{t,i} i_{t,i}^2 + \sum_{j=1}^{4} n_{r,j} i_{r,j}^2\right) \tag{3.27}$$

The average peak magnetic field squared in the cross-section of the bundle is needed to calculate proximity loss. The purpose of using a finite-element simulation is to compute the magnetic field within the cross-section that results from the current distribution assigned in the previous section. A two-dimensional, DC simulation is setup to capture the current assignments for each layer since the frequency dependence at the bundle level has already been taken care of using the surrogate model. It is important to note that the current must be redistributed at every frequency according to the results of the surrogate model.

The spatially averaged resultant magnetic field amplitude squared is computed over the conductor cross-section from simulation results,

$$\langle H_{peak}^2 \rangle = \frac{1}{A_\Omega}\int_\Omega |H_{peak}|^2 dA \tag{3.28}$$

In the isolated conductor case, $A_\Omega = \frac{\pi d_{bos}^2}{4}$, but in a single coil it would be $A_\Omega = \frac{N_t \pi d_{bos}^2}{4}$, where N_t is the number of turns in the coil. This makes calculating proximity loss per-unit-length (which is proportional to H_{peak}^2) easier by taking the average field amplitude squared as the local transverse magnetic field applied to each strand in the conductor and plugging this into (3.17),

$$P_{prox} = N_s G_R \langle H_{peak}^2 \rangle \tag{3.29}$$

The per-unit-length AC resistance is then computed from the summation of the skin effect loss and proximity effect loss in the conductor,

$$R_{AC} = \frac{2}{I_{tot}^2}(P_{skin} + P_{prox}) \tag{3.30}$$

Fabrication Factor Extraction

There are two factors that make the surrogate skin effect model not immediately applicable to the layered mesh geometry:

1. The triangular and rectangular sectors used in the cross-section geometry does not exactly depict reality; the actual shapes are random and impossible to predict with accuracy

2. The bunching operation results in some radial transposition and current sharing between layers

To address these unknowns, an empirical fabrication factor is used. This fabrication factor is unique to each Litz conductor construction, but is independent of the

application of that Litz wire; therefore, it is a single value which can be supplied by the manufacturer as determined from a standardized isolated conductor test, for example the "zig-zag" test as discussed below. The fabrication factor is extracted from measurements obtained with an isolated conductor scenario. The measurement here is made using a "zig-zag" flat board pattern [15] in which an even number of loops are made to cancel out external fields as shown in Fig. 3-11.

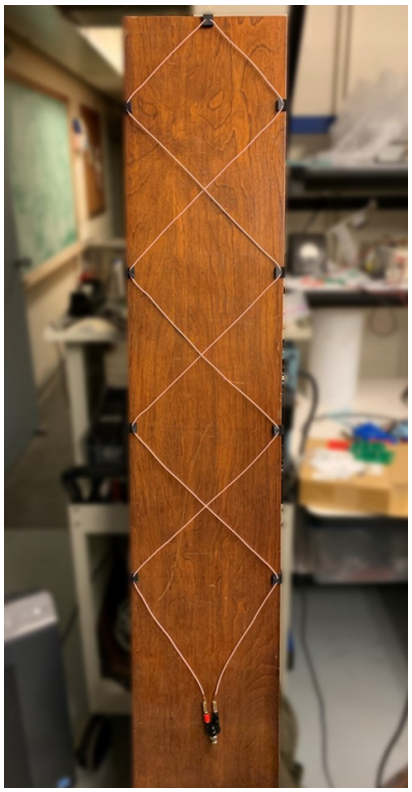

Figure 3-11: Zig-zag board pattern used for the isolated conductor measurements.

The conductor is always sufficiently far apart from itself such that the magnetic field generated by current across the board is not strong enough to induce additional proximity loss. The difference between the isolated conductor measurements and analytical theory [5] is due to non-idealities in the construction that results in unequal current distribution throughout the cross-section, which are better represented in the new calculation presented here.

The fabrication factor, F_{fab}, is a constant multiplicative factor which effectively scales the skin depth prior to running the surrogate skin effect model. Doing this scales the severity of the bundle-level skin effect. The skin-depth, δ, used in calculating the wave number for the surrogate model in (3.19) is then replaced by δ_{eff},

$$\delta = \sqrt{\frac{\rho}{\pi f \mu}} \quad \Rightarrow \quad \delta_{eff} = \sqrt{\frac{\rho}{\pi F_{fab} f \mu}} \tag{3.31}$$

where μ is the magnetic permeability of the conductor.

In order to determine the fabrication factor, the layered mesh analysis is run under the isolated conductor case with varying frequency multipliers. Once the frequency dependent resistance of the isolated layered mesh analysis matches "zig-zag" isolated measurements, the frequency multiplier is taken as the fabrication factor. This process is shown in Fig. 3-12 for both the 5x5x42/44 AWG and 5x40/36 AWG Litz wires. Note that a fabrication factor of zero is equivalent to the uniform cross-sectional current density assumption used by analytical models in the literature.

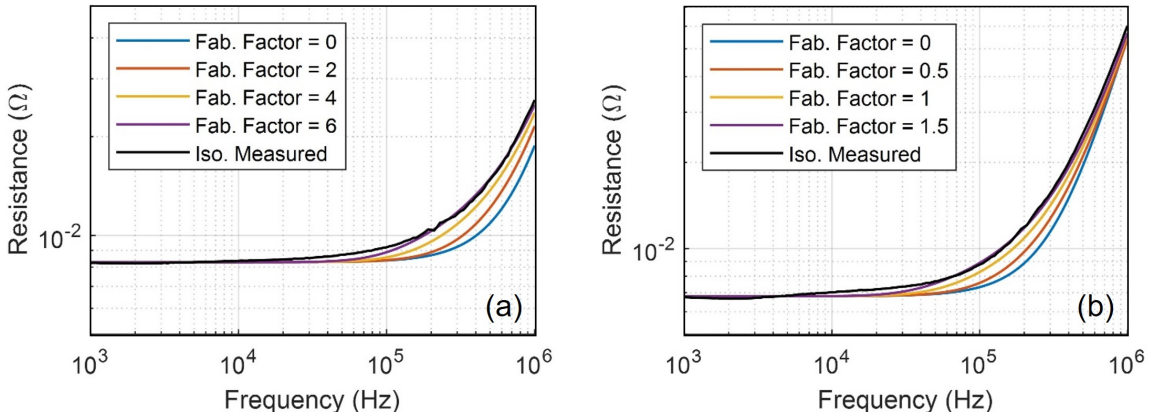

Figure 3-12: Isolated conductor layered mesh analysis with varying fabrication factors on the (a) 5x5x42/44 AWG Litz wire ($m = 4$) and (b) 5x40/36 AWG Litz wire ($m = 5$) compared to their respective isolated conductor (zig-zag) measurements.

From two plots in Fig. 3-12, a fabrication factor of 6 for the 5x5x42/44 AWG Litz wire matches the measured results very well, whereas for the 5x40/36 AWG Litz wire, a fabrication factor of 1.5 matches the measured results. These two values are used as the fabrication factor values for future analysis on each respective conductor when applied to any coil or other configuration. The current density distribution between layers in the 5x40/36 AWG Litz wire, as determined by the surrogate method, is given in Fig. 3-13 as a function of frequency and using the fabrication factor of 1.5.

Currents in each layer of the conductor cross-section are set prior to simulation as shown in Fig. 3-14 for both conductors at 4 different frequencies. The non-uniform current distribution of the layered mesh method results in more accurate internal field representation and hence improved associated loss calculations.

Arbitrary Coil Geometry

The twisting at all levels of the Litz wire construction has the effect of canceling out flux linkages induced due to transverse external magnetic fields. This means that while the external fields cannot be ignored when calculating strand-level proximity loss, they do not change the current distribution in the cross section. This is why the fabrication factor is independent of application and makes simulations of arbitrary coil geometries straight forward. The flowchart in Fig. 3-15 depicts the general layered mesh approach.

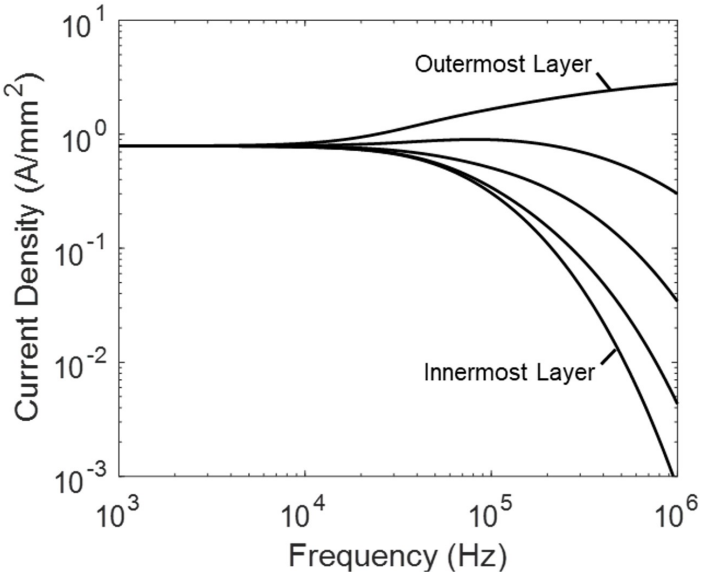

Figure 3-13: Current density in each layer of the 5x40/36 AWG Litz conductor with $F_{fab} = 1.5$ and excitation of 1 A as a function of frequency; extracted from the surrogate model.

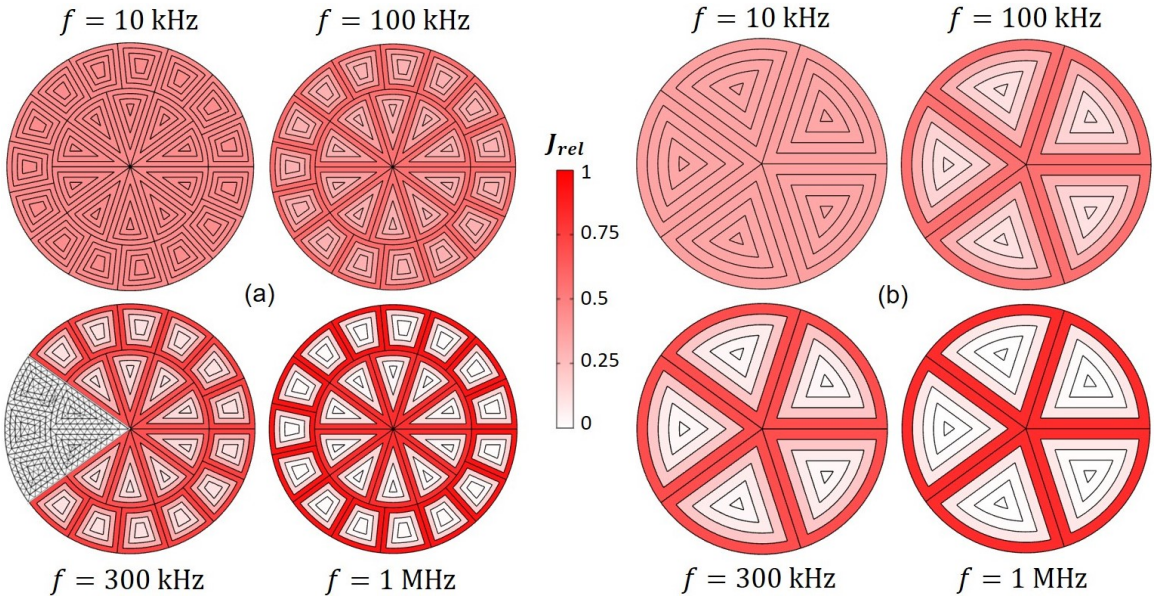

Figure 3-14: Individually normalized current density distributions in each layer at 4 different frequencies for the (a) 5x5x42/44 AWG conductor ($F_{fab} = 6$) and (b) 5x40/36 AWG conductor ($F_{fab} = 1.5$). Fine meshing was shown to be unnecessary in the DC simulations without magnetic diffusion.

In the axisymmetric solenoid simulation example, the circular cross-section of each turn is replaced with the layered mesh geometry and currents are distributed by layer according to the surrogate skin-effect model. From the DC simulation results, the

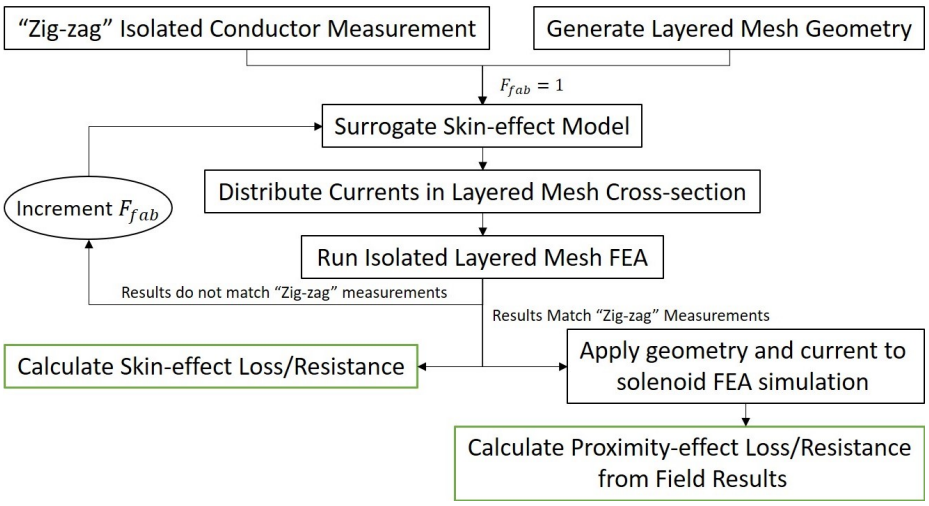

Figure 3-15: Flowchart of the general layered mesh Litz analysis.

resultant magnetic field squared is averaged over all turns in the coil and then used to compute the aggregate proximity loss per-unit length by applying this averaged field squared to each strand in the conductor. This general approach makes two assumptions: linear magnetic material properties in the domain such that no frequencies exist in the magnetic field outside of the fundamental, and single phase sources such that the magnetic field is linearly varying and sinusoidal in amplitude at every point in the domain. The layered mesh approach is applicable outside of these assumptions, however, requires a different final resistance calculation: the focus of future work.

The two Litz conductors were each wound onto respective 6 inch OD PMMA cylinders in 6 and 12 turn coil configurations using 3D printed clips to set desired turn-to-turn spacing. Fig. 3-16 shows the 5x5x42/44 AWG served conductor wound into 12 turns with c/a spacing factors of 1.5 and 2.5 respectively. Note that the spacing factor is the coil pitch, λ, normalized by the conductor OD, $c/a = \lambda/d_{bos}$.

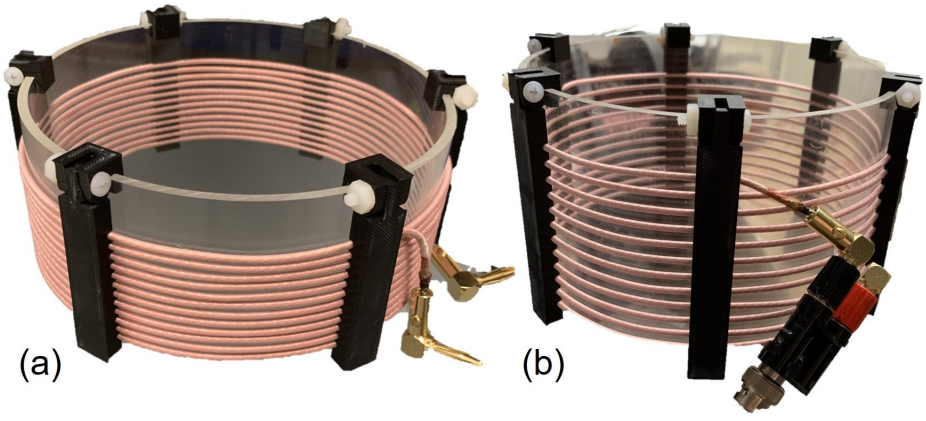

Figure 3-16: 12 turn 5x5x42/44 AWG Litz coils with (a) $c/a = 1.5$ (b) $c/a = 2.5$.

Measurements were taken via an Omicron Bode 100 VNA with the one-port

method (see Appendix for more details). These measured results are compared to the layered mesh simulation in Fig. 3-17. In order to accurately assess the performance of the simulation method, the measurements were linearly scaled to match the simulated resistance value at 10 kHz. This absolute deviation from theory in measured DC resistance (up to 15%) can be attributed to several different factors, including lead connections, imperfect termination (soldered), and limited ability of the measurement method at low impedances. The linear scaling correction was proven to be the proper compensation approach by applying the same scaling to measurements of solid conductor coils and comparing to FEA simulated results (see Appendix B). All FEA simulations were carried out in COMSOL's AC/DC module.

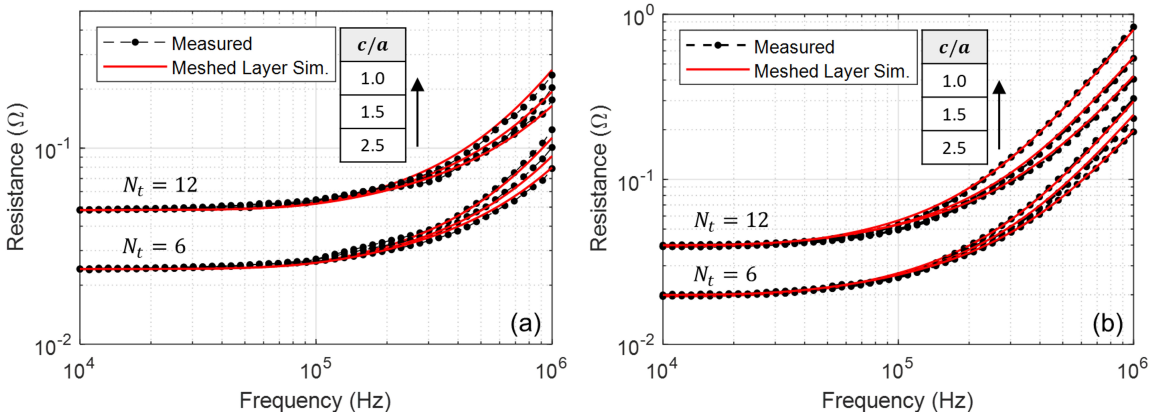

Figure 3-17: Simulation and measurement results for several coil configuration using the (a) 5x5x42/44 AWG Litz wire and (b) 5 AWG Litz wire and (b) 5x40/36 AWG Litz wire.

3.5 Multi-phase Loss Implications

This section presents a method to approximate the AC power loss in Litz wire systems with arbitrary field sources, accounting for local elliptically rotational fields. The general approach is demonstrated with a simplified FEA formulation and shows good alignment with explicit strand-level simulations. Focus of the analysis is placed on multi-coil, air-core applications such as resonant power transfer systems; a fast semi-analytical approach using averaging points is provided for these problems to reduce run times by several orders of magnitude.

Many analytic models prevalent in the literature [3, 5, 6, 9], formulate the solenoid or transformer problem using a general window method in which several simplifying approximations are made to estimate the leakage field. Only single-phase currents which produce stationary AC magnetic fields everywhere in the domain are considered in these calculations and therefore the models are not applicable to general applications of Litz wire, such as those used in multi-coil resonant power transfer systems. In these systems, multiple resonant tanks generate out-of-phase field sources. Not only

is it common for these applications to be fully air-cored [61], with complicated leakage field distributions, but multi-phase currents create a resultant magnetic field at any point in the domain whose vector rotates and is generally elliptical in magnitude variation. In a generic two-hoop setup shown in Fig. 3-18 with each coil individually excited, Fig. 3-19 shows this phenomenon for a random point, P, in the cross-section of the domain with varying current phases.

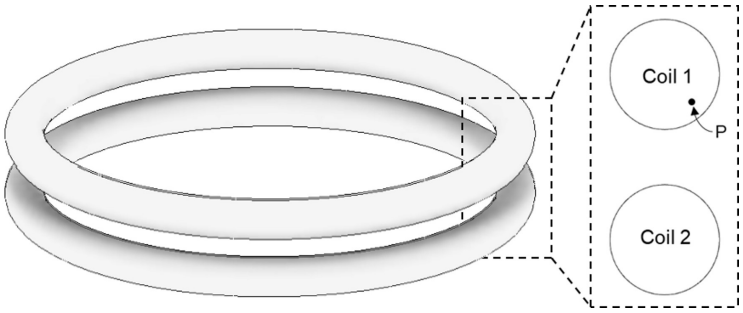

Figure 3-18: A generic two-hoop setup with each coil individually excited. Fields are observed at a representative point, P, in the xy-plane cross-section.

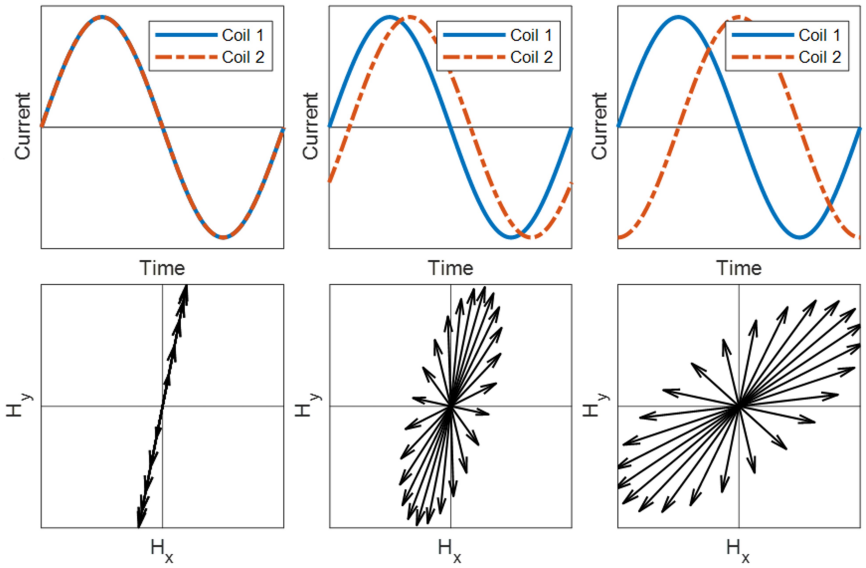

Figure 3-19: Vector plot of the elliptically rotational magnetic fields experienced by the point, P, in the domain of a multi-phase system.

3.5.1 Elliptically Rotational Magnetic Fields

In a multi-phase system, the strand-level skin-effect remains the same as described in Section 3.3.1. However, the proximity-effect effect, which was previously assumed in Section 3.3.2 to be transverse, stationary, and varying only in magnitude, now becomes non-trivial.

Fig. 3-20 shows the eddy current distribution in the cross section of a cylindrical conductor with a uniformly rotating external magnetic field applied at varying frequencies. It has been postulated in [47] and proven in Section 3.5.4 that the major and minor amplitudes of a rotational field may be taken as orthogonal in the calculation of proximity loss. That is, loss due to the major and minor components of the resultant field may be individually computed using the calculation in (3.17) and then summed up to compute the total proximity loss.

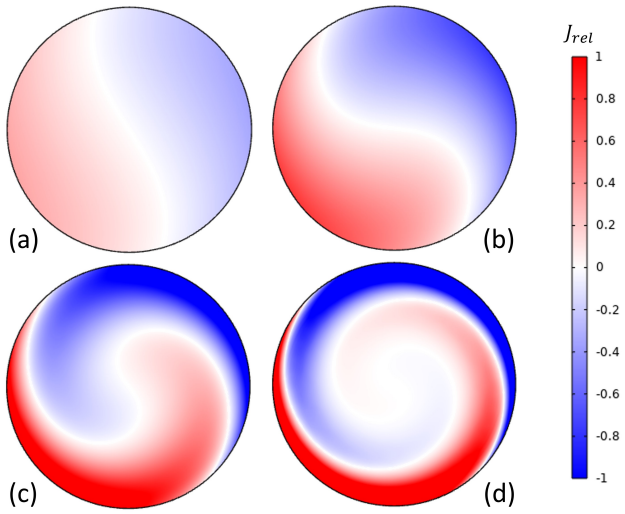

Figure 3-20: Real component of the steady-state eddy current density in a 1 mm copper strand due to uniform transverse rotational fields (circularly oriented) of equal magnitude at (a) 100 Hz, (b) 10 kHz, (c) 100 kHz, and (d) 1 MHz

.

When multiple field sources are present, the contribution at any point in the domain from each source at a given frequency may be represented using phased vectors as shown in Fig. 3-21 for an example with $N = 4$ sources.

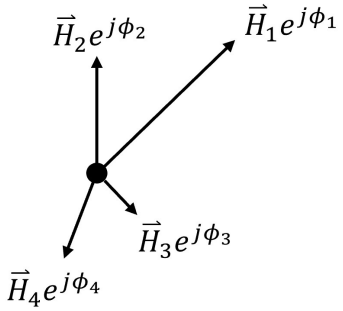

Figure 3-21: Magnetic field vector contributions from each coil at any point in the domain with $N = 4$ sources.

$$\mathbf{H_{tot}}(t) = \hat{x}\sum_{i=1}^{N} H_{x,i}\cos(2\pi ft + \phi_i) + \hat{y}\sum_{i=1}^{N} H_{y,i}\cos(2\pi ft + \phi_i) \tag{3.32}$$

$$\mathbf{H_{tot}} = \hat{x}|H_x|e^{j\theta_x} + \hat{y}|H_y|e^{j\theta_y} \tag{3.33}$$

The resultant magnetic field amplitude variation in time (3.32) can be written as the summation of the individual contributions and is generally elliptically rotational. Here four quantities are introduced to facilitate conversion from temporal form in (3.32) to complex phasor representation (3.33),

$$H_{Rx} = \sum_{i=1}^{N} H_{x,i}\cos(\phi_i) \tag{3.34}$$

$$H_{Ix} = \sum_{i=1}^{N} H_{x,i}\sin(\phi_i) \tag{3.35}$$

$$H_{Ry} = \sum_{i=1}^{N} H_{y,i}\cos(\phi_i) \tag{3.36}$$

$$H_{Iy} = \sum_{i=1}^{N} H_{y,i}\sin(\phi_i) \tag{3.37}$$

With these quantities, the aggregate orthogonal phases, θ_x and θ_y, have the relationships,

$$\theta_x = \tan^{-1}\left(\frac{H_{Ix}}{H_{Rx}}\right) \tag{3.38}$$

$$\theta_y = \tan^{-1}\left(\frac{H_{Iy}}{H_{Ry}}\right) \tag{3.39}$$

and aggregate orthogonal magnitudes, $|H_x|$ and $|H_y|$, are,

$$|H_x| = \sqrt{H_{Rx}^2 + H_{Ix}^2} \tag{3.40}$$

$$|H_y| = \sqrt{H_{Ry}^2 + H_{Iy}^2} \tag{3.41}$$

Finally, after converting to phasor representation (3.33), the major and minor amplitudes of the resultant field can be calculated from [62],

$$H_{\substack{major\\minor}} = |H_x|\cos(\alpha) \pm |H_y|\sin(\alpha) \tag{3.42}$$

where the angle, α, from the global x-axis to either the major or minor axis is written as,

$$\alpha = \frac{1}{2}\tan^{-1}\left(\frac{2|H_x||H_y|\cos(\theta_y - \theta_x)}{|H_x|^2 + |H_y|^2}\right) \tag{3.43}$$

3.5.2 Simplied FEA Approach and Post-processing Calculations

A general FEA approach is laid out in which each phased coil is excited separately with DC current, and the resulting DC field distributions in the entire domain from the individual excitations are recorded for post-processing.

$$\begin{aligned} H_{eff}^2 &= H_{major}^2 + H_{minor}^2 \\ &= 2|H_x|^2 \cos^2(\alpha) + 2|H_y|^2 \sin^2(\alpha) \end{aligned} \tag{3.44}$$

Because of quasi-static conditions, the DC field values are used with the calculations provided above to determine the spatially averaged effective field amplitude (3.44), H_{eff}, over the 2D cross section of the Litz bundles and to compute the power loss for each coil given the currents and number of strands.

The choice of DC excitation both simplifies and expedites the simulation and is a good approximation under the ideal assumption that every strand in the Litz bundle carries equal total current [48].

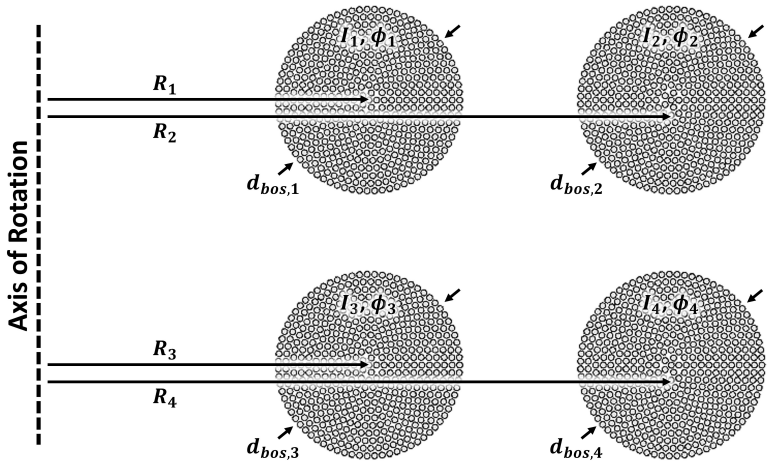

Figure 3-22: Simulation setup for an explicit strand-level simulation. Four single-turn coils, each composed of 484 strands.

This simulation approach, referred to here as the "Elliptical FEA Method," is implemented using COMSOL's AC/DC module where (3.32)-(3.44) are compiled into a surface averaging post-process on the simulation results. The computed losses are compared to a brute-force simulation in which four single-turn coils with currents of varying phase are modeled at the strand-level as shown in Fig. 3-22. All 484 strands in each coil are explicitly modeled and excited with equal current according to the assumption made in Section 3.5.2. This simulation approach is generally impractical as the fine mesh required to accurately capture the current density distribution in each strand, and thus accurately compute loss, renders the simulation time and resources beyond the capabilities of many computers. Nevertheless, the strand-level simulation is taken as the "true" solution to gauge fidelity of the proposed method.

The "Elliptical FEA Method," which took just 9 seconds to simulate, demonstrates great alignment with the brute-force simulation for two different strand gauges, as shown in Fig. 3-23. The large brute-force simulation in comparison took more than a day to simulate just a four-turn problem with the same computational resources. The large reduction in simulation time is not just due to a simpler geometry, but also because the entire frequency dependence of the loss is captured in (3.14) and (3.16) outside of the simulation such that the "Elliptical FEA Method" need only run one DC simulation to capture the H_{eff} used in (3.17).

The use of FEA for field calculations makes this approach general enough to consider problems with magnetic material in the domain if operated in the linear region of its B-H curve. Non-linear materials require extra attention.

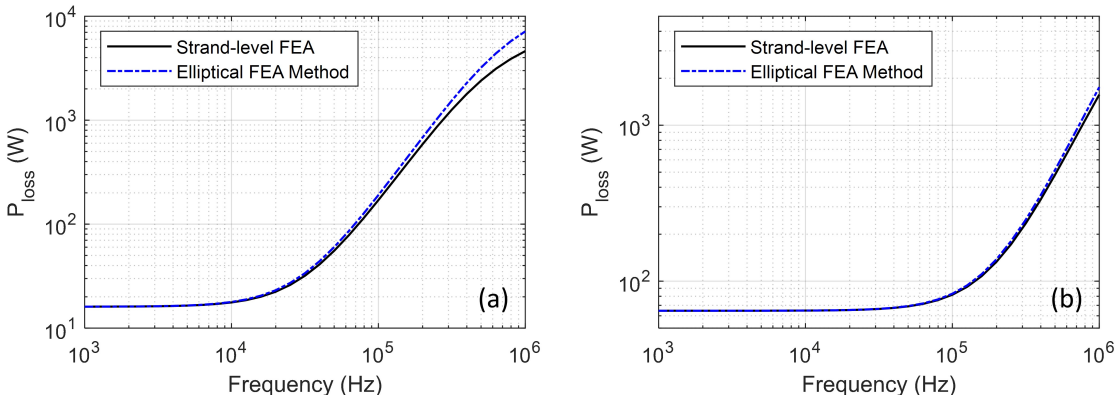

Figure 3-23: Comparison of the proposed loss calculation method implemented in FEA and a strand-level simulation of a four single-turn coil system using bundles of (a) 30 AWG strands and (b) 36 AWG strands.

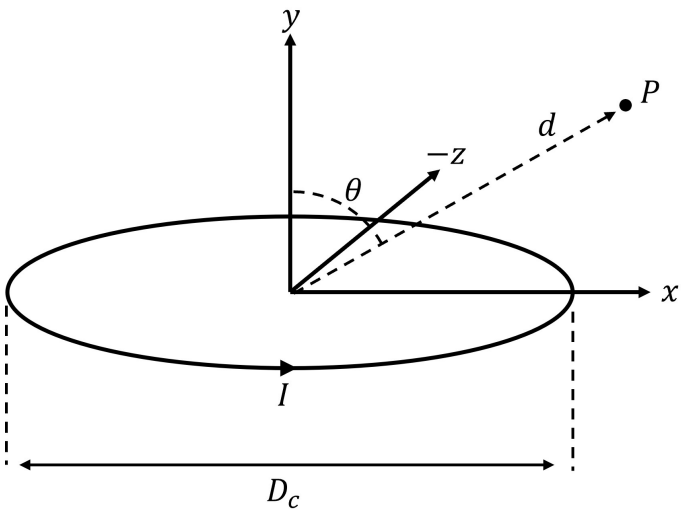

Figure 3-24: Geometry setup for "Loop Center" analytical calculation of the magnetic field external to a turn of interest.

3.5.3 Semi-Analytical Approach for Multi-coil Air-core Systems

A semi-analytical approach can be applied to the subset of problems known as "air-core", in which no magnetic materials are present, much like in many resonant power transfer topologies. Analytical expressions are known for the field distribution due to a circular current loop as shown in Fig. 3-24 [63],

$$\Delta^2 = \left(\frac{D_c}{2}\right)^2 + d^2 + D_c d\sin(\theta) \tag{3.45}$$

$$\beta^2 = \left(\frac{D_c}{2}\right)^2 + d^2 - D_c d\sin(\theta) \tag{3.46}$$

$$H_r = \frac{I D_c^2 E(k^2)}{4\pi\beta^2\Delta}\cos(\theta) \tag{3.47}$$

$$H_\theta = \frac{I\left[\left(d^2 + \left(\frac{D_c}{2}\right)^2\cos(2\theta)\right)E(k^2) - \beta^2 K(k^2)\right]}{2\pi\beta^2\Delta\sin(\theta)} \tag{3.48}$$

where H_r, H_θ, K, and E are the radial and azimuthal magnetic field components at point P in the xy-plane, and elliptical integrals of the first kind and second kind, respectively and,

$$k = \sqrt{\frac{2D_c d\sin(\theta)}{\Delta^2}} \tag{3.49}$$

The x and y magnetic field components can be then directly computed from the radial and azimuthal components,

$$H_x = H_r\sin(\theta) + H_\theta\cos(\theta) \tag{3.50}$$

$$H_y = H_r\cos(\theta) - H_\theta\sin(\theta) \tag{3.51}$$

For circularly wound coils, each turn is taken as an independent current loop and the field contributions are summed up as described in (3.32). To avoid computationally expensive integration, equally spaced points are generated in the cross-section of the bundles where the fields are calculated and averaged over all points to compute loss in the coil. The proximity field in a turn to due to current in another turn is calculated using the "Loop Center" method described above. However, for internal proximity fields generated by a turn's own current, an infinitely long, straight conductor approximation is used,

$$R = \sqrt{\left(\hat{x} - \frac{D_c}{2}\right)^2 + (\hat{y} - y)^2} \tag{3.52}$$

$$\zeta = \tan^{-1}\left(\frac{\hat{y} - y}{\hat{x} - \frac{D_c}{2}}\right) \tag{3.53}$$

$$H_x = -\sin(\zeta)\frac{2IR}{\pi d_{bos}^2} \tag{3.54}$$

$$H_y = \cos(\zeta)\frac{2IR}{\pi d_{bos}^2} \tag{3.55}$$

where $(\hat{x}, \hat{y})$ is the location of an averaging point, R and ζ are its distance from and angle about the bundle center, y is the axial position of the turn center, d_{bos} is the bundle outer surface diameter, and I is the total peak current in the turn.

Algorithm 1 Semi-Analytical Multi-phase Loss Calculation

function GETLOSS(d_{bos}, D_c, y, d_s, N_s, I, ϕ, f)
- Each input vector $\in \mathbb{R}^n$ where n is the total # of turns
- Input vectors are denoted collectively as $(\cdot)$

for turn i in n **do** ▷ turn to calculate field at
$[\hat{x}, \hat{y}] \leftarrow$ `GetAveragingPoints`$((\cdot)[i])$
for turn j in n **do** ▷ iterate through source turns
if $i == j$ **then**
$[\hat{H}_x, \hat{H}_y] \leftarrow$ `Straight`$(\hat{x}, \hat{y}, (\cdot)[i])$
else
$[\hat{H}_x, \hat{H}_y] \leftarrow$ `LoopCenter`$(\hat{x}, \hat{y}, (\cdot)[j])$
$[H_{Rx}, H_{Ix}, H_{Ry}, H_{Iy}] \mathrel{+}= \{\hat{H}_x, \hat{H}_y\}_{\phi[j]}$
$H_{eff}^2[i] \leftarrow \langle$`Transform`$([H_{Rx}, H_{Ix}, H_{Ry}, H_{Iy}])\rangle$
$[F_R, G_R] \leftarrow$ `CalcF`$_{\mathtt{R}}$`G`$_{\mathtt{R}}$$(d_s, f)$
$P_{skin} \leftarrow \sum \frac{8\rho F_R D_c N_s^3}{(d_s I)^2}$
$P_{prox} \leftarrow \sum \pi D_c N_s G_R H_{eff}^2$
return $P_{loss} = P_{skin} + P_{prox}$

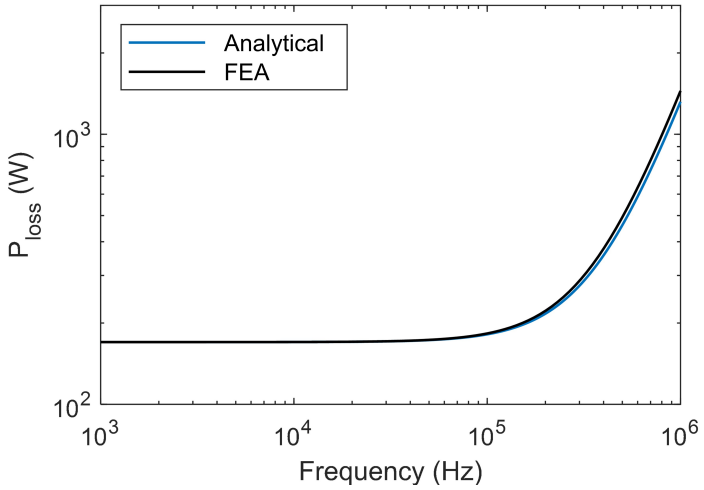

Figure 3-25: Comparison of the analytical calculation implemented in MATLAB and a strand-level FEA simulation in COMSOL for an example perfect Litz multi-coil system using 36 AWG strands

The semi-analytical approach is implemented in MATLAB through Algorithm 1 and shows good alignment with the full FEA simulations discussed in Section 3.5.2 as shown in Fig. 3-25. To compute the same problem with the semi-analytical approach using averaging points took just 23 ms to run; a 400x reduction over the "Elliptical FEA Method."

3.5.4 Proof of Spatially Orthogonal Proximity Effect

To prove that spatially orthogonal components of an incident rotating field described in general phasor notation by,

$$\mathbf{B_i} = \hat{x}B_x + \hat{y}jB_y \tag{3.56}$$

can be used to compute loss corresponding to each component individually before summing up to get the total loss, we follow a process similar to that described in [54]. Nagel derives the field in the domain of an infinitely long conducting cylinder of radius a due to an incident transverse harmonic field. The geometry of this problem lends itself to a cylindrical coordinate system, (ρ, ϕ, z), such that (3.56) becomes,

$$\begin{aligned}\mathbf{B_i} =&\hat{\rho}\big(B_x\cos(\phi) - jB_y\sin(\phi)\big)\\ &+\hat{\phi}\big(-B_x\sin(\phi) + jB_y\cos(\phi)\big)\end{aligned} \tag{3.57}$$

Absent a conducting cylinder, the magnetic vector potential which generates (3.57) according to $\mathbf{B_i} = \nabla \times \mathbf{A_i}$ can be simply written as,

$$\mathbf{A_i} = \hat{z}\big(B_x\rho\sin(\phi) - jB_y\rho\cos(\phi)\big) = \hat{z}A_{i,z} \tag{3.58}$$

However, with a conducting cylinder in the domain, the vector field is non-trivial and follows the scalar Helmholtz equation,

$$\rho^2\frac{\partial^2 A_z}{\partial\rho^2} + \rho\frac{\partial A_z}{\partial\rho} + k^2\rho^2 A_z + \frac{\partial^2 A_z}{\partial\phi^2} = 0 \tag{3.59}$$

where $k = \frac{1-j}{\delta}$ is the wavenumber. It is well known [64] that, through separation of variables, the solution to (3.59) is of the form,

$$A_z = D_1\mathcal{J}_\nu(k\rho)\big[C_1\cos(\nu\phi) + C_2\sin(\nu\phi)\big] \tag{3.60}$$

when $\rho \leq a$ for finite vector potential at $\rho = 0$, where $\mathcal{J}_\nu$ is the ν^{th} order Bessel function of the first kind. The vector potential outside the conducting cylinder ($\rho > a$) is of the form,

$$A_z = \big(D_2\rho^\nu + D_3\rho^{-\nu}\big)\big[C_1\cos(\nu\phi) + C_2\sin(\nu\phi)\big] \tag{3.61}$$

To solve for the unknowns, the following three boundary conditions are formulated to assert the incident field and satisfy Maxwell's equations:

BC1) $\lim_{\rho\to\infty} \mathbf{A} = \mathbf{A_i}$

BC2) $A_z(a^-, \phi) = A_z(a^+, \phi)$

BC3) $\hat{\rho} \times \nabla \times \mathbf{A}|_{\rho=a^-} = \hat{\rho} \times \nabla \times \mathbf{A}|_{\rho=a^+}$

The first boundary condition, BC1), enforces the source vector potential to be $\mathbf{A_i}$ at $\rho \to \infty$ and leads to the following relationships,

$$\nu = 1 \tag{3.62}$$

$$D_2 C_1 = -jB_y \tag{3.63}$$

$$D_2 C_2 = B_x \tag{3.64}$$

With this knowledge, BC2), which requires continuity of $\mathbf{A}$ at the boundary of the conducting cylinder and air, leads to the relationship,

$$D_1 a \mathcal{J}_1(ka) = D_2 a^2 + D_3 \tag{3.65}$$

The final boundary condition stems from Maxwell's equations and the continuity of the tangential magnetic field at the surface described by $\rho = a$ for non-magnetic materials. Writing BC3) out leads to,

$$ka^2 D_1 \frac{1}{2}\big[\mathcal{J}_0(ka) - \mathcal{J}_2(ka)\big] + D_3 = D_2 a^2 \tag{3.66}$$

Noticing that for the region of interest (inside the conducting cylinder, $\rho \leq a$), if we substitute C_1 and C_2 in terms of D_2 into (3.60), the vector potential can be written in terms of the ratio of only two unknowns, D_1 and D_2,

$$\mathbf{A}(\rho \leq a) = \hat{z}\frac{D_1}{D_2}\mathcal{J}_1(k\rho)\big[B_x \sin(\phi) - jB_y \cos(\phi)\big] \tag{3.67}$$

Combining (3.65) and (3.66) to eliminate D_3 results in the ratio,

$$\frac{D_1}{D_2} = \frac{4a}{ka\big[\mathcal{J}_0(ka) - \mathcal{J}_2(ka)\big] + 2\mathcal{J}_1(ka)} \tag{3.68}$$

which, when substituted into (3.67), gives the final vector potential inside the conducting cylinder. However, the current density distribution in the conducting cylinder is the desired result. Fortunately, the current density in a divergence-less magnetic vector potential follows the simple relationship, $\mathbf{J} = -j\omega\sigma\mathbf{A}$, and allows us to write the complex current density everywhere in the cylinder,

$$\mathbf{J} = \hat{z}\frac{-j4\omega\sigma a}{ka\big[\mathcal{J}_0(ka) - \mathcal{J}_2(ka)\big] + 2\mathcal{J}_1(ka)}\mathcal{J}_1(k\rho) \big[B_x \sin(\phi) - jB_y \cos(\phi)\big] \tag{3.69}$$

Finally, to prove that spatially orthogonal field components are also orthogonal

in the computation of proximity-effect power loss, the following condition must hold true,

$$\iint |\mathbf{J}|^2 = \iint |\mathbf{J}|^2_{B_x=0} + \iint |\mathbf{J}|^2_{B_y=0} \tag{3.70}$$

which in this case is trivial because,

$$|\mathbf{J}|^2 = |\mathbf{J}|^2_{B_x=0} + |\mathbf{J}|^2_{B_y=0} \tag{3.71}$$

Chapter 4

Coreless Transformer Design

This chapter covers the application of the tools described in the preceding text to the design of an ultra-high efficiency four-coil resonant air-core transformer. The approach is to take the high-level design of an existing solid conductor transformer (MIT's 40 kW transformer) and optimize the conductors for minimal complexity and maximum efficiency, two objectives that generally work against each other. The analytical multi-phase Litz wire approach described in Section 3.5 is used to optimize the Litz conductors because of its fast computation enabling a large and thorough design space exploration.

4.1 Cylindrical Transformer Parameter Extraction

In order to establish current magnitudes and phases during transformer operation, the inductance matrix of the transformer must be know. The general geometric definitions of a coaxial multi-coil system with cylindrical coils is shown in Fig. 4-1.

When calculating the diagonal entries of the inductance matrix, the self inductance of each coil is [65],

$$L = \sum_{i=1}^{N_t} \sum_{j=1}^{N_t} L_{ij} \tag{4.1}$$

where if $i = j$, then [66],

$$L_i = \mu_0 R_i \left\{ \left(1 + \frac{d_{bos}^2}{32 R_i^2} \right) \log \left(\frac{16 R_i}{d_{bos}} \right) + \frac{d_{bos}^2}{96 R_i^2} - 1.75 \right\} \tag{4.2}$$

and if $i \neq j$, then [67],

$$L_{ij} = \mu_0 \sqrt{R_i R_j} \left\{ \left(\frac{2}{k} - k \right) K(k) - \frac{2}{k} E(k) \right\} \tag{4.3}$$

where K and E are the complete elliptic integrals of the first and second kind respec-

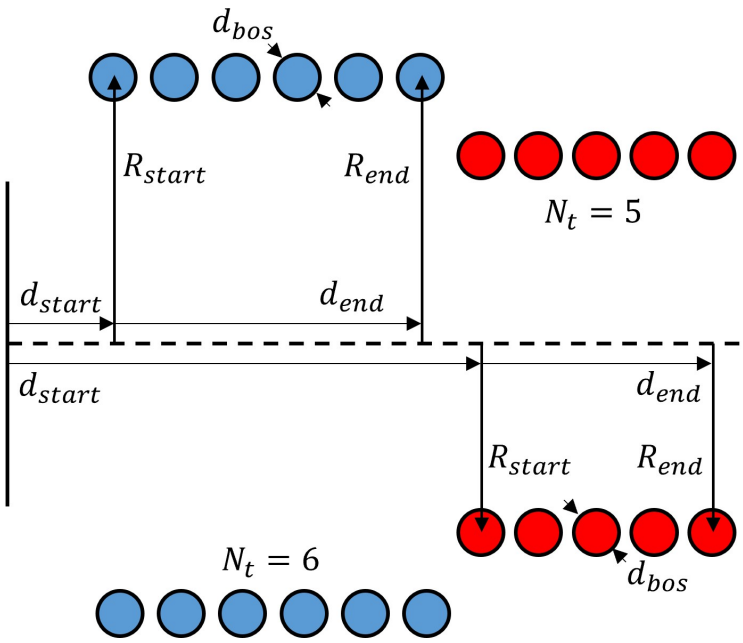

Figure 4-1: Geometry setup used when calculating the inductance matrix of a coaxial multi-coil system with cylindrically-wound coils.

tively and,

$$k = \frac{2\sqrt{R_i R_j}}{\sqrt{(R_i + R_j)^2 + (d_i - d_j)^2}} \tag{4.4}$$

When computing the non-diagonal entries of the inductance matrix, the mutual inductance between two coils is calculated by summing the contributions of individual hoops in each coil,

$$M_{mn} = \sum_{i=1}^{N_{t,m}} \sum_{j=1}^{N_{t,n}} L_{ij} \tag{4.5}$$

where (4.3) is used to compute each L_{ij}.

Fig. 4-2 shows the equivalent circuit of the four coil resonant transformer without resistive elements. The losses will be computed through the analysis techniques described in Chapter 3, so this circuit will only be used to extract current magnitudes and phases in each coil.

Once the inductance matrix is known, the currents can be solved for in the frequency domain with known resonant capacitors C_1 and C_2, source voltage magnitude (V_s), source resistance (R_s), and load resistance (R_L). With a four-port circuit matrix formulation, $\mathbf{V} = \mathbf{ZI}$,

$$\begin{bmatrix} V_s \\ 0 \\ 0 \\ 0 \end{bmatrix} = \begin{bmatrix} R_s + j\omega L_1 & j\omega M_{12} & j\omega M_{13} & j\omega M_{14} \\ j\omega M_{12} & j\omega L_2 + \frac{1}{j\omega C_2} & j\omega M_{23} & j\omega M_{24} \\ j\omega M_{13} & j\omega M_{23} & j\omega L_3 + \frac{1}{j\omega C_3} & j\omega M_{34} \\ j\omega M_{14} & j\omega M_{24} & j\omega M_{34} & R_L + j\omega L_4 \end{bmatrix} \begin{bmatrix} I_1 \\ I_2 \\ I_3 \\ I_4 \end{bmatrix} \tag{4.6}$$

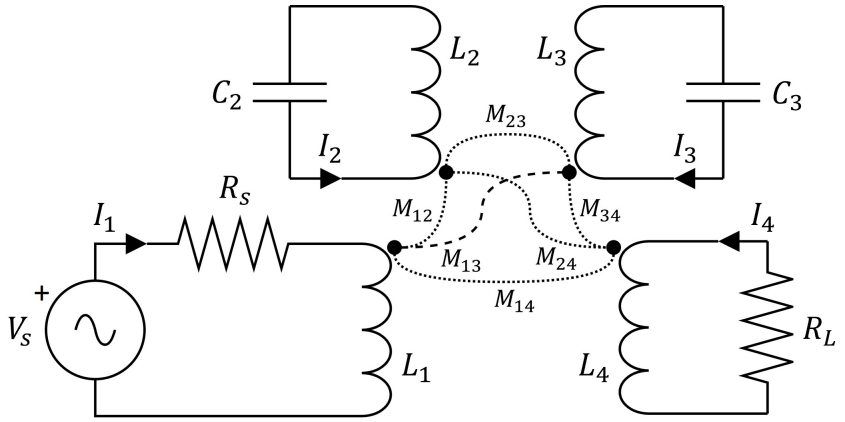

Figure 4-2: Equivalent circuit of the four coil resonant transformer.

The currents are then solved for by $\mathbf{I} = \mathbf{Z}^{-1}\mathbf{V}$. These are inputs to the analytical multi-phase Litz loss calculation.

4.2 Genetic Algorithm Setup

A genetic algorithm based optimization package for MATLAB, GOSET [68], is used here to optimize the transformer with two objective functions:

$$\text{Objective 1} : \min\left\{N_{s,tot}\right\} \tag{4.7}$$

$$\text{Objective 2} : \max\left\{\eta\right\} \tag{4.8}$$

where $N_{s,tot}$ is the total number of strands in all of the coils and η is the transformer efficiency at a specified frequency and output power.

With the center location of each turn in the transformer fixed, the current magnitudes and phases are fixed and the optimization only varies two parameters per coil, a scaling factor and the strand gauge, for a total of 8 decision variables. The scaling factor linearly scales the bundle OD from the baseline value of the equivalent solid conductor transformer, d_{bos}. Based on this new diameter, the strand gauge, and a fixed fill factor (50%) the number of strands in each bundle can be calculated.

$$N_{s,i} = \left\lfloor \frac{\mathrm{FF}_i\ \mathrm{SF}_i\ d_{bos,i}^2}{\left[(0.127\times 10^{-3})92^{\frac{36-\mathrm{AWG}_i}{39}}\right]^2} \right\rfloor \tag{4.9}$$

where FF_i, SF_i, and AWG_i are the fill factor, scaling factor, and strand gauge used in the i^{th} coil, respectively. Table 4.1 gives the optimization variables, their ranges, and types.

The algorithm randomly selects values for each parameter, called genes, with the design combination of genes referred to as an individual. A population of individuals is mutated to create the next generation based on the performance of each individual, quantified by the fitness functions. This continues for several generations until even-

Table 4.1: Transformer Optimization Variables

Tag	Optimization Parameter	Min. Values	Max. Value	Type
g_1	Coil 1: d_{bos} Scaling Factor	0.1	c/a_1	Linear
g_2	Coil 2: d_{bos} Scaling Factor	0.1	c/a_2	Linear
g_3	Coil 3: d_{bos} Scaling Factor	0.1	c/a_3	Linear
g_4	Coil 4: d_{bos} Scaling Factor	0.1	c/a_4	Linear
g_5	Coil 1: Strand Gauge	38	52	Integer
g_6	Coil 2: Strand Gauge	38	52	Integer
g_7	Coil 3: Strand Gauge	38	52	Integer
g_8	Coil 4: Strand Gauge	38	52	Integer

tually the designs converge. For a multi-objective optimization, the designs typically converge to what is called a Pareto optimal front: the optimal front delineating the trade-off between objectives (an example is shown in Fig. 4-3). Any design along this front is optimal and it becomes a designer's decision which point to choose based on how they weight each objective in terms of importance.

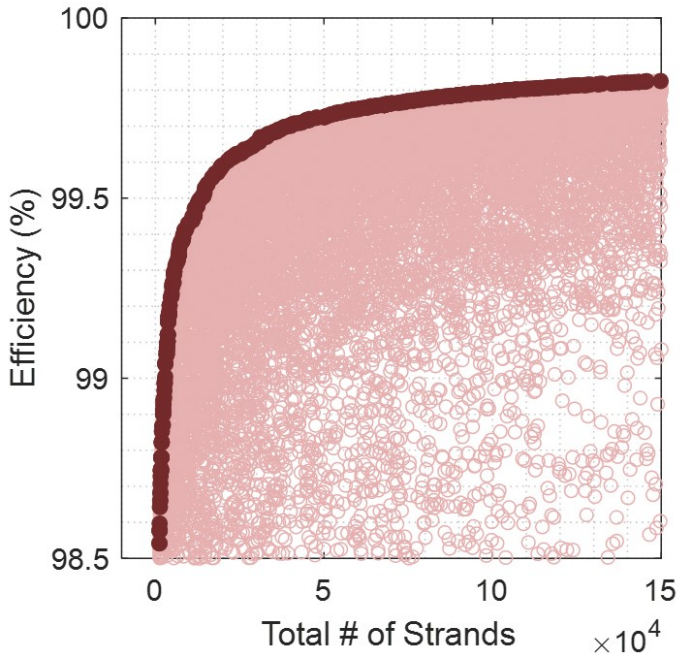

Figure 4-3: All points evaluated in an example genetic algorithm optimization with the Pareto front highlighted.

4.3 Optimization Results

The 4x voltage ratio 40 kW transformer was optimized at several frequencies around the designed frequency and each optimization consisted of 125 generations with a population of 300 individuals in each generation except for the initial population of 1,000. All designs which failed geometry checks were "killed" by artificially modifying the fitness evaluation of those designs, similar to the Augmented Lagrangian Method for unconstrained optimization problems [69]. Fig. 4-4(a) shows the optimal fronts for each frequency studied and Fig. 4-4(b) shows a different visualization of the same data which can be used to easily identify the minimum total number of strands in the optimal design for a target efficiency at a specified frequency. The minimum number of strands is a good indication of the minimum level of complexity required for the Litz wire to achieve the target efficiency.

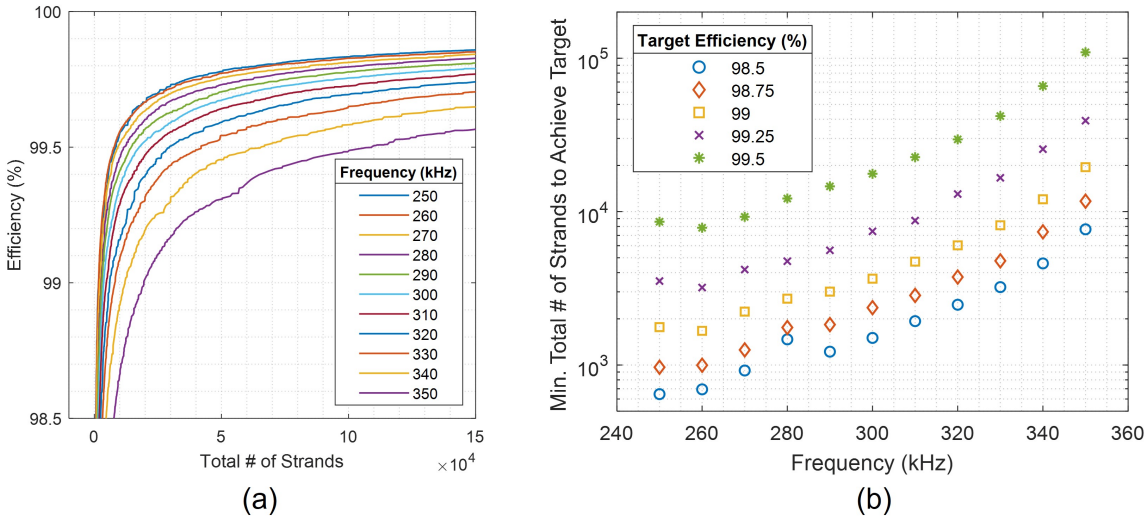

Figure 4-4: (a) Optimal fronts extracted from the optimization of the 40 kW transformer with a 4x voltage ratio at several frequencies of interest (b) a different visualization of the results according to target efficiencies.

While several frequencies were analyzed to observe trade-offs in frequency, the transformer has peak magnetic performance at 290 kHz and therefore we can select a design from the 290 kHz optimal curve. However, it should be noted that not all designs produced by the optimization are feasible. This is for several reasons. First of all, Litz wire composed of odd numbered strand gauges in the AWG standard are typically not available. Additionally, the construction of the conductor is up to the manufacturer and certain strand counts are structurally unstable [70]. And finally, the fill factor is highly dependent on conductor construction and therefore the 50% fill factor assumed, which correlates the number of strands to the bundle diameter for a given strand gauge, will not hold true in reality.

For these reasons, the optimal designs are used as general guidance to select commercially available Litz wire from New England Wire's product selection guide

[37]. Table 4.2 shows optimal designs selected for target efficiencies of 99% and 99.5%, and their corresponding similar feasible design according to conductors listed in New England Wire's catalog. The feasible designs were run through the same analysis, this time with set strand numbers and bundle diameters, to compute the transformer efficiency. In some cases, these feasible conductors actually perform better due to the aforementioned difference in fill factor.

Table 4.2: Optimal Designs Selected

Parameter	Opt. Design	Feas. Design	Opt. Design	Feas. Design
$d_{bos,1}$ [in]	0.1296	0.157	0.1905	0.226
$d_{bos,2}$ [in]	0.1392	0.157	0.1946	0.226
$d_{bos,3}$ [in]	0.1518	0.157	0.1949	0.226
$d_{bos,4}$ [in]	0.0853	0.093	0.1829	0.231
Gauge 1 [AWG]	40	40	44	44
Gauge 2 [AWG]	39	40	44	44
Gauge 3 [AWG]	40	40	44	44
Gauge 4 [AWG]	38	38	42	42
# of strands in Coil 1	849	1,100	4,641	4,200
# of strands in Coil 2	777	1,100	4,840	4,200
# of strands in Coil 3	1,164	1,100	4,858	4,200
# of strands in Coil 4	231	260	2,688	2,700
Total # of strands	3,021	3,560	17,027	15,300
Efficiency @ 290 kHz	99.00%	99.12%	99.50%	99.52%

4.4 Optimal Design Construction

A theoretical efficiency of 99.5% was chosen as desirable, accounting for expected performance degradation due to construction non-idealities. The design in the last column of Table 4.2 was selected with a small modification. Coils 1-3 could be constructed by twisting together 4 bundles of the 5x5x42/44 AWG Litz conductor readily available from previous studies in Section 3.4. Coil 4 in the design was modified to be three of these conductors twisted together for a total strand count of 3,150 and approximate bundle diameter of 0.2 in.

Twisting together several pre-formed bundles with tight enough pitch to remain structurally sound is non-trivial due to significant torque build up in both the tensioned strands and the Nomex insulating fiber. To deal with this during construction, a funnel fixture shown in Fig. 4-5 was constructed. The funnel creates enough friction to prevent the conductors from slipping through and the shaped outlet sustains the torque at one end. The 4 conductors are held together in the chuck of a manual drill at the other end with enough leverage to also withstand the torque. The user

simultaneously pulls the conductors through the funnel and twists by turning the drill until the desired length of the conductor is achieved. A similar fixture was printed off for the 3 bundle conductor used in Coil 4.

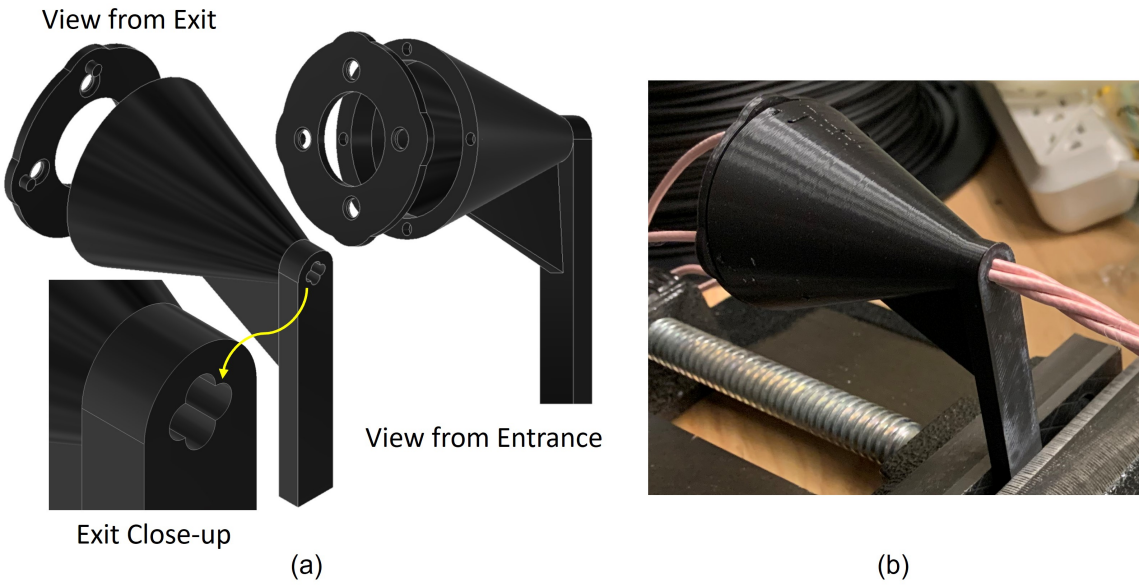

Figure 4-5: 3D printed funnel fixture for constructing pre-formed Litz bundles.

Once the desired length has been achieved, both ends are tied down in a manner that can withstand the significant torque build up. At this point if either end is let go, the entire conductor will unravel. To prevent this from a happening, TG-LH-FBPE-80 flexible potting resin with the properties shown in Fig. 4-6 was coated along the conductor and allowed to dry for several days. This resin has several beneficial properties. Not only is it electrically insulating, but it also has a higher thermal conductivity than air and therefore helps extract heat out from the center of the bundle. The resin also wets the Nomex insulation, decreasing its effective thermal impedance. Finally, the flexibility of the resulting conductors allows them to be wound after drying instead of using a wet winding process.

After the 4 conductors with varying lengths were fabricated, they were wound into respective coils. The two inner resonant coils were wound onto 3D printed spacers clipped to a 10.25" PMMA cylinder. The drive and load coils were similarly wound into spacing clips attached on the outside of a 12" PMMA cylinder. These two cylinders are then inserted into one another to assemble the full transformer as shown in Fig. 4-7.

After construction, the DC resistances of each coil were measured and are tabulated in Table 4.3. Additionally, the self and mutual inductance were measured with a VNA by selectively shorting coils while observing the inductance at the terminals of another coil. The coupling coefficients are then extracted from the inductance matrix according to,

$$K_{ij} = \frac{L_{ij}}{\sqrt{L_i L_j}} \tag{4.10}$$

Properties	Part A Resin	Part B Hardener	Mixed	Unit	Test Method
Thermal Conductivity	-	-	1.1	W/mK	ASTM D5470
Chemical type	Epoxy	Amine	-	-	-
Colour	Black liquid	Clear, yellowish liquid	-	-	Visual
Mix ratio, by weight	2.0	1.0	-	-	-
Viscosity, CAP2000+ viscometer, 25° C	22,200	140	3,200	cP	ASTM D1084
Hardness, cured 25° C for 7 days	-	-	65	Shore A	ASTM D2240
Water boil, weight gain, 24 hour	-	-	1.0	%	-
Ionic content, Cl	-	-	>500	ppm	-
Ionic content, K	-	-	N.D.	-	-
Ionic content, Na	-	-	N.D.	-	-
Electrical resistivity	-	-	10^{16}	ohm/cm	-
Filler type	Metal oxide	-	-	-	-
Maximum Operating Temperature	-	-	200	° C	-
Glass Transition Temperature (T_g)	-	-	24	° C	-
CTE1 (Coefficient of Thermal Expansion before (T_g))	-	-	40	ppm/K	-
CTE2 (Coefficient of Thermal Expansion after (T_g))	-	-	181	ppm/K	-
Shelf life, 25° C	12	12	-	Month	-
Pot life, 25° C	-	-	6	Hour	-

Recommended Cure

Alternative Cure	Temp. (°C)	Cure Time
A	25	24 hours
B	50	4 hours

TG-LH-FBPE-80

Figure 4-6: TG-LH-FBPE-80 flexible potting resin properties

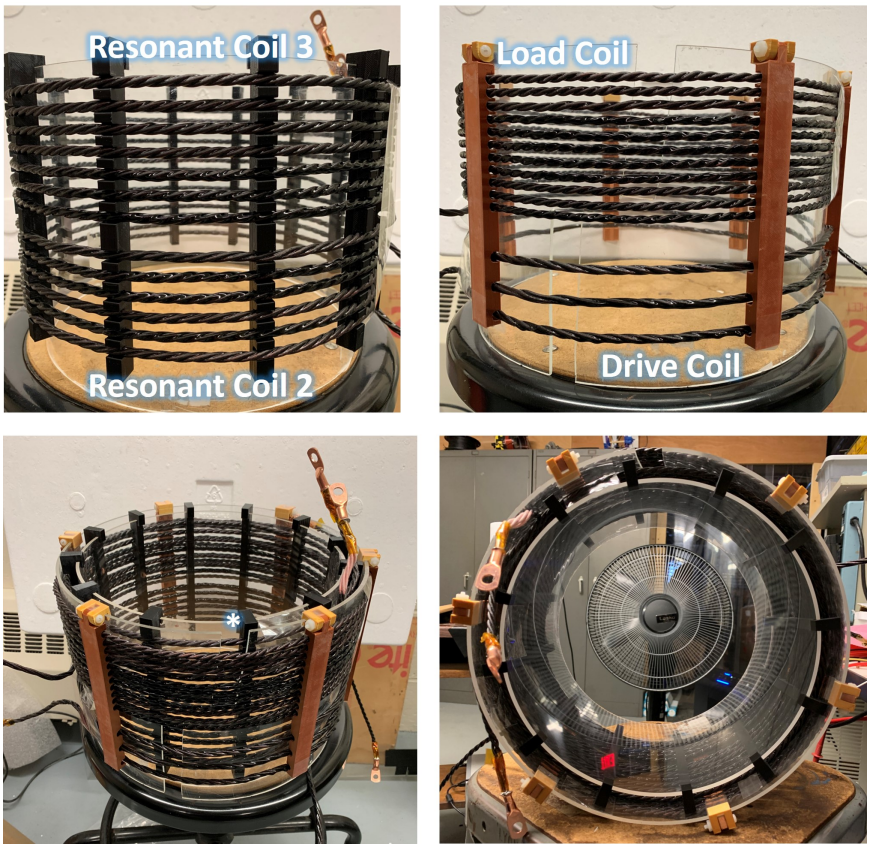

Figure 4-7: Inner and outer cylinder sub-assemblies and the fully constructed ultra-high efficiency 40 kW transformer.

with the results tabulated in Table 4.4 next to the theoretical design values.

Table 4.3: DC Resistance of Each Coil in the Ultra-high Efficiency Transformer

Coil	DC Resistance
Drive (1)	7.08 mΩ
1st Resonant (2)	13.03 mΩ
2nd Resonant (3)	15.06 mΩ
Load (4)	35.09 mΩ

Table 4.4: Theoretical and Measured Coupling Coefficients of the Ultra-high Efficiency Transformer

Coupling Coefficient	Theoretical Value	Measured Value
K_{12}	0.75517	0.75143
K_{13}	0.34403	0.36219
K_{14}	0.38312	0.36093
K_{23}	0.37373	0.36785
K_{24}	0.39879	0.35502
K_{34}	0.80342	0.81751

4.5 Performance Comparisons

It becomes difficult, at efficiencies as great as 98%, to measure the power loss in the resonant transformer accurately. This is in part due to the dependence of the coil currents on the inter-coil coupling, high frequency operation, and low magnitude loss as a fraction of the total through power. Many electrical measurement tools such as differential voltage probes and current probes have higher percentage error with increasing frequency. Fiber optic differential probes perform better at high frequencies but tolerances are still not tight enough to measure losses with the 0.1% fidelity really needed to demonstrate performance improvements between the solid conductor transformer and the ultra-high efficiency version.

4.5.1 Thermal Measurement Techniques

Thermal measurements are a form of loss signal amplification as the only source of temperatures above ambient is heat flux from conduction loss. While the most accurate method of measuring temperatures is through temperature sensors, whether they be thermistors or thermocouples, for purposes of our measurements a thermal camera, which captures IR signals emanating from a heat source, provides the best insight into the temperature of the system as a whole and is the most flexible in that regard. Their are also benefits in terms of electrical isolation that become important during full transformer operation.

The FLIR A700 was used to produce all thermal imaging in this study. The measurement setup shown in Fig. 4-8 was constructed to capture the temperature

transients of the two resonant coils of the ultra-high efficiency transformer carrying a large DC current. This type of test is used for calibration of the coils' thermal capacitance to back out loss from the initial temperature transients due to the coils carrying any arbitrary periodic current waveform, as will be discussed later in this section.

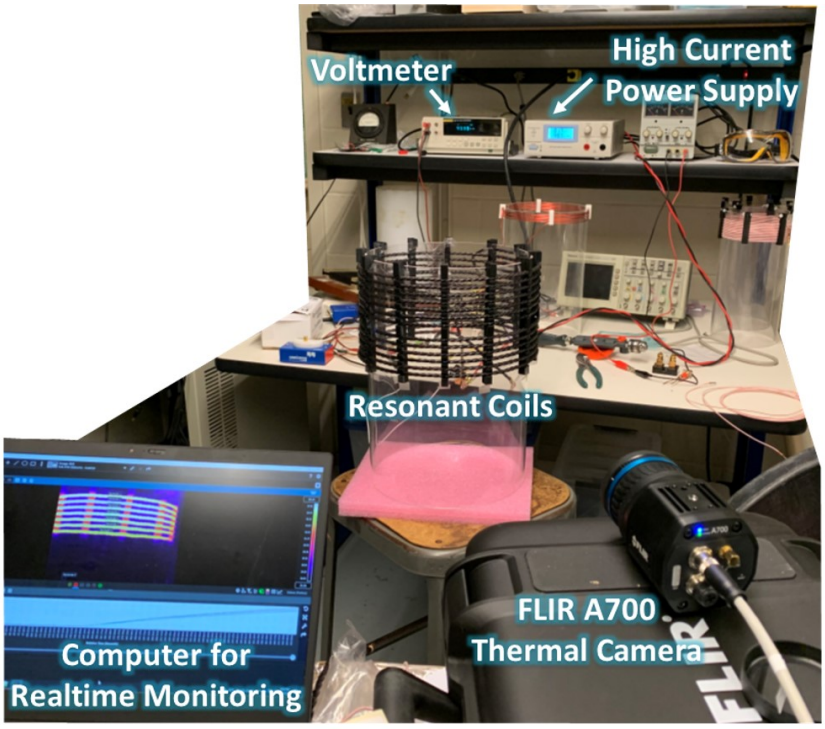

Figure 4-8: Experimental setup for the thermal measurements of an ultra-high efficiency resonant coil carrying a large DC current.

Fig. 4-9 shows a thermal image of the two resonant coils at near steady-state temperature when running 50 A DC through the coils in series. A Circuit Specialist 15 V, 60 A switch-mode DC power supply was used to drive the current and a Fluke meter measured the voltage across a 1 mΩ $\pm$0.1% resistor placed in series with the coils using the Kelvin measurement technique for accurate current sensing.

Fig. 4-10 shows the temperature profiles from ambient and rate of temperature change for each turn in the second resonant coil (Coil 3). The temperature was averaged over a small area within the visible turn to reduce the impact of local IR sensor noise and the ambient temperature was recorded and subtracted from the turn measurements to nullify global noise such as mid-run re-calibrations that the camera periodically performs.

Steady-state temperatures are a good way to qualitatively compare losses between different excitations of the same coil in a relatively constant ambient environment, however to back out loss quantitatively, the thermal impedance from the coil to ambient must be known. This is simple in theory if one assumes a lumped element equivalent thermal circuit, but in practice real considerations such as buoyant natural

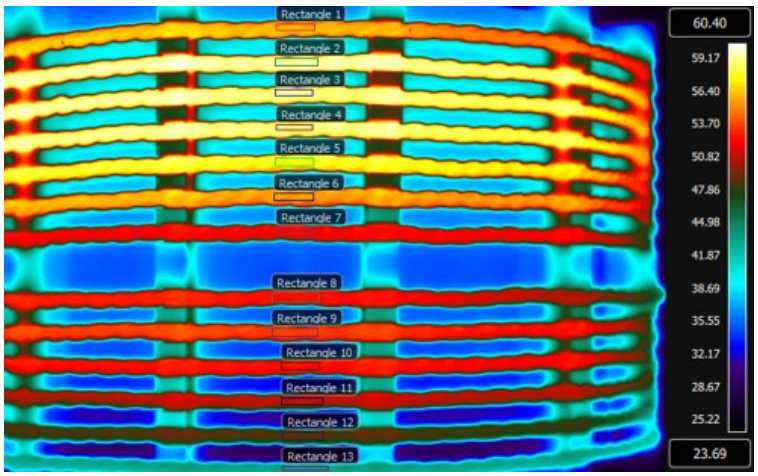

Figure 4-9: Thermal capture of the two resonant coils of the ultra-high efficiency transformer when carrying 50 A DC in series.

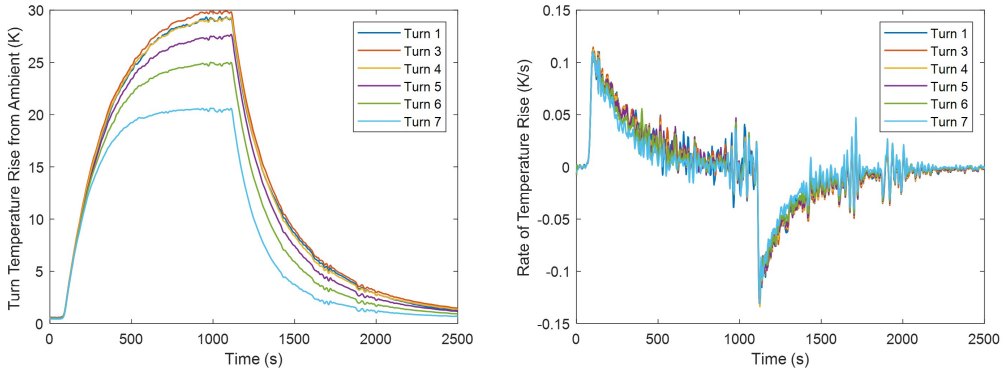

Figure 4-10: On a turn-by-turn basis for the second resonant coil carrying 50 A DC (left) the temperature vs. time curve and (right) the rate of temperature change vs. time curve

convection, heat rise, fluctuating ambients, and turn-to-turn heating make this a non-trivial approach. Instead the initial transient can be used to compute loss with the simple relationship,

$$P_{loss} = C_{heat}\frac{dT}{dt} \tag{4.11}$$

The working assumption here is that because the coils are initially at ambient, there is no heat leakage through the theoretical shunt thermal impedance to ambient because of zero temperature differential. Therefore, all of the power loss in the coil during the first few moments goes into charging the coil's thermal capacitance, C_{heat}, which is a physical property calculated from the materials specific heat, c, and the mass of the material, m,

$$C_{heat} = cm \tag{4.12}$$

This behaviour can be seen in Fig. 4-10 as while the general temperature curve for each coil follows a path similar to a parallel RC circuit (with different resistances to ambient) driven by a current source, the initial rate of change of the temperature for each turn is the same.

This method has been used to measure losses in magnetic cores as high frequency [71] and can be performed on a turn-by-turn basis or on the transformer as a whole. The difficulty in this measurement technique comes from amplified noise due to time differentiation of the temperature signal. To mitigate this, a Savitzky-Golay filter [72] is applied to the temperature data. The filter generates a polynomial fit between adjacent points and effectively smooths the temperature signal without distorting trends, making it more tenable for differentiation. Still, the power loss is discontinuous in the transition from non-excited to excited and smoothing will inevitably distort the initial slope. For this reason, it's important to run several calibration tests and get a nominal value for C_{heat} through averaging. Varying DC currents were injected into Coil 3 and the rate of change of temperature change was measured and is shown in Fig. 4-11. The excitation and outcome for each calibration run are provided in Table 4.5.

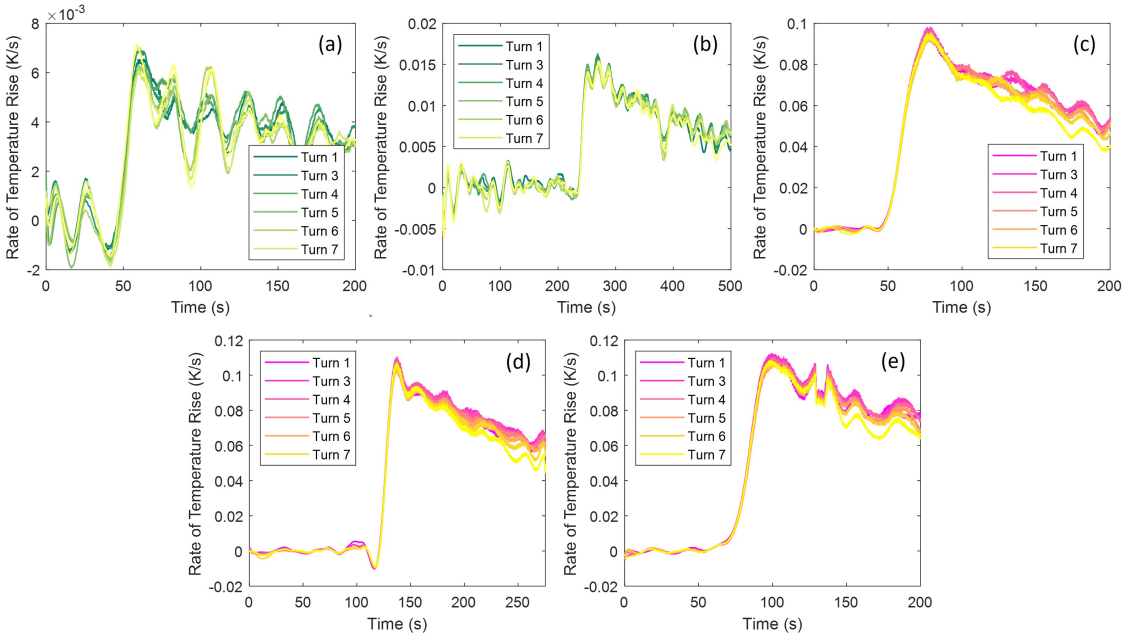

Figure 4-11: Rate of change of temperatures for each turn in Coil 3 with corresponding excitation conditions provided in Table 4.5.

Note: Artifacts of the Savitzky-Golay filter are present in the waveforms of Fig. 4-11 and may impact the thermal capacitance measurements. This can be corrected in the future by correlating percentage overshoot of the filter applied to an ideal RC waveform to the measured waveform, using the same window size.

The data in Table 4.5 demonstrates the importance of high power loss to get clean temperature data. For this reason, the thermal capacitance calculated from the largest current excitation is taken as the final measured value. Additionally, the 50

Table 4.5: Test Conditions of the Calibration Runs for Thermal Capacitance in the Second Resonant Coil ($R_{DC,\,tot} = 15.06$ mΩ)

Label	DC Current (A)	$\langle \frac{dT}{dt}_{peak} \rangle$ (K/s)	P_{loss}/turn (W/turn)	C_{heat}/turn (J/K-turn)
(a)	11	0.0065	0.260	40
(b)	18	0.0154	0.697	45.26
(c)	45	0.0957	4.357	45.53
(d)	47.5	0.1061	4.854	45.75
(e)	50	0.1092	5.379	49.26

A waveform had the least amount of artifacts from the smoothing filter. However, calibrations may also be run at similar power levels to those expected during full operation. This experimental process was repeated to measure the thermal capacitance per turn in each coil of the ultra-high efficiency transformer and the data is given in Table 4.6.

Table 4.6: Experimentally measured thermal capacitances per turn in each coil of the ultra-high efficiency transformer

Coil	C_{heat}/turn (J/K-turn)
Drive (1)	52.29
1st Resonant (2)	47.90
2nd Resonant (3)	50.46
Load (4)	38.77

The measured thermal capacitances make intuitive sense in relation to one another as the the drive coil, with 4 Litz sub-bundles and the largest turn diameter, should have the largest thermal mass and therefore thermal capacitance. Likewise, the two inner resonant coils have 4 Litz sub-bundles, but a smaller turn diameter than the Drive coil. Therefore, their thermal capacitances should be slightly smaller than that of the drive coil. Finally, the load coil has 3 Litz sub-bundles and roughly the same diameter as the drive coil. Its thermal capacitance should be approximately 75% that of the drive coil, which is evident.

4.5.2 Full Operation Thermal Comparisons

Due to the nested structure of the transformer, the thermal camera is unable to view the inner resonant coils and therefore only a qualitative comparison can be made between the solid conductor transformer and the ultra-high efficiency transformer. To control the environment and ensure, as best as possible, no temperature fluctuations due to moving air in the lab, the transformers were placed in an insulating styrofoam box shown in Fig. 4-12 with a viewing window cut out. This results in a reheating effect, but serves the purpose of comparing between the two transformers.

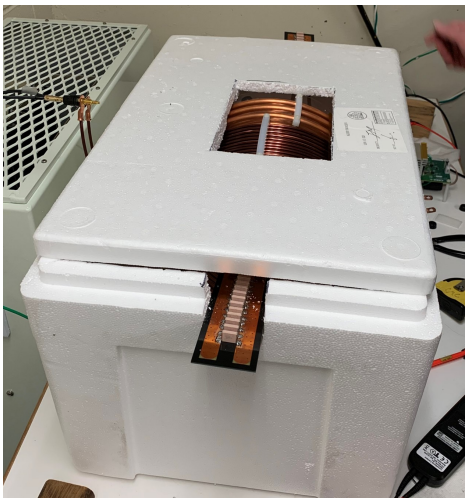

Figure 4-12: Insulating styrofoam chamber with a viewing window cut out to minimize the impact of flowing air in the environment on temperature measurements.

With the chamber setup, each transformer was operated to the maximum capabilities of the lab. Both transformers were run at 1.5 kW for full power and 750 W for half power. Fig. 4-13 shows the thermal profile of the solid conductor transformer at 1.5 kW for an extended duration. The power was turned off at 140 minutes to observe cool down.

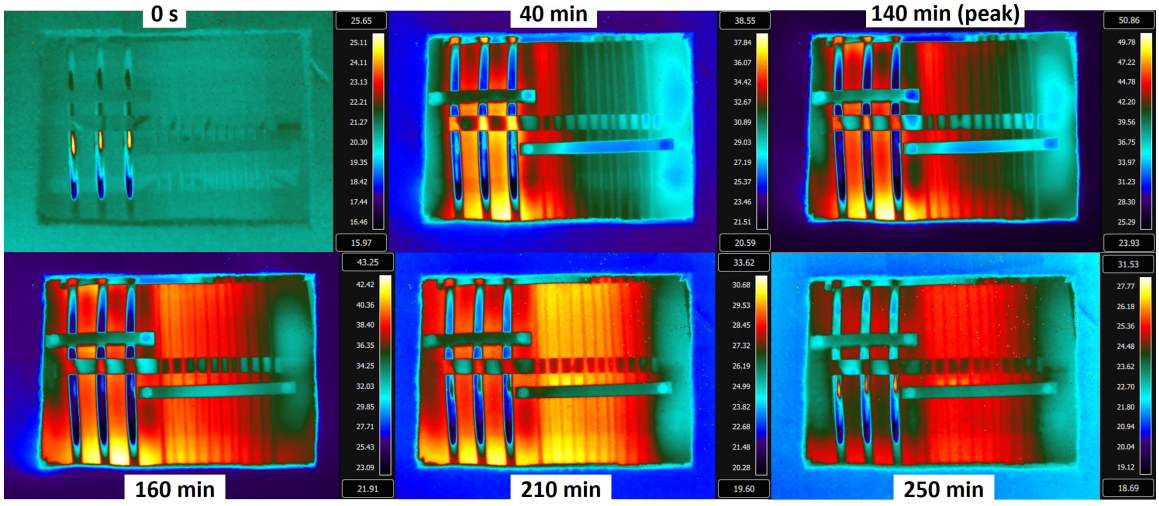

Figure 4-13: Periodic thermal images of the solid conductor transformer operated at 1.5 kW in the thermal isolation chamber for >2 hours.

For the solid conductor transformer measurements, a layer of thin Kapton tape was placed along all of the visible turns in order negate the high emissivity of the shiny copper turns and its distortion of the temperature signals. The tape is both electrically and thermally insulating such that it does not allow heat transfer between turns. It is, however, in close thermal contact with each turn and heats up locally

according to the temperature at the contact surface. This tape was not necessary for the ultra-high efficiency transformer measurements due to the black resin having low emissivity.

A comparison of the absolute temperatures of the 14 observable turns in each transformer at full (1.5 kW) and half (750 W) power is provided in Fig. 4-14 for the same operating time window. From these results, it is observed that the ultra-high efficiency transformer has less than half the loss of the solid conductor transformer. In fact the low loss (LL) transformer has lower temperatures operating at full power than the solid conductor transformer has operating at half power. While the exact efficiency of either transformer is not known exactly, the solid conductor transformer is much easier to model and compute losses through a full FEA simulation. Therefore there is high confidence in the designed efficiency (98.6%) of the solid conductor transformer. This results in an efficiency of >99.3% in the ultra-high efficiency design.

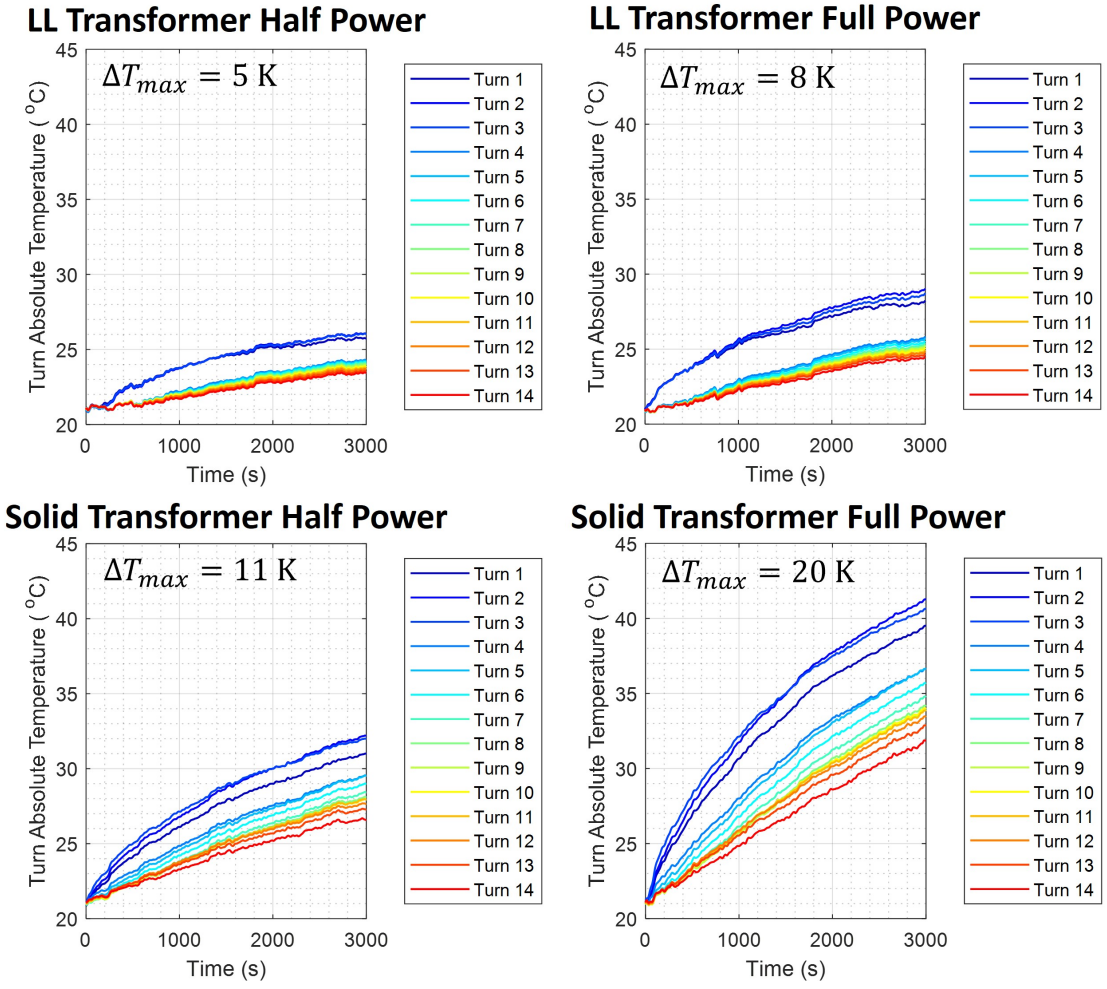

Figure 4-14: Temperature vs. time profile for the two transformers (Low Loss = LL) operated at full (1.5 kW) and half (750 W) power for 50 minutes. The maximum temperature rise, amongst all observable turns, from the start to end of the 50 minute window is shown.

4.6 Conclusions and Future Work

In conclusion, this thesis covered the design methodology of an ultra-high efficiency coreless resonant transformer and focused on the minimization of AC conduction losses. Considerations unique to large-scale industrial applications guided the studies towards simultaneous complexity minimization to address the economics of the transformer. For this reason, a methodical approach was taken to exhaustively study all options of conductor geometries and to provide insight into the trade-offs of complexity and performance. Increasingly complex conductor designs, starting with the simplest geometry of solid conductor coils and ending with multi-level Litz structures, were studied to determine the performance extent of each variation. A diverse set of numerical, analytical, and experimental tools were utilized throughout this work. Along the way, where a void in analysis existed, contributions were made to the literature regarding modeling techniques such as addressing non-ideal Litz conductor construction [73] and multi-phase Litz wire loss implications [74].

After converging on a design for a 40 kW transformer that maximized efficiency and minimized conductor complexity, the ultra-high efficiency design, with a theoretical efficiency of 99.5% at full load and 300 kHz operating frequency, was constructed and compared to a magnetically equivalent design consisting of solid conductor coils. The comparison was done using thermal measurement techniques to amplify the loss signal, and a makeshift thermal isolation chamber was used to minimize the impact of moving air on the coil temperatures. Experimental results suggest that the ultra-high efficiency transformer has less than half the losses of the solid conductor coil, which has a designed efficiency of 98.6%. This leads to the conclusion that the ultra-high efficiency transformer is >99.3% efficient and can therefore carry twice the power of the solid conductor transformer (40 kW $\rightarrow$ 80 kW) under the same temperature constraints.

Experimental results show good alignment with the modeling techniques developed in this work, however, future work should focus on further validating the multi-phase Litz loss phenomenon with experiments and applying a similar analysis technique to circular cross-section solid conductor coils to determine the applicability to the simplest of conductor geometries.

Appendix A

Mathematical Definitions

Definitions for the Kelvin functions used in (3.14) and (3.16) are written below, where $\mathcal{J}_\nu(\theta)$ is the ν^{th} order Bessel function of the first kind [75],

$$ber(x) = ber_0(x) \tag{A.1}$$

$$bei(x) = bei_0(x) \tag{A.2}$$

$$ber_\nu(x) = \Re\mathrm{e}\Big\{\mathcal{J}_\nu\big(xe^{\frac{j3\pi}{4}}\big)\Big\} \tag{A.3}$$

$$bei_\nu(x) = \Im\mathrm{m}\Big\{\mathcal{J}_\nu\big(xe^{\frac{j3\pi}{4}}\big)\Big\} \tag{A.4}$$

$$ber'(x) = \frac{ber_1(x) + bei_1(x)}{\sqrt{2}} \tag{A.5}$$

$$bei'(x) = \frac{bei_1(x) - ber_1(x)}{\sqrt{2}} \tag{A.6}$$

Appendix B

Coil Measurement Calibration Gauge

Taking low resistance measurements at high frequencies is challenging for any impedance analyzer or vector network analyzer (VNA), especially for coils with significant inductance. The reactance of a coil at high frequencies can be several orders of magnitude higher than the resistance component. This means the measurement equipment must be sensitive enough to detect very small phase differences.

The Omicron Bode 100 VNA was used for all of the measurements taken in this paper. Several measurement methods are possible with a VNA and Omicron's manual provides the suggested method range depending upon the frequency sweep of measurement and impedance magnitude of the device under test (DUT). Fig. B-1 shows a region plot provided in the Omicron Bode 100 documentation with their suggested measurement technique according to the impedance magnitude of the DUT. Overlaid onto this graph is the estimated impedance magnitude of the 6-turn, 5x5x42/44 AWG Litz conductor coil studied in Section 3.4.

The "one-port" method is recommended for the coils measured in this paper and was shown via a sensitivity study to be the best method. The short calibration was performed with a gold short as the DUT, while a purely resistive tight tolerance 1.1 Ω resistor was used as a DUT for the load calibration. After performing the open calibration, the VNA has all the information it needs to discern the impedance. To verify the calibration quality, several coil configurations using 14 AWG solid magnet wire were then measured. These solid conductor coils had similar nominal impedances to the Litz solenoids measured in Section 3.4, and therefore the phase differentiation required by the VNA was also similar. Turn-to-turn spacing was fixed at three different set values using 3D printed coil forming clips. The solid conductor coil geometry is well defined and therefore measurements should match simple 2D axisymmetric FEA simulation results. The VNA calibration was reperformed until the solid conductor coil measurements were found to closely follow FEA after linearly scaling to match DC resistances. This is necessary because of poor performance of the "one-port" measurement method at low-frequencies. As shown in Fig. B-2, the coil measurements do in fact closely follow FEA after linearly scaling to match DC resistances. The authors suggest gauging calibration quality with a fixed coil of known frequency dependent resistance prior to the measurement of the more complex Litz wire coils.

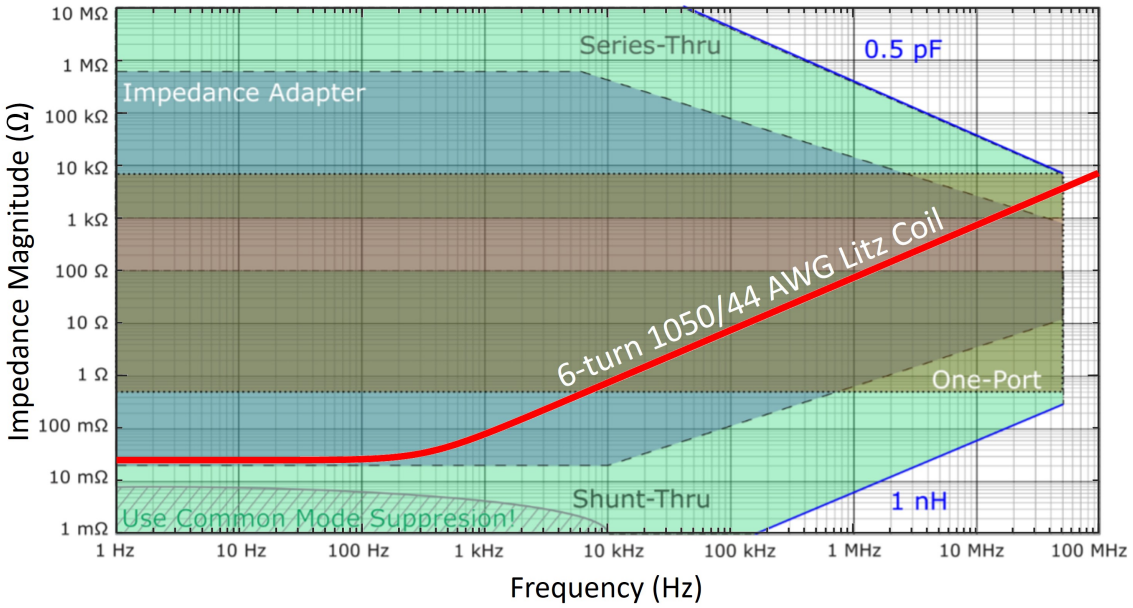

Figure B-1: Region plot provided in Omicron's documentation recommending measurement techniques according to impedance magnitude of the DUT. Estimated impedance magnitude of the 6-turn, 5x5x42/44 AWG Litz conductor coil studied in Section 3.4 is overlaid.

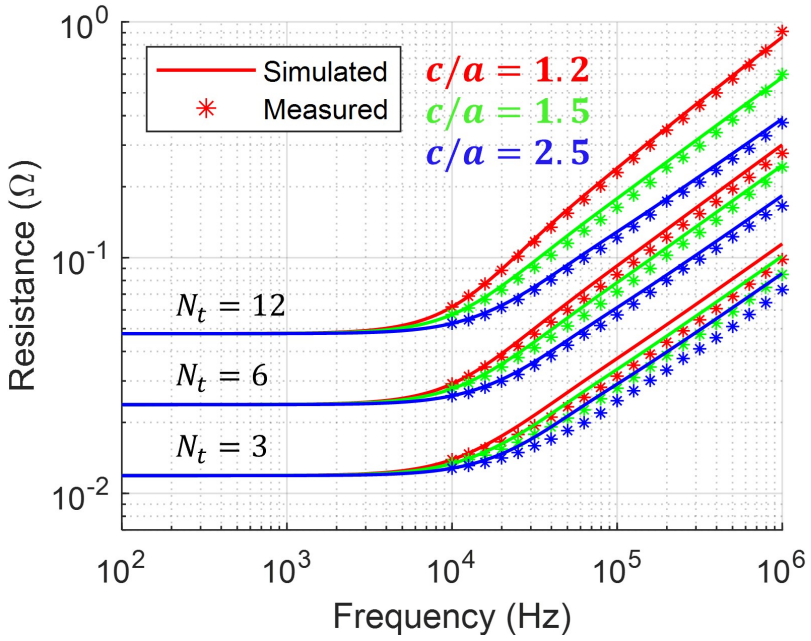

Figure B-2: Measurement and FEA simulation results for several coil constructions using a solid 14 AWG magnet wire.

Appendix C

Code

C.1 Layered Mesh Analysis for 5x5x42/44 AWG Litz Solenoid

The code used to perform Layered Mesh analysis on a solenoid composed of 5x5x42/44 AWG Litz wire, as described in Section 3.4, can be found on MATLAB's Central File Exchange [76]. It requires COMSOL's AC/DC module with LiveLink for MATLAB scripting. The inputs and outputs to the code are described in Fig. C-1.

Inputs:
- *dbos* - the diameter of the bundle's outer surface [m]
- *gauge* - strand gauge used in the conductor [AWG]
- *N1* - number of bundles in the first level
- *freqs* - vector containing the frequencies to perform analysis at [Hz]
- *Ns* - total number of strands in the conductor
- *Nt* - number of turns in the solenoid
- *ca* - vector containing the c/a spacing factor of each coil, defined as *c/a - coil pitch / dbos*
- *Dc* - coil diameter taken from the center of the conductors [m]
- *BF* - bundle factor (referred to as fabrication factor in [1])

Outputs:
- *Rac* - vector containing the AC resistance of the coil at each frequency specified [Ohms]

Figure C-1: Description of inputs and outputs to the Layered Mesh analysis code for a solenoid composed of 5x5x42/44 AWG Litz wire.

C.2 Layered Mesh Analysis for 5x40/36 AWG Litz Solenoid

The code used to perform Layered Mesh analysis on a solenoid composed of 5x40/36 AWG Litz wire, as described in Section 3.4, can be found on MATLAB's Central File Exchange [77]. It requires COMSOL's AC/DC module with LiveLink for MATLAB scripting. The inputs and outputs to the code are described in Fig. C-2.

Inputs:
- *dbos* - the diameter of the bundle's outer surface [m]
- *gauge* - strand gauge used in the conductor [AWG]
- *N1* - number of bundles in the first level
- *freqs* - vector containing the frequencies to perform analysis at [Hz]
- *Ns* - total number of strands in the conductor
- *Nt* - number of turns in the solenoid
- *ca* - vector containing the c/a spacing factor of each coil, defined as *c/a - coil pitch / dbos*
- *Dc* - coil diameter taken from the center of the conductors [m]
- *BF* - bundle factor (referred to as fabrication factor in [1])

Outputs:
- *Rac* - vector containing the AC resistance of the coil at each frequency specified [Ohms]

Figure C-2: Description of inputs and outputs to the Layered Mesh analysis code for a solenoid composed of 5x40/36 AWG Litz wire.

C.3 Multi-phase Litz Semi-analytical AC Loss Calculation

The semi-analytical code used to perform AC loss analysis on cylindrical Litz coils composed of ideal Litz wire, as described in Section 3.5, can be found on MATLAB's Central File Exchange [78]. The inputs and outputs to the code are described in Fig. C-3.

Inputs:
- *dbos_c* - vector containing the diameter of the bundle's outer surface for each coil [m]
- *Dc_c* - vector containing each coil's diameter, defined from the center of the bundle [m]
- *Nt* - vector containing the number of turns in each coil
- *ca* - vector containing the c/a spacing factor of each coil, defined as: *c/a = coil pitch / dbos*
- *z_c* - vector containing the axial position of the top turn for each coil [m]
- *ds_c* - vector containing the strand diameter used in the Litz bundle for each coil [m]
- *Ns_c* - vector containting the number of strands in the Litz bundle for each coil
- *Ipeak_c* - vector containing the peak sinusoidal AC current magnitude in each coil [A]
- *phi_c* - vector containing the relative phase of the current in each coil [rad]
- *f* - vector of frequencies to analyze the system at

Outputs:
- *Ploss* - vector containing the total power loss for each input frequency [W]
- *Ps* - vector containing the power loss due to skin-effect for each input frequency [W]
- *Pp* - vector containing the power loss due to proximity-effect for each input frequency [W]

Figure C-3: Description of inputs and outputs to the multi-phase Litz analytical AC loss calculation code.

Bibliography

[1] A. J. Carvajal, "First principles design of coreless power transformers," Master's thesis, Cambridge, MA, 2016.

[2] D. E. Schemmel, *Design of High-Power High-Frequency Coreless Transformer Systems*. PhD thesis, Cambridge, MA, 2022.

[3] P. Dowell, "Effects of eddy currents in transformer windings," *Proceedings of the Institution of Electrical Engineers*, vol. 113, no. 8, p. 1387, 1966.

[4] J. Ferreira and J. D. Van Wyk, "A new method for the more accurate determination of conductor losses in power electronic converter magnetic components," in *Third International Conference on Power Electronics and Variable-Speed Drives*, pp. 184–187, 1988.

[5] J. Ferreira, "Improved analytical modeling of conductive losses in magnetic components," *IEEE Transactions on Power Electronics*, vol. 9, no. 1, p. 127–131, 1994.

[6] M. Bartoli, N. Noferi, A. Reatti, and M. Kazimierczuk, "Modeling litz-wire winding losses in high-frequency power inductors," *PESC Record. 27th Annual IEEE Power Electronics Specialists Conference.*

[7] M. Bartoli, A. Reatti, and M. Kazimierczuk, "Minimum copper and core losses power inductor design," in *IAS '96. Conference Record of the 1996 IEEE Industry Applications Conference Thirty-First IAS Annual Meeting*, vol. 3, pp. 1369–1376 vol.3, 1996.

[8] C. Sullivan, "Optimal choice for number of strands in a litz-wire transformer winding," *IEEE Transactions on Power Electronics*, vol. 14, no. 2, pp. 283–291, 1999.

[9] F. Tourkhani and P. Viarouge, "Accurate analytical model of winding losses in round litz wire windings," *IEEE Transactions on Magnetics*, vol. 37, no. 1, p. 538–543, 2001.

[10] J. Acero, P. Hernandez, J. Burdio, R. Alonso, and L. Barragdan, "Simple resistance calculation in litz-wire planar windings for induction cooking appliances," *IEEE Transactions on Magnetics*, vol. 41, no. 4, pp. 1280–1288, 2005.

[11] E. Plumed, J. Acero, I. Lope, and C. Carretero, "3d finite element simulation of litz wires with multilevel bundle structure," in *IECON 2018 - 44th Annual Conference of the IEEE Industrial Electronics Society*, pp. 3479–3484, 2018.

[12] E. Plumed, I. Lope, C. Carretero, and J. Acero, "A recursive methodology for modelling multi-stranded wires with multilevel helix structure," *Applied Mathematical Modelling*, vol. 83, p. 76–89, 2020.

[13] J. Acero, I. Lope, J. M. Burdio, C. Carretero, and R. Alonso, "Loss analysis of multistranded twisted wires by using 3d-fea simulation," *Workshop on Control and Modeling for Power Electronics (COMPEL)*, 2014.

[14] T. Guillod, J. Huber, F. Krismer, and J. W. Kolar, "Litz wire losses: Effects of twisting imperfections," in *2017 IEEE 18th Workshop on Control and Modeling for Power Electronics (COMPEL)*, pp. 1–8, 2017.

[15] R. Y. Zhang, J. K. White, J. G. Kassakian, and C. R. Sullivan, "Realistic litz wire characterization using fast numerical simulations," *2014 IEEE Applied Power Electronics Conference and Exposition - APEC 2014*, 2014.

[16] R. Y. Zhang, J. K. White, and J. G. Kassakian, "Fast simulation of complicated 3-d structures above lossy magnetic media," *IEEE Transactions on Magnetics*, vol. 50, no. 10, 2014.

[17] A. Rokopf, E. Bar, C. Joffe, and C. Bonse, "Calculation of power losses in litz wire systems by coupling fem and peec method," *IEEE Transactions on Power Electronics*, vol. 31, no. 9, 2016.

[18] J. Lyu, H. Chen, Y. Zhang, Y. Du, and Q. S. Cheng, "Fast simulation of litz wire using multilevel peec method," *IEEE Transactions on Power Electronics*, vol. 35, no. 12, p. 12612–12616, 2020.

[19] S. Ehrlich, H. Rossmanith, M. Sauer, C. Joffe, and M. Marz, "Fast numerical power loss calculation for high-frequency litz wires," *IEEE Transactions on Power Electronics*, vol. 36, no. 2, p. 2018–2032, 2021.

[20] C. Sullivan, "Cost-constrained selection of strand diameter and number in a litz-wire transformer winding," in *Conference Record of 1998 IEEE Industry Applications Conference. Thirty-Third IAS Annual Meeting (Cat. No.98CH36242)*, vol. 2, pp. 900–906 vol.2, 1998.

[21] C. Sullivan, J. McCurdy, and R. Jensen, "Analysis of minimum cost in shape-optimized litz-wire inductor windings," in *2001 IEEE 32nd Annual Power Electronics Specialists Conference (IEEE Cat. No.01CH37230)*, vol. 3, pp. 1473–1478 vol. 3, 2001.

[22] O. Lucía, J. M. Burdío, L. A. Barragán, J. Acero, and I. Millán, "Series-resonant multiinverter for multiple induction heaters," *IEEE Transactions on Power Electronics*, vol. 25, no. 11, pp. 2860–2868, 2010.

[23] H. Kurose, D. Miyagi, N. Takahashi, N. Uchida, and K. Kawanaka, "3-d eddy current analysis of induction heating apparatus considering heat emission, heat conduction, and temperature dependence of magnetic characteristics," *IEEE Transactions on Magnetics*, vol. 45, no. 3, pp. 1847–1850, 2009.

[24] A. P. Sample, D. T. Meyer, and J. R. Smith, "Analysis, experimental results, and range adaptation of magnetically coupled resonators for wireless power transfer," *IEEE Transactions on Industrial Electronics*, vol. 58, no. 2, pp. 544–554, 2011.

[25] S. Li and C. C. Mi, "Wireless power transfer for electric vehicle applications," *IEEE Journal of Emerging and Selected Topics in Power Electronics*, vol. 3, no. 1, pp. 4–17, 2015.

[26] S. Y. R. Hui, W. Zhong, and C. K. Lee, "A critical review of recent progress in mid-range wireless power transfer," *IEEE Transactions on Power Electronics*, vol. 29, no. 9, pp. 4500–4511, 2014.

[27] S. Li, W. Li, J. Deng, T. D. Nguyen, and C. C. Mi, "A double-sided lcc compensation network and its tuning method for wireless power transfer," *IEEE Transactions on Vehicular Technology*, vol. 64, no. 6, pp. 2261–2273, 2015.

[28] D. Gerada, A. Mebarki, N. L. Brown, C. Gerada, A. Cavagnino, and A. Boglietti, "High-speed electrical machines: Technologies, trends, and developments," *IEEE Transactions on Industrial Electronics*, vol. 61, no. 6, pp. 2946–2959, 2014.

[29] A. Tenconi, S. Vaschetto, and A. Vigliani, "Electrical machines for high-speed applications: Design considerations and tradeoffs," *IEEE Transactions on Industrial Electronics*, vol. 61, no. 6, pp. 3022–3029, 2014.

[30] A. M. EL-Refaie, J. P. Alexander, S. Galioto, P. B. Reddy, K.-K. Huh, P. de Bock, and X. Shen, "Advanced high-power-density interior permanent magnet motor for traction applications," *IEEE Transactions on Industry Applications*, vol. 50, no. 5, pp. 3235–3248, 2014.

[31] A. Yoon, X. Yi, J. Martin, Y. Chen, and K. Haran, "A high-speed, high-frequency, air-core pm machine for aircraft application," *2016 IEEE Power and Energy Conference at Illinois (PECI)*, 2016.

[32] X. Yi, A. Yoon, and K. S. Haran, "Multi-physics optimization for high-frequency air-core permanent-magnet motor of aircraft application," in *2017 IEEE International Electric Machines and Drives Conference (IEMDC)*, pp. 1–8, 2017.

[33] N. J. Renner, J. D. Lenz, X. Yi, and K. S. Haran, "Development of form-wound air-core armature windings for high-frequency electric machines," in *2017 IEEE International Electric Machines and Drives Conference (IEMDC)*, pp. 1–8, 2017.

[34] A. Ruehli, "Equivalent circuit models for three-dimensional multiconductor systems," *IEEE Transactions on Microwave Theory and Techniques*, vol. 22, no. 3, 1974.

[35] A. E. Ruehli, "Inductance calculations in a complex integrated circuit environment," *IBM Journal of Research and Development*, vol. 16, no. 5, 1972.

[36] D. C. Meeker, "Finite element method magnetics, version 4.2," 2018.

[37] "Product selection guide," *New England Wire Technologies*.

[38] C. R. Sullivan and R. Y. Zhang, "Analytical model for effects of twisting on litz-wire losses," in *2014 IEEE 15th Workshop on Control and Modeling for Power Electronics (COMPEL)*, pp. 1–10, 2014.

[39] COMSOL, "Comsol multiphysics v. 5.6."

[40] COMSOL, "Ac/dc module user's guide, comsol multiphysics v. 5.6."

[41] M. Kamon, M. J. Tsuk, and J. K. White, "Fasthenry: A multipole-accelerated 3-d inductance extraction program," *IEEE Transactions on Microwave Theory and Techniques*.

[42] Y. Hackl, P. Scholz, W. Ackermann, and T. Weiland, "Multifunction approach and specialized numerical integration algorithms for fast inductance evaluations in nonorthogonal peec systems," *IEEE Transactions on Electromagnetic Compatibility*, vol. 57, no. 5, 2015.

[43] H. Chen and Y. Du, "Proximity effect in transient analysis of radio base stations," *International Journal for Numerical Modelling: Advances in EMC Numerical Modelling*, 2018.

[44] A. E. Ruehli, G. Antonini, and L. Jiang, "Skin-effect model for round wires in peec," in *International Symposium on Electromagnetic Compatibility - EMC EUROPE*, pp. 1–6, 2012.

[45] C. A. Hoer and C. H. Love, "Exact inductance equations for rectangular conductors with applications to more complicated geometries," *Journal of Research of the National Bureau of Standards, Section C: Engineering and Instrumentation*, p. 127, 1965.

[46] T. Ibuchi and T. Funaki, "Validation of the air-core inductor copper loss model for high-frequency power conversion applications," in *2013 International Symposium on Electromagnetic Compatibility*, pp. 561–566, 2013.

[47] M. Perry and T. Jones, "Eddy current induction in a solid conducting cylinder with a transverse magnetic field," *IEEE Transactions on Magnetics*, vol. 14, no. 4, p. 227–232, 1978.

[48] X. Nan and C. Sullivan, "An improved calculation of proximity-effect loss in high-frequency windings of round conductors," *IEEE 34th Annual Conference on Power Electronics Specialist, 2003. PESC 03.*

[49] G. S. Smith, "A simple derivation for the skin effect in a round wire," *European Journal of Physics*, vol. 35, no. 2, p. 025002, 2014.

[50] J. R. Riba, "Analysis of formulas to calculate the ac resistance of different conductors' configurations," *Electric Power Systems Research*, vol. 127, pp. 93–100, 2015.

[51] M. Abramowitz and I. A. Stegun, *Handbook of Mathematical Functions with Formulas, Graphs, and Mathematical Tables*. New York: Dover, ninth dover printing, tenth gpo printing ed., 1964.

[52] C. W. Clenshaw, "Chebyshev series for mathematical functions," *National Physical Laboratory Mathematical Tables*, vol. 5, 1962.

[53] "Bessel function of first kind - matlab," 2022.

[54] J. R. Nagel, "Induced eddy currents in simple conductive geometries due to a time-varying magnetic field," *IEEE Antennas & Propagation Magazine*, 2017.

[55] Q. Meng and J. Biela, "Survey and comparison of 1d/2d analytical models of hf losses in litz wire," in *2020 22nd European Conference on Power Electronics and Applications (EPE'20 ECCE Europe)*, pp. P.1–P.11, 2020.

[56] S. Butterworth, "Effective resistance of inductance coils at radio frequency," *Wireless and Wireless Eng.*, vol. 3, p. 483, 1926.

[57] A. Kurs, A. Karalis, R. Moffatt, J. D. Joannopoulos, P. Fisher, and M. Soljacic, "Wireless power transfer via strongly coupled magnetic resonances," *Science*, vol. 317, no. 5834, p. 83–86, 2007.

[58] F. E. Terman, "Radio engineering handbook," *Journal of the British Institution of Radio Engineers*, vol. 11, no. 1, p. 35–35, 1951.

[59] R. Benato and S. D. Sessa, "A new multiconductor cell three-dimension matrix-based analysis applied to a three-core armoured cable," *IEEE Transactions on Power Delivery*, vol. 33, no. 4, pp. 1636–1646, 2018.

[60] H. Nagaoka, "The inductance coefficients of solenoids," *Journal of the College of Science, Imperial University, Tokyo*, vol. 27, no. 6, p. 33, 1909.

[61] P. Czyz and et al., "Design and experimental analysis of 166 kw medium-voltage medium-frequency air-core transformer for 1:1-dcx applications," *IEEE Journal of Emerging and Selected Topics in Power Electronics*, 2021.

[62] J. Peatross and M. Ware, "Physics of light and optics," *Brigham Young University*, 2021.

[63] J. Griffith and G. W. Pan, "Time harmonic fields produced by circular current loops," *IEEE Transactions on Magnetics*, vol. 47, no. 8, 2011.

[64] R. F. Harrington, "Cylindrical wave functions," *Time-Harmonic Electromagnetic Fields, IEEE*, pp. 198–263, 2001.

[65] E. B. Rosa and F. Grover, *Formulas and Tables for the Calculation of Mutual and Self-Inductance.*

[66] E. B. Rosa and F. Grover, *Formulas and Tables for the Calculation of Mutual and Self-Inductance.*

[67] E. B. Rosa and F. Grover, *Formulas and Tables for the Calculation of Mutual and Self-Inductance.*

[68] S. Sudhoff, "Genetic optimization system engineering tool (goset) v. 2.3."

[69] M. R. Hestenes, "Multiplier and gradient methods," *Journal of Optimization Theory and Applications*, vol. 4, pp. 303–320, 1969.

[70] "Litz wire for high efficiency," *ELEKTRISOLA.*

[71] P. Papamanolis, T. Guillod, F. Krismer, and J. W. Kolar, "Transient calorimetric measurement of ferrite core losses up to 50 mhz," *IEEE Transactions on Power Electronics*, vol. 36, no. 3, pp. 2548–2563, 2021.

[72] A. Savitzky and M. J. E. Golay, "Smoothing and differentiation of data by simplified least squares procedures.," *Analytical Chemistry*, vol. 36, no. 8, pp. 1627–1639, 1964.

[73] N. J. Salk and C. M. Cooke, "A versatile simulation-assisted layered mesh analysis for generalized litz wire performance," *IEEE Transactions on Magnetics*, pp. 1–1, 2022.

[74] N. J. Salk and C. M. Cooke, "Calculation of ac losses in multi-phase litz coil systems," *2022 IEEE/AIAA Transportation Electrification Conference and Electric Aircraft Technologies Symposium (ITEC+EATS)*, 2022.

[75] J. W. W., A. Young, and A. Kirk, "Bessel functions. part iv, kelvin functions," *Mathematics of Computation*, vol. 19, no. 90, p. 344, 1965.

[76] N. Salk, "Layered mesh ac loss analysis: 5x5x42/44 awg litz wire," *MATLAB Central File Exchange.*

[77] N. Salk, "Layered mesh ac loss analysis: 5x40/36 awg litz wire," *MATLAB Central File Exchange.*

[78] N. Salk, "Multi-phase ac loss calculation for air-core litz coils," *MATLAB Central File Exchange.*